

TOP-DOWN FABRICATION OF INDIUM ARSENIDE ANTIMONIDE PILLARS
FOR INFRARED DETECTION

TOP-DOWN FABRICATION OF INDIUM ARSENIDE ANTIMONIDE PILLARS
FOR INFRARED DETECTION

By CURTIS GOOSNEY, H.B.Sc.

A Thesis Submitted to the School of Graduate Studies in Partial Fulfillment of the
Requirements for the Degree Master of Applied Science

McMaster University © Copyright by Curtis Goosney, December 2022

McMaster University – Hamilton, Ontario, Canada

Master of Applied Science (2022) – Engineering Physics

TITLE: Top-down fabrication of indium arsenide antimonide pillars for infrared detection

AUTHOR: Curtis Goosney, H.B.Sc. (University of Toronto)

SUPERVISOR: Dr. Ray R. LaPierre

NUMBER OF PAGES: 120

Lay Abstract

Infrared light (IR) falls in the wavelength range of 0.75 μm to 1000 μm , with IR based technology having numerous applications in society. With uses in the sciences, research, medicine, and general everyday technology, common IR ranges for material analysis range from 1.4 to 3 μm in the short-wavelength IR (SWIR), 3-5 μm in the mid-wavelength IR (MWIR), and 8-15 μm in the long-wavelength IR (LWIR). These ranges include IR absorption due to molecular vibrations, and includes wavelengths corresponding to the bandgaps of relevant semiconductor materials for IR detectors. To aid in light absorption in semiconductor materials, nanometer scale cylindrical structures called nanowires or pillars can be used on the detector surface, enhancing light absorption, and allowing for absorption wavelength manipulation by adjusting nanowire diameter. This work focuses on developing IR detectors with wavelength absorption in the 1-16 μm range, dependent on nanowire geometry.

Abstract

InSb and InAsSb pillars, which are large diameter nanowires (NWs), were investigated as an alternative infrared (IR) detector technology to HgCdTe (MCT) for tunable multispectral IR detection with optical properties manipulated by pillar diameter and pitch. Undoped InSb and InAsSb thin films were grown on undoped Si (100) substrates by molecular beam epitaxy (MBE) with a thin AlSb buffer layer. A top-down etching method was used to fabricate pillars of diameters ranging from 300 nm to 1500 nm for InSb, and 1700 nm to 4000 nm for InAsSb. Pillar arrays were analyzed optically by Fourier transform IR spectroscopy (FTIR). The InSb and InAsSb pillars produced narrow absorption peaks with wavelength ranging from 1.61 μm to 6.86 μm for InSb and 8.1 μm to 16.2 μm for InAsSb. A 100 nm increase in pillar diameter corresponded to a 0.495 μm increase in peak absorption wavelength.

InSb thin films were also grown on n-type (As doped, $\leq 0.005 \Omega \text{ cm}$) Si (100) substrates to create a p-i-n junction, with an initial 2 μm thick undoped InSb region grown directly on the substrate, and a 0.5 μm thick p-type (Be doped, $2 \times 10^{19} \text{ cm}^{-3}$) InSb top layer. These films were used to create two devices; an interdigitated contact photoconductor with varying finger geometry, and a photovoltaic device with square top contacts of varying area. I-V characterization demonstrated trends in current with varying finger geometry. Photocurrent measurements were obtained for both the photoconductor and photovoltaic devices under IR and solar illumination. The photocurrent values were orders of magnitude higher for the photoconductive device compared to the photovoltaic device, indicative of

potential photoconductive gain. Photocurrent generation in the InSb p-i-n structure introduces the possibility of diameter-dependent photocurrent generation in etched pillar devices.

Acknowledgements

I will begin by thanking my supervisor, Ray LaPierre, for giving me the opportunity to conduct this research in his lab group. My gratitude for his guidance, support, patience, and knowledge shared with me during our talks is immeasurable, and the skills I have developed as a researcher and experimentalist while under his guidance will accompany me through all my future endeavors. In working under Ray's supervision, I was given the opportunity to meet and work with other skilled researchers. To start, although Mitch Robson was finishing his work as I was starting, he aided me with my transition from undergraduate to graduate studies, and helped me understand device processing skills early on. Simon McNamee, Nebile Isik Goktas, Devan Wagner, and Paige Wilson provided me with a wealth of early and continued practical knowledge. Later, graduate students Amanda Thomas and Ara Ghukasyan provided insightful discussion and assistance, as well as opening an avenue for minor collaboration efforts.

I would like to express my thanks to key researchers and facilities within and beyond McMaster. Starting within McMaster, my thanks is directed towards Doris Stevanovic and Shahram Tavakoli of the Center for Emerging Device Technologies (CEDT) for their patience in assisting me with device processing in McMaster's cleanroom facility, as well as Shahram's extensive knowledge of the MBE system which paved the basis of my work. Significant thanks is expressed towards Victoria Jarvis and Jim Britten of the McMaster analytical x-ray diffraction facility (MAX), Elna Luckham and Zeynel Bayindir of the Biointerfaces Institute (BI), and Chris Butcher and Travis Casagrande of

the Canadian Center for Electron Microscopy (CCEM). Victoria and Jim were crucial in understanding MBE growth quality, and my collaborations with them were an important part of my work. Elna and Zeynel were essential in helping me understand optical properties through use of the BI's FTIR microscope. Chris and Travis trained me on multiple high resolution SEM systems that I amassed hundreds of user hours on that were necessary to characterize my samples before, during, and after numerous processing steps. Outside of McMaster, a thanks to Alex Tsukernik from the Toronto Nanofabrication Center (TNFC) at the University of Toronto who assisted in electron beam lithography (EBL), and the Quantum Nanofabrication Center (QNFC) at the University of Waterloo for allowing my use of their cleanroom facilities. Overall, this work was supported by the High Throughput and Secure Networks Challenge Program at the National Research Council of Canada and the Natural Sciences and Engineering Research Council of Canada.

Finally, I want to thank my family; my mother, step-father, younger brother, and younger sister. Their support, both emotionally and financially, during my undergraduate and graduate studies can never be repaid. As a first-generation university student, although my interest in the physical sciences may not be fully understood, being given the opportunity to pursue my academic interests is something given to me by my mother that she could not pursue herself, and is something that will never be forgotten. A final thanks to my partner, Cody, who motivated me over these past years as I completed my degree. His support while I worked my way through the final year of my undergraduate degree, and through the years of my graduate studies as I navigated new interests, motivations, and academic pathways, will always be cherished.

Table of Contents

Lay Abstract	iii
Abstract	iv
Acknowledgements	vi
List of Figures and Tables	x
Chapter 1 – Introduction.....	1
1.1 Early History of Infrared Technologies	1
1.2 Photodetector Operating Principles.....	3
1.2.1 <i>Crystal Structure and the Bandgap</i>	4
1.2.2 <i>The p-n Junction</i>	8
1.2.3 <i>Photodetector Operation</i>	12
1.3 Modern Infrared Photodetector Technology	16
1.3.1 <i>Hg_{1-x}Cd_xTe (MCT)</i>	16
1.3.2 <i>Alternative IR Materials to MCT</i>	18
1.3.3 <i>Optical Properties of Nanowires (NWs)</i>	23
1.4 Thesis Goal and Outline	25
1.5 References	26
Chapter 2 – Experimental Methods and Characterization Techniques.....	31
2.1 Characterization Methods.....	31
2.1.1 <i>Scanning Electron Microscopy</i>	31
2.1.2 <i>X-ray Diffraction</i>	34
2.1.3 <i>Fourier-transform Infrared Spectroscopy</i>	36
2.1.4 <i>The Hall Effect</i>	40
2.2 Top-down Pillar Fabrication Method	41
2.2.1 <i>Molecular Beam Epitaxy</i>	42
2.2.2 <i>Electron Beam Lithography and Ti Mask</i>	46
2.2.3 <i>Reactive Ion Etching</i>	48
2.2.4 <i>Focused Ion Beam Etching</i>	50
2.3 References	51
Chapter 3 – InSb Nanowires for Multispectral Infrared Detection.....	53
3.1 Abstract	53
3.2 Introduction.....	54
3.3 Experimental Details and Results.....	55
3.3.1 <i>Thin Film Growth and Characterization</i>	55

3.3.2	<i>Nanowire Fabrication and Characterization</i>	59
3.4	Discussion	63
3.5	Conclusion	69
3.6	References	69
Chapter 4 – InAsSb Pillars for Multispectral Long-wavelength Infrared Absorption		71
4.1	Abstract	71
4.2	Introduction	72
4.3	Material and Methods	74
4.4	Results and Discussion	77
4.5	Conclusion	85
4.6	References	85
Chapter 5 – IV Characterization of InSb Photoconductor and Photovoltaic Devices		90
5.1	Introduction	90
5.2	Experimental Details	91
5.2.1	<i>Thin Film Growth</i>	91
5.2.2	<i>Photolithography and Pattern Description</i>	93
5.3	Results and Discussion	98
5.3.1	<i>SEM and FTIR of InSb Thin Films</i>	98
5.3.2	<i>Dark J-V Characteristics of InSb Photoconductor Devices</i>	100
5.3.3	<i>Dark J-V Characteristics of InSb Photovoltaic Devices</i>	102
5.3.4	<i>Photocurrent Results</i>	103
5.4	Preliminary InSb Pillar Device	105
5.4.1	<i>InSb Pillar Device Fabrication</i>	105
5.4.2	<i>InSb Pillar Dark Current Results</i>	107
5.4.3	<i>InSb Pillar Photocurrent Results</i>	108
5.5	Conclusion	111
5.6	References	112
Chapter 6 – Focused Ion Beam Etching of Single Pillar Structures		113
Chapter 7 – Conclusion and Future Prospects		117
7.1	Thesis Summary	117
7.2	Future Prospects	119
7.3	References	120

List of Figures and Tables

- 1.1 – Atom arrangements (beige spheres) for the a) Cubic, b) Body-Centered Cubic, and c) Face-Centered Cubic lattice arrangements.
- 1.2 – Schematic diagram of a simplified electronic band structure demonstrating the presence of a bandgap.
- 1.3 – Schematic representation of an abrupt p-n junction depicting the diffusion of charge carriers, the built-in potential V_0 , the depletion region width w_0 , the bandgap energy E_g , and the Fermi level energy E_f .
- 1.4 – Schematic representation of the general operating principle of a general photodiode detector. Incident illumination of an energy sufficient to excite electrons across the bandgap generates EHPs in the depletion region.
- 1.5 – Schematic representation of an abrupt p-n junction between p-type and n-type semiconductors with an applied a) forward bias, and b) reverse bias.
- 1.6 – Bandgap tuning of $\text{In}_x\text{Ga}_{1-x}\text{As}$, $\text{Hg}_{1-x}\text{Cd}_x\text{Te}$, and $\text{InAs}_{1-x}\text{Sb}_x$, by altering material composition.
- 1.7 – Schematic representation of two NW p-i-n junction constructions, layered axially along the NW length, and a core-shell structure forming a radial p-i-n structure.
- 2.1 – Schematic depicting the interaction volume that a beam of incident electrons creates with a sample under investigation, and the relative positions of detectable emissions used for imaging.
- 2.2 – Depiction of Bragg's law, outlining the condition for constructive interference between incident X-rays reflecting off atomic planes.
- 2.3 – Schematic layout of the Vertex 70/80v and Hyperion 3000 microscope setup used for FTIR measurements. Beam paths in the Hyperion are labeled with R and T for reflectance and transmittance, respectively. The interferometer in the Vertex is highlighted. The mirror arrangement is simplified.
- 2.4 – Schematic demonstrating probe arrangement for a Hall effect measurement.
- 2.5 – Depiction of the top-down fabrication process used to obtain the large diameter pillars.
- 2.6 – Depiction of the various growth modes that diffusing adatoms may undergo to lead to thin film formation. a) Frank van der Merwe (layers), b) Volmer-Weber (islands), and c) Stranski-Krastanov (layer + islands).

- 2.7 – Layout of the EBL pattern used for mask fabrication on InSb and InAsSb thin films. Pitches were varied moving down columns, and diameters were varied moving along rows.
- 2.8 – Schematic of an ICP-RIE etch chamber depicting the sample stage electrode for RF power, the generated plasma, positive ions in the ion sheath above the sample, and the induction coils around the chamber to direct ion motion.
- 3.1 – Plan view SEM images of InSb thin films grown (a) without an AlSb buffer layer at 550 °C, and with an AlSb buffer layer at (b) 500 °C, (c) 550 °C, and (d) 600 °C. Insets show the corresponding (220) X-ray diffraction pole figures. The scale bar in (d) indicates 5 μm , applicable to all images.
- 3.2 – (a) 30° tilted SEM image of PMMA A5 resist showing an EBL pattern of holes with a pitch of 1000 nm and diameter of 400 nm. (b) Plan view SEM image of Ti mask remaining after liftoff for a pitch of 1500 nm and diameter of 600 nm. The scale bar indicates 5 μm for both images.
- 3.3 – 30° tilted SEM images of InSb NW arrays with diameter (D) and pitch (P) of (a) D = 300 nm, P = 2000 nm; (b) D = 500 nm, P = 2000 nm; (c) D = 700 nm, P = 2000 nm; (d) D = 900 nm, P = 3000 nm; (e) D = 1100 nm, P = 3000 nm, and (f) D = 1300 nm, P = 3500 nm. The scale bar in (f) indicates 3 μm , applicable to all images.
- 3.4 – The top and base diameter of NWs obtained by SEM as compared to the Ti disc diameter (dashed line) for the indicated pitches (P: 1000 nm, 2000 nm, 3000 nm). The colored lines are a guide to the eye.
- 3.5 – (a) TEM image of NWs with top diameter of 300 nm and pitch of 1000 nm. The space between NWs is filled with Pt for the FIB process. The scale bar depicts 0.5 μm . (b) Electron diffraction pattern from the selected area indicated by a circle in (a). The scale bar depicts 5 nm^{-1} . (c) EDX line scan along the length of a NW, showing the NW composition. Green, red, and blue represent In, Sb and Si, respectively. The scale bar depicts 1 μm .
- 3.6 – (a) FTIR absorbance spectra of NW arrays with the indicated diameter (D) and pitch (P). (b) Simulated absorbance spectra.
- 3.7 – Schematic (not to scale) of possible NW IR sensor.
- 3.8 – FTIR results demonstrating the absorbance before (dashed) and after (solid) an HF etch performed on InSb NWs. Arrays presented have D: 500 nm, 600 nm, 700 nm and P: a) 2000 nm and b) 3000 nm.

- 3.9 – 30° tilt SEM images of a D: 1500 nm P: 4000 nm NW array (a) before and (b) after a 45 s HF etch for Ti mask removal. The scale bar in (a) corresponds to 1 μm and applies to both images.
- 3.10 – SEM images taken with the FEI Magellan 400 of two NW arrays post-HF etch to remove the Ti mask. (a) P: 1000 nm D: 300 nm, and (b) P: 2000 nm D: 800 nm. The scale bar in (b) corresponds to 1 μm and is applicable to both images.
- 4.1 – Plan view SEM images of InAsSb thin films for (a) sample A (undoped), (b) sample B (Be doped), and (c) sample C (Te doped). The scale bar in (c) corresponds to 2 μm and is applicable to all images.
- 4.2 – 220 Pole figures of InAsSb thin films from (a) sample A (undoped), (b) sample B (Be doped) and (c) sample C (Te doped). The insets are single 2D frames from each 3D texture scan, taken from a similar region of reciprocal space, showing 200, 220 and 311 diffraction features for the corresponding samples.
- 4.3 – Twinning by 180° (or $\pm 60^\circ$) rotation about the [111] face of InAs_{1-x}Sb_x. Regions of multiple layer twinning account for the diffuse scattering observed in the 3D diffraction pattern. Twin planes are indicated by yellow lines.
- 4.4 – 30° tilted SEM images of InAsSb pillars, corresponding to arrays with (a) 4000 nm pitch and 1900 nm diameter, (b) 4000 nm pitch and 2300 nm diameter, (c) 5000 nm pitch and 3500 nm diameter, and (d) 6000 nm pitch and 4000 nm diameter. The scale bar in (d) corresponds to 20 μm and is applicable to all images.
- 4.5 – (a) FTIR absorptance spectra of InAsSb pillar arrays with different diameter (D) and pitch (P), absorptance from the as-grown thin film (black line), and absorptance from the Si substrate (dashed line). Arrows indicate the peak absorptance wavelengths. (b) Peak absorptance wavelength versus diameter for the HE₁₁ mode. Solid circles are InSb pillars (chapter 3) and InAsSb pillars (chapter 4). Solid line shows the theoretical fit to the MWIR results obtained from Ref. [4.13], dashed line is the linear fit to experimental data.
- 5.1 – (a) Cross-sectional view of thin film growth and photovoltaic device structure. (b) Schematic of the photoconductive device.
- 5.2 – Schematic depicting Au the patterns for contacting the InSb thin film. (a) The photoconductor interdigitated finger pattern with various finger width (W) and separation (S) combinations in a 4x4 array, along with a magnified example of a single width and separation combination. (b) The photovoltaic top-contact pattern demonstrating the square pattern for the thin Ti windows (grey) and the Au overlay (yellow) used to border the Ti windows for electrical probing.

- 5.3 – SEM images of the completed interdigitated finger top-contact for photoconductive studies. The finger separations presented in all images is 5 μm . The finger widths are a) 10, b) 30, and c) 100 μm . Image d) depicts W10 S5 at a higher magnification, showing the end of an individual finger.
- 5.4 – Analysis of InSb thin films. (a) Plan view SEM image of the p-i-n InSb thin film growth. (b) FTIR results comparing measured undoped InSb data (black-solid) to expected data (black-dashed), and to p-i-n structured InSb on an As doped ($< 0.005 \Omega\cdot\text{cm}$) Si (100) substrate (red-solid).
- 5.5 – Dark J-V characteristics for select finger width and separation combinations presented on a semi-log plot. The inset depicts the same data in a linear plot.
- 5.6 – Dark J-V characteristics demonstrating the trends for (a) a fixed finger separation, and (b) a fixed finger width.
- 5.7 – Dark J-V characteristics for select square contact areas on a semi-log plot. The inset depicts the same data in a linear plot.
- 5.8 – Measured photocurrent obtained from the InSb photoconductor and photovoltaic devices. The photoconductor device under (a) IR illumination and (b) solar illumination and the photovoltaic device under (c) IR illumination and (d) solar illumination. The inset of c and d present the photocurrent on a smaller current range.
- 5.9 – (a) SEM images of back-etched BCB-coated InAsSb pillar structures. (b) FTIR results demonstrating the effect of back-etched BCB on pillar absorption for a select array of D: 1700 nm and P: 4000 nm. FTIR performed on a $\sim 2.6 \mu\text{m}$ thick BCB layer on the same undoped Si (100) substrate is included for comparison.
- 5.10 – Dark J-V characteristics for four InSb pillar diameter and pitch combinations presented on a semi-log plot. The inset depicts the same data in a linear plot.
- 5.11 – J-V characterization under IR illumination compared to dark current for the pillar array with D: 1100 nm and P: 3000 nm on a semi-log plot. The inset depicts a linear plot.
- 5.12 – (a) Photocurrent measured for each pillar array taken under full IR illumination. (b) Photocurrent measured for the D: 900 nm P: 3000 nm pillar array taken under filtered IR illumination.
- 6.1 – Plan view SEM images taken with the FEI Magellan of (a) the initial etch consisting of a single pillar, a 2x2 array, and a 3x3 array, and (b) the second etch consisting of 2 single pillars of different diameters, and two 2x2 arrays with one containing pillars of the same diameter, and the next containing pillars of varying diameters. The scale bar applies to both images.

- 6.2 – 30° tilted SEM images taken of the initial and second FIB etches depicting (a) a single 1.7 μm diameter pillar, (b) a 2x2 array of 1.7 μm diameter pillars, (c) a 3x3 array of 1.7 μm diameter pillars, (d) a single 1 μm diameter pillar, (e) a 2x2 array of 1.7 μm pillars, and (f) a 2x2 array of a 1.1 μm, 1.5 μm, 1.9 μm, and 2.3 μm diameter pillar. The scale bar in (f) is applicable for all images.
- 6.3 – FTIR results obtained for (a) the initial etch pattern, and (b) the etch pattern done to reduce undercutting into the substrate.
- 6.4 – (a) SEM image of the 2x2 array consisting of pillars of varying diameters and a 5000 nm pitch. (b) EDS mapping of Si presented in blue. (c) EDS mapping of Ga presented in purple. Signal from In, As, and Sb was present representing the pillar and surrounding thin film and is omitted.
- 7.1 – Complete FTIR results for InSb (dashed) and InAsSb (solid) pillars.
- 7.2 – Potential device structure for a p-i-n InSb pillar array.

Chapter 1 – Introduction

1.1 Early History of Infrared Technologies

Infrared (IR) light was first discovered in the year 1800 by William Herschel using a prism and a thermometer [1.1, 1.2]. In his experiment, the prism was used to separate sunlight into a spectrum on his workbench (figure 1.1), and he was interested in measuring each colored region with a thermometer and comparing the temperature change with a reference elsewhere in the room to better understand the energy distribution of the sun's rays. He observed that for the thermometer being exposed to visible light, the temperature reading increased as the thermometer was moved through the visible spectrum from violet to red light. He noted, however, that the highest temperature increase occurred beyond visible red light, in an uncolored region of the workbench. Herschel called the rays incident on this region "calorific rays"; they were invisible yet transmitted the highest amount of heat. With the use of a thermometer, he confirmed that these invisible rays refracted and reflected, as with visible light. With the first observation of these invisible rays came the need for a formal way of detecting their presence. The result of this was that many early IR technologies operated on the basis of temperature, a branch of detector technology called thermal detectors.

In the year 1821, Thomas Seebeck discovered the thermoelectric effect and demonstrated the first thermocouple, allowing for a temperature difference in a conductive material to induce an electric potential. This effect is called the Seebeck effect and demonstrates a linear dependence of a generated voltage ΔV based on material properties

and the temperature difference $\Delta T = T_{hot} - T_{cold}$ between the hot and cold sides of the material [1.3]. He further solidified the existence of the invisible IR rays observed by Herschel by analyzing heat distributions through prisms of varying materials [1.4]. The thermocouple was later refined into the more sensitive thermopile by Leopoldo Nobili in 1829, and it was demonstrated to measure the IR radiation emanating from a person 25-30 feet away, and showed that a caterpillar always emanated a higher temperature from its body than the butterfly that followed [1.5,1.6]. Initial astronomical measurements performed with thermocouple technology were performed in 1856 when Charles Piazzzi Smythe detected IR radiation from the moon, leading to a more advanced thermopile-based detector being used in 1915 by William Coblentz of the U.S National Bureau of Standards to measure the IR radiation emanating from 110 distant stars [1.7]. In the year 1878, Samuel Langley developed the bolometer [1.8]. This device operated based on a temperature dependent resistance, whereas the thermocouple operated based on the thermoelectric effect, allowing for incident IR radiation to alter a material's temperature, allowing for measurable changes in its electrical properties. At the time, the bolometer advanced to be able to detect the heat emanating from a cow from a quarter of a mile away. These early IR detection technologies operated due to temperature differences and a material's thermal properties. In general, these thermal detectors have a slow response due to the requirement of a temperature change and do not offer any wavelength information or specificity from the emitting body [1.9].

Another branch of detector technology called photon detectors was developed during the early 1900's with the first IR photoconductor developed in 1917 by Case [1.10]. Such

a photoconductor device functions based on photon absorption within the material, exciting electrons in the photoconductor's crystal structure. As the wavelength of incident light being absorbed is dependent on the detector's material properties, wavelength specificity can be obtained in photon detectors. In 1933 Kutzscher found that the naturally occurring mineral galena, comprised of PbS, was a photoconductive material and had an absorption response up to about 3 μm in the IR region [1.11]. Eventually, such IR detectors utilizing PbS photoconductors were used for the first IR survey of the sky. The observations done at the Mount Wilson Observatory covered 75% of the sky and found upwards of 20,000 IR sources, including stars and other objects that were never seen before using visible light observations. Photon detectors are the branch of IR detector focused on in this thesis.

1.2 Photodetector Operating Principles

As mentioned, photon detectors are the primary branch of photodetector that will be discussed in this work. The most common example of a photodetector consists of a semiconductor containing a p-n junction, referred to as a photodiode, and this section covers the physics of the p-n junction and the origination of a bandgap. Photon detectors, as opposed to thermal detectors, can allow for wavelength specificity during detection. In brief, the semiconductor chosen allows for wavelength selection of the absorbed light based on the semiconductor's bandgap energy E_g . If light is of sufficient energy, it will excite electrons across the bandgap and be absorbed. The p-n junction within a semiconductor is an abrupt junction in which the semiconductor transitions from being p-type doped to n-type doped. A p-type dopant is a dopant with fewer valence electrons than the atoms making

up the semiconductor's crystal structure and will induce a majority of holes, which are positively charged vacancies created by absent electrons that can travel through the material. The n-type dopant contains more valence electrons than the atoms making up the semiconductor and this induces an electron majority. The hole and electron majority sides meeting at the p-n junction will cause diffusion of majority carriers to the opposite side of the junction, forming the depletion region, and creating a built-in potential. This potential causes optically generated electron-hole pairs (EHPs) to be swept to their majority side and collected by metal contacts on the semiconductor device. Information in the following sections pertaining to semiconductor physics comes primarily from references [1.12-1.15].

1.2.1 Crystal Structure and the Bandgap

The primitive basis vectors **a**, **b**, and **c** can be used to describe the arrangement of atoms in a crystalline solid. Given some point in the solid, any other equivalent point in the crystal can be reached through a linear combination of the basis vectors,

$$\mathbf{R} = m\mathbf{a} + n\mathbf{b} + p\mathbf{c} \quad (1.1)$$

where *m*, *n* and *p* are integers. The set of vectors **R** that are linear combinations of the basis vectors will define the crystal lattice sites of the solid. Some simple crystal lattice arrangements include the cubic, body-centered cubic, and face-centered cubic arrangements. These arrangements consist of a simple arrangement of atoms centered on the corner of repeated cubes, with the body-centered arrangement having one extra atom at the center of the cube, and the face-centered arrangement having an extra atom at the center of the cubes faces. These are shown in figure 1.1.

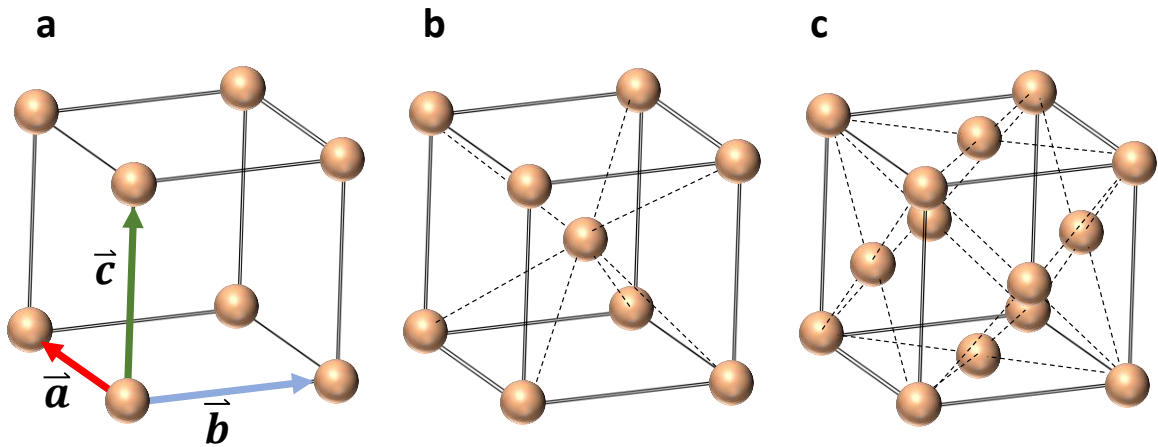


Figure 1.1 Atom arrangements for the a) cubic, b) body-centered cubic, and c) face-centered cubic lattice arrangements.

More complicated crystal arrangements exist, such as the diamond and zincblende arrangements. The diamond arrangement is such that each atom is surrounded by 4 equidistant neighboring atoms, with the neighboring atoms creating the corners of a tetrahedron. The zincblende arrangement is the same in terms of atom positions in the lattice; however, the 4 neighbors of the tetrahedral organization are a different atomic species. These lattice structures are taken on by important semiconductors such as Si with a diamond structure, and GaAs with a zincblende structure. All III-V compounds crystallize in the zincblende arrangement in bulk with the exception of nitrides [1.16-1.18]. III-N compounds may also take on the wurtzite crystal structure, a closely related structure to zincblende which also takes on a tetrahedral organization of neighboring atomic species with a different atomic stacking arrangement.

The energy-momentum relationship of a crystalline solid, usually called the band structure, is determined by the material's crystal structure and the atomic species involved.

The band structure is obtained by solving the Schrödinger equation for an electron experiencing a potential exerted on it by the atoms in the lattice. The Bloch theorem states that for the Schrödinger equation,

$$\left[-\frac{\hbar^2}{2m} \nabla^2 + V(\mathbf{r}) \right] \phi_{\mathbf{k}}(\mathbf{r}) = E_{\mathbf{k}} \phi_{\mathbf{k}}(\mathbf{r}) \quad (1.2)$$

for a potential $V(\mathbf{r})$ with the periodicity of the crystal lattice, the solution will be of the form,

$$\phi_{\mathbf{k}}(\mathbf{r}) = e^{i\mathbf{k}\cdot\mathbf{r}} U_{\mathbf{n}}(\mathbf{k}, \mathbf{r}) \quad (1.3)$$

where $U_{\mathbf{n}}$ is periodic with the periodicity of the crystal lattice. From this it can be shown that the energy $E_{\mathbf{k}}$ is periodic in crystal momentum \mathbf{k} . To understand the periodicity of the energy in the crystal structure it is useful to look at the reciprocal lattice. For a given set of basis vectors for the crystal lattice, the vectors,

$$\mathbf{a}^* = 2\pi \frac{\mathbf{b} \times \mathbf{c}}{\mathbf{a} \cdot \mathbf{b} \times \mathbf{c}} ; \mathbf{b}^* = 2\pi \frac{\mathbf{c} \times \mathbf{a}}{\mathbf{a} \cdot \mathbf{b} \times \mathbf{c}} ; \mathbf{c}^* = 2\pi \frac{\mathbf{a} \times \mathbf{b}}{\mathbf{a} \cdot \mathbf{b} \times \mathbf{c}} \quad (1.4)$$

define the reciprocal lattice basis vectors. The original basis vectors are referred to as direct basis vectors. The reciprocal vectors are perpendicular to the sets of planes formed by the direct basis vectors and are normalized to the direct lattice's unit cell volume. Since $E_{\mathbf{k}}$ is periodic, we can use \mathbf{k} vectors in the primitive unit cell of the reciprocal lattice, called the Brillouin zone. Any vector beyond the Brillouin zone can be written as a vector within it due to the periodicity of the crystal lattice. Various numerical methods have been used to solve the band structure of different semiconductor materials. The band structures of Ge

and InSb are presented in [1.19], with a basic representation of a band structure shown in figure 1.2.

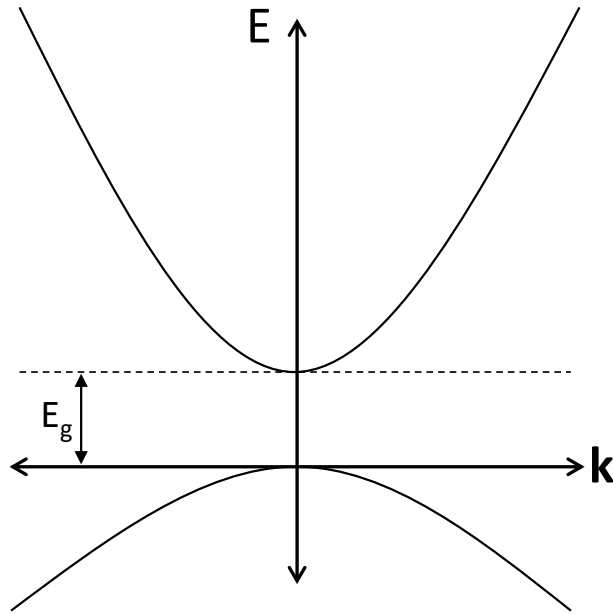


Figure 1.2 Schematic diagram of a simplified electronic band structure demonstrating the presence of a bandgap.

In figure 1.2, the horizontal axis denotes the \mathbf{k} vector and points of symmetry within the Brillouin zone. There is a gap separating the maximum of the lower energy bands (the valence band) and the valley of the upper energy bands (the conduction band). This energy separation is the bandgap, E_g . The bandgap varies in size depending on the semiconductor, ranging from very narrow bandgap semiconductors such as InAsSb alloys (0.08-0.35 eV @ 300 K) and InSb (0.17 eV @ 300 K) to larger bandgaps such as GaAs (1.43 @ 302 K) [1.20, 1.21]. InSb and InAsSb alloys having a narrow bandgap makes them a semiconductor

material capable of acting in the infrared regime. The bandgap is also temperature dependent with the dependency given by the Varshni equation [1.22],

$$E_g(T) = E_g(0) - \frac{\alpha T^2}{T + \beta} \quad (1.5)$$

where α and β are material parameters. In general, E_g decreases with increasing T .

1.2.2 The p-n Junction

In an intrinsic semiconductor, a semiconductor with no external doping, the number of occupied levels in the conduction band is given by,

$$n = \int_{E_c}^{E_{\max}} N(E)F(E) dE \quad (1.6)$$

where E_c is the energy at the bottom of the conduction band (coinciding with E_g), E_{\max} is the energy at maximum of the conduction band, $N(E)$ is the density of states, and $F(E)$ is the Fermi-Dirac distribution. The density of states $N(E)$ is defined as,

$$N(E) = \frac{dn(E)}{dE} \quad (1.7)$$

and will yield information on the number of electrons per material volume $n(E)$ situated at certain energy ranges dE . The Fermi-Dirac distribution $F(E)$ is given as,

$$F(E) = \frac{1}{1 + \exp\left(\frac{E - E_f}{kT}\right)} \quad (1.8)$$

and gives us the probability of occupancy of an energy level. The Fermi energy E_f is the energy at which the probability of occupancy is 0.5, and for an intrinsic semiconductor it

falls near half the value of the bandgap energy. It can be found that the resulting expression for the number of electrons in the conduction band in equilibrium conditions becomes,

$$n_0 = 2 \left(\frac{2\pi m_e^* kT}{h^2} \right)^{\frac{3}{2}} \exp\left(-\frac{E_c - E_f}{kT}\right) = N_c \exp\left(-\frac{E_c - E_f}{kT}\right) \quad (1.9)$$

where m_e^* is the electron effective mass, and the subscript on n indicates equilibrium conditions. Similarly for holes in the valence band, we find that,

$$p_0 = 2 \left(\frac{2\pi m_h^* kT}{h^2} \right)^{\frac{3}{2}} \exp\left(-\frac{E_f - E_v}{kT}\right) = N_v \exp\left(-\frac{E_f - E_v}{kT}\right) \quad (1.10)$$

where m_h^* is the hole effective mass. The intrinsic carrier concentration of the semiconductor is found as,

$$n_i^2 = p_i^2 = n_0 p_0 = N_c N_v \exp\left(-\frac{E_g}{kT}\right) \quad (1.11)$$

To form a p-n junction and create a photodiode for detector applications, the semiconductors are doped with donor and acceptor atoms. Donor atoms (n-dopants) are atoms with more valence electrons than those making up the semiconductor and will contribute excess electrons to the crystal lattice making the semiconductor n-type. Acceptor atoms (p-dopants) have fewer valence electrons than those making up the semiconductor and will remove electrons from the crystal lattice, creating positively charged vacancies called holes and make the semiconductor p-type. If we assume that ambient temperature is enough to ionize most donor or acceptor atoms, and that the dopant concentration is much higher than the intrinsic carrier concentration, we can say for an n-doped semiconductor

that $n_0 \approx N_d$ where N_d is the number of donor atoms. Similarly for a p-doped semiconductor, $p_0 \approx N_a$ where N_a is the number of acceptor atoms. So, we find that,

$$\text{n-type material:} \quad p_0 = \frac{n_i^2}{N_d} \quad (1.12)$$

$$\text{p-type material:} \quad n_0 = \frac{n_i^2}{N_a} \quad (1.13)$$

Considering some semiconductor material, the Fermi energy level depends on the doping. In an n-type semiconductor, donor atoms will introduce excess electrons and electrons will be the majority charge carrier. In a p-type semiconductor, acceptor atoms will introduce excess holes and holes will be the majority charge carrier. In an n-type material, the Fermi energy level will shift to be closer to the conduction band, and in a p-type material the Fermi energy level will shift to be closer to the valence band. When an abrupt p-n junction is introduced in a semiconductor material, the diffusion and drift of charge carriers will occur. The diffusion of charge carriers occurs due to the introduced concentration gradient causing majority charge carriers to diffuse across the junction and become minority carriers. The drift of charge carriers occurs due to a potential difference created at the junction by the diffusing charge carriers, called the built-in potential. The current density of electrons experiencing drift and diffusion is given by,

$$J_n(x) = J_{n,\text{drift}} + J_{n,\text{diffusion}} = q\mu_n n \varepsilon + qD_n \frac{dn}{dx} \quad (1.14)$$

with an analogous expression for holes. q is the fundamental charge of the electron, μ is the carrier mobility, ε is the electric field, and D_n is a constant of proportionality describing the flux of electrons diffusing due to a concentration gradient $\frac{dn}{dx}$. For a p-n junction in

equilibrium, the drift and diffusion currents will cancel one another. The built-in potential across the p-n junction is given by,

$$V_0 = \frac{kT}{q} \ln \left(\frac{N_a N_d}{n_i^2} \right) \quad (1.15)$$

The built-in potential is dependent on the donor and acceptor concentrations on the n and p sides of the junction, respectively. The increase of charge carriers will result in more carriers capable of diffusing across the p-n junction, leading to a higher potential difference between them. The diffusion of charge carriers across the p-n junction into a side where they are a minority carrier introduces the possibility of recombination. If a charge carrier has some lifetime τ before recombination can occur, on average only a certain distance can be traveled into the region where it is a minority carrier before electron relaxation occurs and the EHPs recombine.

The width of the depletion region is given by,

$$w_0 = \sqrt{\frac{2\epsilon_0\epsilon_r V_0}{q} \left(\frac{1}{N_a} + \frac{1}{N_d} \right)} \quad (1.16)$$

where ϵ_0 is the permittivity of free space and ϵ_r is the relative permittivity of the semiconductor. As with the built-in potential V_0 , the depletion region width w_0 is dependent on acceptor and donor concentrations. These parameters are presented schematically in figure 1.3.

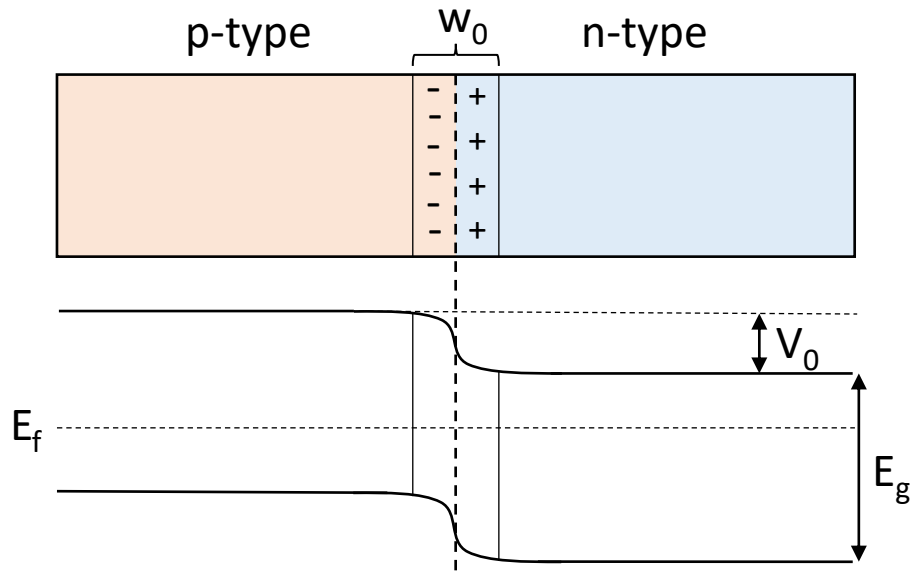


Figure 1.3 Schematic representation of an abrupt p-n junction depicting the diffusion of charge carriers, the built-in potential V_0 , the depletion region width w_0 , the bandgap energy E_g , and the Fermi level energy E_f .

1.2.3 Photodetector Operation

In the previous sections, the basic physics of an abrupt p-n junction was discussed. The origination of some key parameters such as the bandgap energy E_g , the depletion region width w_0 , and the built-in potential V_0 were mentioned. For some given semiconductor of a bandgap energy E_g , light incident on the semiconductor will be absorbed if the energy of the incident photon is greater than that of the bandgap energy. Electrons in the valence band are excited to the conduction band, leaving behind a hole in the valence band, and an EHP is optically generated. InAsSb alloys and InSb having a narrow bandgap energy corresponds to long wavelength absorption in the infrared region. InAsSb alloys can have a tunable absorption wavelength from $3.5 \mu\text{m}$ at InAs, $7.1 \mu\text{m}$ at InSb, and $14.7 \mu\text{m}$ at the composition $\text{InAs}_{0.36}\text{Sb}_{0.64}$. If EHPs are generated outside the depletion region, the minority

carrier will have a high probability of recombination before it can cross the junction where it is a majority carrier. Due to this, EHP generation in the depletion region is favorable. If an EHP is generated in the depletion region, it will have the shortest possible distance to travel to reach its majority carrier side, and it will be experiencing the strong built-in potential V_0 that will sweep the carriers to their majority side of the junction. This reduces the probability for recombination to occur and improves the efficiency of the device. This operating principle is presented schematically in figure 1.4.

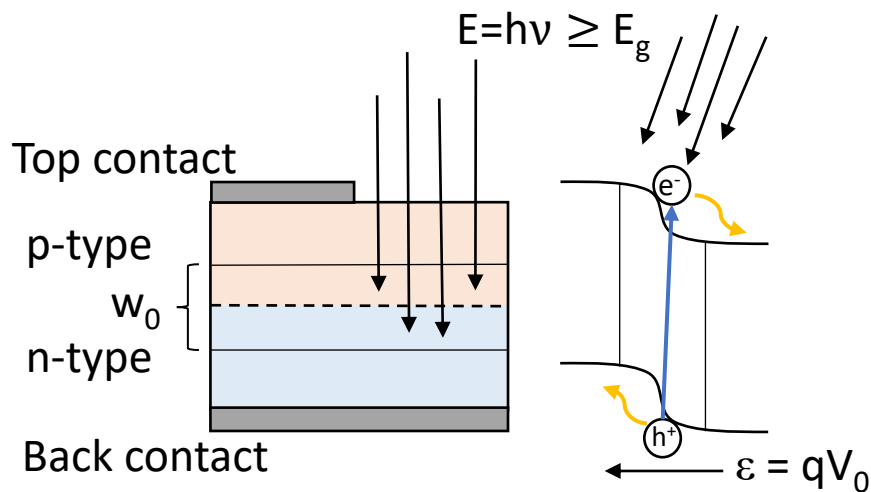


Figure 1.4 Schematic representation of the general operating principle of a photodiode detector. Incident illumination of an energy sufficient to excite electrons across the bandgap generates EHPs in the depletion region.

Reducing the probability of unwanted recombination is of utmost importance for device function. To further assist in charge carrier collection, the p-n junction can be biased, removing equilibrium conditions, and allowing a net current to flow. If light is incident on the photodiode, this current flow is dominated by optically generated current under reverse

bias (negative applied voltage). When an external voltage V is applied across the p-n junction, the depletion region width is altered as follows,

$$w_{\text{bias}} = \sqrt{\frac{2\epsilon_0\epsilon_r(V_0 - V)}{q} \left(\frac{1}{N_a} + \frac{1}{N_d} \right)} \quad (1.17)$$

It can be seen that the external voltage acts to decrease the built-in potential if it is positive, i.e., the photodiode is forward biased. A small forward bias is the regime that solar cells operate under to generate power. This forward bias results in a decrease of depletion region width and causes a net current flow through the photodiode. If the photodiode is reverse biased, the applied voltage acts to increase the built-in potential and increases the width of the depletion region. Photodetectors operate under a reverse bias. Under the reverse bias condition, the optically generated current can be effectively collected and discerned from the overall current flow as the increased V_0 and w_0 allow for photogenerated EHPs to be more readily collected; however, power is consumed to do so, rather than being produced with the solar cell's forward bias operation. The overall current flow through a biased photodiode is given by the diode equation as follows,

$$I = qA \left(\frac{D_n}{L_n} n_p + \frac{D_p}{L_p} p_n \right) \left(\exp\left(\frac{qV}{kT}\right) - 1 \right) \quad (1.18)$$

where the term,

$$I_0 = qA \left(\frac{D_n}{L_n} n_p + \frac{D_p}{L_p} p_n \right) \quad (1.19)$$

is the reverse saturation current under reverse bias. This reverse saturation current is diffusion dominated. Under illumination, the photogenerated current dominates over the

reverse saturation current in the reverse bias, and shifts the measured current-voltage characteristic downwards proportionally to the photogenerated current, resulting in a final diode equation under illumination,

$$I = I_0 \left(\exp\left(\frac{qV}{kT}\right) - 1 \right) - I_L \quad (1.20)$$

where I_L is the photocurrent. These biasing situations and their corresponding energy band diagrams are shown in figure 1.5.

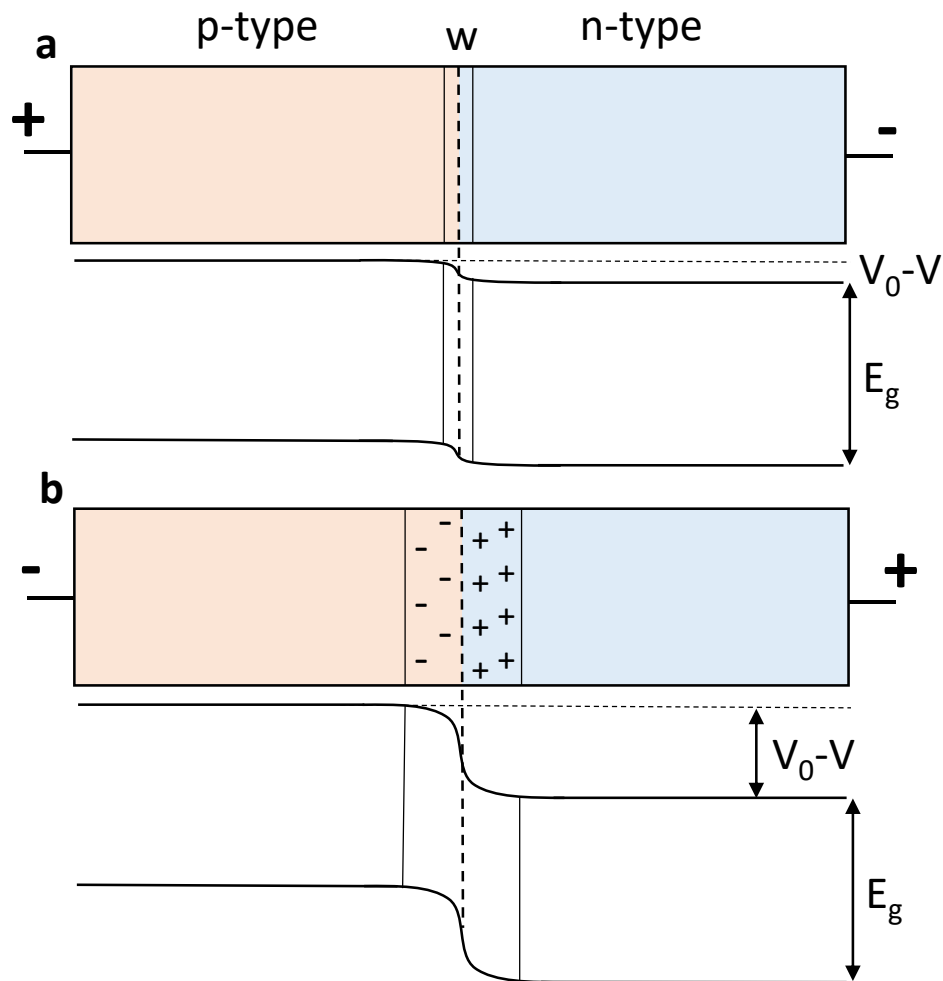


Figure 1.5 Schematic representation of an abrupt p-n junction between p-type and n-type semiconductors with an applied a) forward bias, and b) reverse bias.

1.3 Modern Infrared Photodetector Technology

1.3.1 $Hg_{1-x}Cd_xTe$ (MCT)

In the mid-20th century, Lawson et al. [1.23] reported on the physical properties of the $Hg_{1-x}Cd_xTe$ (MCT) material system. This material provided an incredible avenue for the development of IR detector technology, and MCT detector technology still proves to be the most popular to date [1.24]. The initial selling point for MCT as a material suitable for IR applications is the ability to tune the bandgap of the material over such a wide range. The bandgap of the MCT material system at room temperature can be tuned from a semimetal with $E_g = -0.14$ eV at HgTe ($x = 0$), crossing $E_g = 0$ at $x \approx 0.15$, and increasing to 1.49 eV at CdTe ($x = 1$). The bandgap as a function of x and T can be given by the following equation [1.25],

$$E_g(x, T) = -0.302 + 1.93x - 0.81x^2 + 0.832x^3 + 5.35 \times 10^{-4}(1 - 2x)T \quad (1.21)$$

This bandgap range corresponds to an absorption wavelength range that is capable of spanning 1 μm to 30 μm , covering the short-wavelength IR (SWIR) to very long-wavelength IR (VLWIR) regions of the IR spectrum. The MCT material system also has a high electron mobility μ_e . As mentioned in Eq. (1.14), the carrier mobility is a measure of either an electron or hole to effectively move through the crystal lattice under the influence of an electric field. Scattering mechanisms within the crystal lattice limit the mobility, and the mobility tends to dominate in the electrical conductivity of the material. The electron mobility of MCT at 300 K with $x = 0.18-0.25$, which corresponds to an absorption

wavelength range λ_{ab} of 5.9 μm to 6.9 μm in the mid-wavelength IR region (MWIR), can be described by the following equation [1.26],

$$\mu_e = 10^4(8.754x - 1.044)^{-1} \quad (1.22)$$

in units of $\text{cm}^2\text{V}^{-1}\text{s}^{-1}$. At the composition $\text{Hg}_{0.806}\text{Cd}_{0.194}\text{Te}$, corresponding to $E_g \approx 0.145$ eV and $\lambda_{abs} = 8.5$ μm , the electron mobility is $\mu_e = 1.5 \times 10^4$ $\text{cm}^2\text{V}^{-1}\text{s}^{-1}$. Hole mobilities μ_h range from 40 to 80 $\text{cm}^2\text{V}^{-1}\text{s}^{-1}$ at room temperature, with minimal temperature dependence, multiple orders of magnitude lower than μ_e . MCT also has the benefit of being highly lattice matched to its usual CdZnTe substrate across the entirety of its IR tunability range [1.7,1.9]. The difference in lattice parameter between CdTe and $\text{Hg}_{0.8}\text{Cd}_{0.2}\text{Te}$ is approximately 0.2%, allowing for MCT to successfully use the same substrate for varying compositions, and allowing for stacking layers of different compositions for multispectral applications.

Although MCT has ideal parameters for IR photodetection, attempts have been made to address some prominent shortcomings. Weak Hg-Te bonds lead to bulk, surface, and interface instabilities, with bulk MCT uniformity and yield being an issue. Another issue is the lattice matched CdZnTe substrate. Integration with silicon readout integrated circuits (ROIC) is difficult due to a difference in thermal expansion coefficients between CdZnTe and Si. CdZnTe is also limited in its size, with a 7x7 cm^2 substrate being the largest commercially available, limiting the size of MCT based IR focal plane arrays (FPAs). These 7x7 cm^2 substrates cost upwards of \$10,000, compared to the \$100 6-inch diameter Si substrates available, making the cost of MCT device fabrication very high [1.27].

1.3.2 Alternative IR Materials to MCT

1 – In_xGa_{1-x}As

InGaAs photodetectors are well established with applications in the near IR (NIR) wavelength range [1.9]. InGaAs photodetectors for use in the wavelength range of 1-1.7 μm are used for communication systems, low light night vision, remote sensing, range finding, and process control [1.28]. The lower dark current and noise of InGaAs compared to Ge makes it an effective material system for NIR applications. High quality photodiodes have been grown by metalorganic chemical vapor deposition (MOCVD) with performance comparable to MCT photodiodes in the NIR region [1.29].

2 – InAs_{1-x}Sb_x

InSb has the narrowest bandgap of 0.17 eV at 300 K of non-ternary alloy III-V semiconductors corresponding to $\lambda_{\text{abs}} = 7.1 \mu\text{m}$, and the highest electron mobility of $80,000 \text{ cm}^2 \text{ V}^{-1} \text{ s}^{-1}$ of relevant IR materials [1.7]. These properties alone make it a promising alternative to MCT for IR applications. Large diameter, high quality bulk InSb substrates are available, with InSb detectors used for ground-based IR astronomy. Cryogenically cooled InSb and MCT detectors have comparable array size in the MWIR region, but the wide range wavelength tunability of MCT still makes it more popular [1.30-1.33]. Wavelength tunability is achievable by alloying InSb with InAs to form InAs_{1-x}Sb_x ternary compounds. The large bowing parameter of InAs and InSb alloys allows for the bandgap to reach as low as 0.08 eV at 300 K, corresponding to $\lambda_{\text{abs}} \approx 15 \mu\text{m}$ in the LWIR region [1.20].

3 – GaAs/AlGaAs Quantum Well IR Photodetectors (QWIP)

In terms of QWIP technology, the GaAs/AlGaAs multiple quantum-well detector is the most mature [1.7, 1.9]. Large FPAs in the LWIR imaging region, comparable to high quality MCT detectors, are being fabricated [1.34-1.36]. GaAs/AlGaAs QWIPs rely on bandgap engineering and creating a repeating layered structure of alternating materials with different bandgaps. Electron accumulation in the quantum wells created by the alternating bandgap differences result in the formation of sub-bands and the possibility of electron excitation to the sub-bands from within the quantum wells formed by the repeated quantum well structure. For operation in the 7-11 μm range, Si doped ($N_d \approx 10^{18} \text{ cm}^{-3}$) 40 \AA thick GaAs is sandwiched between 500 \AA thick barrier layers comprised of $\text{Al}_x\text{Ga}_{1-x}\text{As}$ in the $x = 0.25 - 0.3$ range. This quantum well structure is repeated 50 times to produce the sub-band structure, with the ability to push further into the LWIR by decreasing the aluminum content x to 0.15 and increasing the GaAs thickness to 60 \AA . GaAs/AlGaAs QWIPs have the advantage of being based on well-known GaAs growth and processing technology, with the use of uniform and controlled molecular beam epitaxy (MBE) growths on > 6-in GaAs wafers with high yield and low cost. However, due to these benefits, the sub-band transition results in low excitation lifetimes and poor performance at temperatures > 50 K. For n-type QWIPs, the optical absorption is proportional to the incident wave's polarization component normal to the QW, meaning that photons at a normal incidence will not be absorbed. To ensure adequate absorption to compensate for these mentioned issues, the QW layers can be coupled with a diffraction grating or highly reflective surface to ensure non-normal incidence, as well as etching QW structures into pyramidal light trapping

structures. The bandgap versus composition for various material systems is shown in figure 1.6 [1.20].

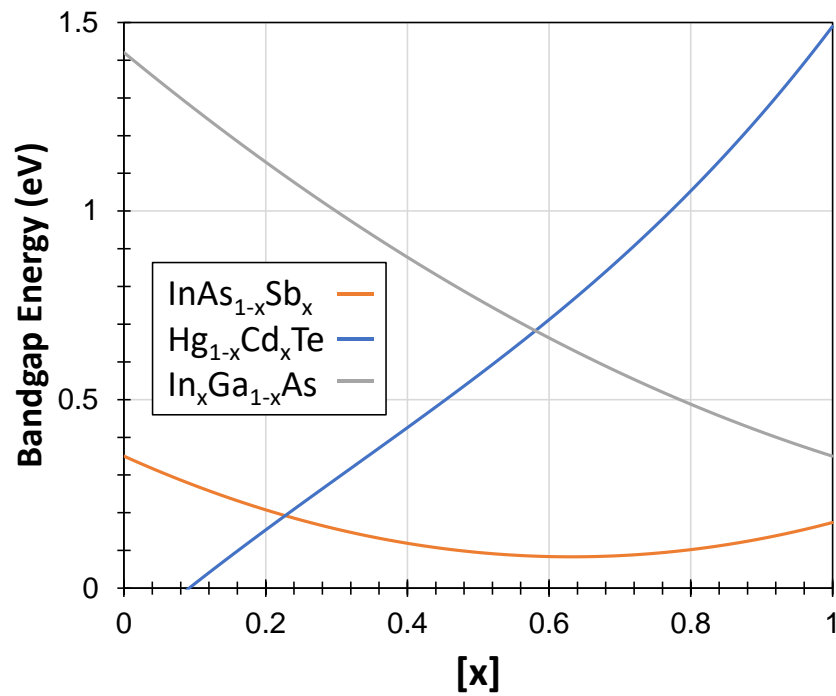


Figure 1.6 Bandgap tuning of In_xGa_{1-x}As, Hg_{1-x}Cd_xTe, and InAs_{1-x}Sb_x, by altering material composition.

4 – III-V Nanowire Arrays

Nanowire (NW) array photodetectors made of III-V materials have been fabricated and have demonstrated optical absorption in the visible to MWIR regions [1.37]. NWs are thin cylindrical nanoscale structures with lengths on the order of microns and widths ranging from tens to hundreds of nanometers. NWs are typically grown by the vapor-liquid-solid (VLS) growth method utilizing molecular beam epitaxy (MBE) or metalorganic vapor phase epitaxy (MOVPE). A foreign species seed particle such as Au can be used to initiate NW growth from a substrate, but growth without such a particle is possible through self-assisted NW growth. If growing on Si, a SiO_x mask can be formed and patterned with lithography techniques and etching to layout arrays of circular apertures in the oxide mask with varying diameters and pitches. Impinging group III material will coalesce in the holes of the mask, with the diameter and pitch of the open circles determining the diameter and the pitch of the growing NW array. The oxide mask prevents thin film or NW growth in unwanted regions. An alternative method to nanowire fabrication is top-down etching from a thin film or substrate, which was the method employed in this thesis.

The resulting NWs yield unique optical properties, and unlike other IR materials that have a large lattice mismatch with Si, the small growth area of the NW allows for lattice strain relaxation allowing for prominent IR III-V materials to be grown on cheaper Si substrates with minimal defects [1.38-1.41]. The growth process of the NWs allows for the formation of core-shell structures, in which varying compounds or doping levels are manipulated radially as opposed to along the length of the NW itself, allowing for unique p-n junction and carrier transport paths as shown in figure 1.7. Simulations of GaAs, InP,

and InAs NW arrays [1.42], and InSb NW arrays [1.43] demonstrated that manipulation of NW geometry can allow for tunability of peak absorption wavelength. In the IR region, InSb NW simulations demonstrated wavelength tunability from about 1 – 6.5 μm by altering NW diameter. InAsSb core-shell NWs in the diameter range of 440 – 520 nm were grown by catalyst-free selective-area growth with a SiO_x mask on Si (111) substrates via MBE and demonstrated diameter dependent absorption wavelength tuning from about 2-2.5 μm [1.44]. One of the first III-V NW array detectors grown was InAs on Si, demonstrating absorption in the 0.5-1 μm range [1.45]. InAs NWs on Si has also been demonstrated in the 1.4-3.3 μm range [1.46], InP NWs on InP in the 477-1240 nm range [1.47], InN NWs on Si in the 635-1550 nm range [1.48], InAsSb NWs on InAs in the 3-6 μm range exhibiting NW diameter dependent photocurrent [1.49], and InAsSb NWs on Si in the 1.5-4 μm range [1.50]. Such NW array devices have demonstrated optical absorption in the UV (with ZnO), visible, NIR, SWIR, and MWIR regions, with the possibility of extending absorption into the LWIR region being evident due to the ability to tune the bandgap of InAsSb into the LWIR region, with NW diameter dependent absorption allowing for absorption specificity and multispectral capabilities.

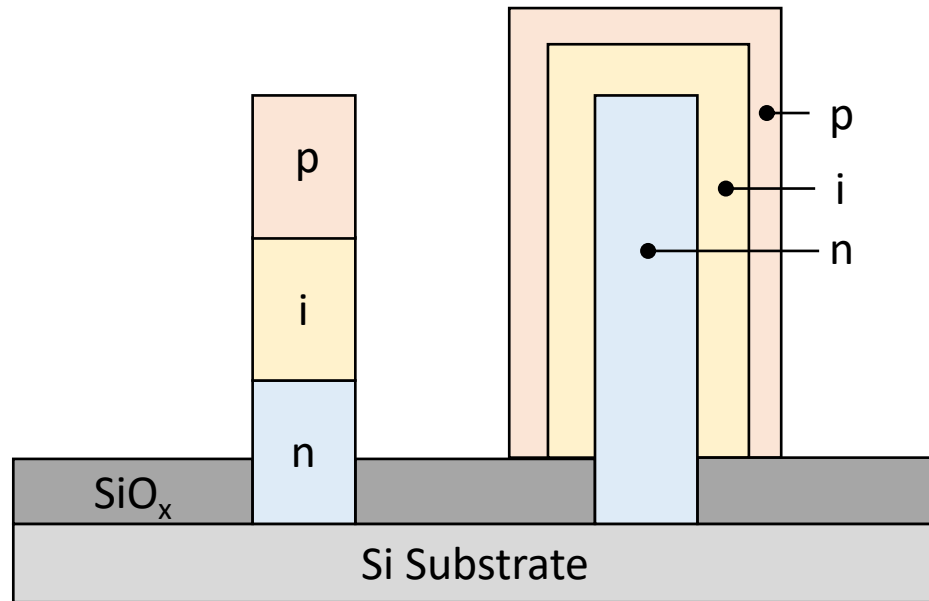


Figure 1.7 Schematic representation of two NW p-i-n junction constructions, layered axially along the NW length, and a core-shell structure forming a radial p-i-n structure.

1.3.3 Optical Properties of Nanowires (NWs)

It has been demonstrated through simulation and experiment that tuning of the absorption wavelength in NW arrays is possible due to manipulation of NW diameter and pitch. Absorption in NWs is caused primarily by three optical effects:

- **Radial mode resonances** arise due to the cylindrical symmetry of the NW, allowing for light of specific wavelengths to couple into these resonant modes. This leads to enhanced absorption at a specific wavelength by the NW material, which is a NW diameter-based phenomena. This phenomenon is the most prominent of the effects and leads to enhanced absorption in a material beyond that of a thin film of the same material [1.42-1.44, 1.51].

- **Evanescent mode coupling** occurs through nearby NWs in an ordered array and is dependent on NW pitch. A portion of the confined radial modes propagating in the NW is lost and energy decreases radially away from a given NW. This evanescent wave propagation can overlap between adjacent NWs leading to increases in absorption of the array overall, depending on NW pitch. If the array is too spread out (large pitch), evanescent coupling is insignificant, lowering overall absorption. If the array is too dense (small pitch), the NW array approaches a thin film of the given NW material, eliminating enhanced absorption through diameter dependences, and enhancing reflection off the NW top surfaces. A diameter/pitch ratio of between $1/3 - 2/3$ was found to be optimal [1.42].
- **Fabry-Perot mode resonances** occur within the NW along its length. These resonances have minimal effect on NWs of length greater than 500 nm, and are not as significant on NW absorption as the two other mentioned phenomena [1.42, 1.43].

The radial mode resonances arise due to the behavior of the incident electric field in the cylindrically symmetric NW structure [1.51]. Incident light couples more effectively with the hybrid HE_{1n} family of modes due to the electric field profile within the NW overlapping with that of an incident plane wave. Through Maxwell's equations in cylindrical coordinates, the solution for the transverse component of the electric field in a cylindrical NW is given by,

$$E(\rho) = A_m J_m(\rho T) + B_m N_m(\rho T) \quad (1.23)$$

where A_m and B_m are constants that are determined through boundary conditions, T is a constant relating to the wavenumber in the NW, J_m is the Bessel function, and N_m is the

Neumann function. Since the Neumann function is not defined at $\rho = 0$ it must be the case that $B_m = 0$. If we focus our attention to the radius $\rho = R$ (the radius of the NW) with no field outside the NW,

$$E(R) = J_m(RT) = 0 \quad (1.24)$$

If we approximate the Bessel function as a sine wave, we require that $RT = n\pi$ for Eq. (1.24) to hold true. This results in,

$$\lambda_{HE_{1n}} = \frac{\text{Re}\{\bar{n}\}D}{n} \quad (1.25)$$

where \bar{n} is the complex index of refraction of the mode, and D is the diameter of the NW. There is a clear NW diameter dependence on the resonant absorption wavelength coupling with the HE_{1n} mode of the NW. This resonant coupling produces a sharp absorption peak at the coupling wavelength with absorption higher than that of a thin film made of the same material. With increasing NW diameter, there will be a red-shift of the sharp resonant absorption peak, allowing for absorption wavelength tuning through manipulation of NW geometry as opposed to bandgap engineering. Higher order HE_{1n} modes for $n > 1$ will cause additional resonant absorption peaks; however, these peaks do not produce as strong of an absorption effect as the HE_{11} guided modes. Coupling of incident light into the HE_{1n} modes allows for optical absorption over an area larger than the NW surface area.

1.4 Thesis Goal and Outline

The focus of this work is on narrow bandgap III-V materials and their application in the MWIR and LWIR regions. InSb and InAsSb alloy thin films were grown by MBE

on Si and fabricated through a top-down etching method into large diameter NWs (called pillars) to demonstrate the ability for MWIR and LWIR multispectral absorption with diameter dependent absorption. Chapter 2 focuses on the primary experimental and characterization techniques used for this work. MBE and reactive ion etching (RIE) are discussed as they are key to the fabrication of large diameter pillars, with thin film quality characterization through SEM, EDS, Hall effect measurements, and XRD, and pillar characterization through SEM and FTIR. Chapter 3 discusses results pertaining to initial InSb pillars acting in the SWIR and MWIR regions, and chapter 4 discusses InAsSb pillars to allow for absorption into the LWIR region. Chapter 5 discusses work on InSb p-i-n structure thin film devices for photoconductor and photovoltaic operation. Chapter 6 discusses etching of single pillar structures, and chapter 7 concludes, summarizing the key findings of this work, and potential prospects moving forwards beyond these results.

1.5 References

- [1.1] W. Herschel, Experiments on the refrangibility of the invisible rays of the Sun, *Phil. Trans. R. Soc.* 90 (1800) 284-292
- [1.2] E. S. Barr, Historical survey of the early development of the infrared spectral region, *Am. J. Phys.* 28 (1960) 42-54
- [1.3] A. Ghukasyan, and R. R. LaPierre, Modelling thermoelectric transport in III-V nanowires using a Boltzmann transport approach: a review, *Nanotechnol.* 32 (2021) 042001
- [1.4] T. J. Seebeck, On the unequal evolution of heat in the prismatic spectrum, *Phil. Mag.* 66 (1825) 330-343
- [1.5] L. Nobili, Beschreibung eines Thermo-Multiplicators oder elektrischen Thermoskops, *Ann. Physik* 2 (1830) 245

- [1.6] L. Nobili, and M. Melloni, Recherches sur plusieurs phénomènes calorifiques entreprises au moyen du thermo-multiplicateur, *Ann. Chim. et Phys.* 48 (1831) 198-218
- [1.7] A. Rogalski, J. Antoszewski, and L. Faraone, Third-generation infrared photodetector arrays, *J. Appl. Phys.* 105 (2009) 091101
- [1.8] S. Langley, The bolometer and radiant energy, *Proceedings of the American Academy of Arts and Sciences* 16 (1880) 342-358
- [1.9] A. Rogalski, Infrared detectors: an overview, *Infrared Phys. Technol.* 43 (2002) 187-210
- [1.10] T. Case, Notes on the change of resistance of certain substances in light, *Phys. Rev.* 9 (1917) 305
- [1.11] R. J. Cashman, Film-type infrared photoconductors, *Proc. IRE* 47 (1959) 1471
- [1.12] S. M. Sze, *Physics of semiconductor devices*, Wiley, 1981
- [1.13] N. Ashcroft and N. Mermin, *Solid state physics*, Brooks/Cole, 1976
- [1.14] R. Hummel, *Electronic properties of materials*, 4th ed., Springer, 2011
- [1.15] A. Kitai, *Principles of solar cells, LEDs and related devices – The role of the PN junction*, 2nd ed., Wiley, 2019
- [1.16] O. Madelung, *Physics of III-V compounds*, Wiley, New York, 1964
- [1.17] R. K. Willardson and A. C. Beer, Eds., *Semiconductors and semimetals*, Vol. 2, *Physics of III-V compounds*, Academic, New York, 1966
- [1.18] K. Dick, P. Caroff, J. Bolinsson, M. Messing, J. Johansson, K. Deppert, L. Wallenberg, and L. Samuelson, Control of III-V nanowire crystal structure by growth parameter tuning, *Semicon. Sci. and Technol.* 25 (2010) 024009
- [1.19] M. Chelikowsky and M. Cohen, Nonlocal pseudopotential calculation for the electronic structure of eleven diamond and zinc-blende semiconductors, *Phys. Rev.* 14 (1976) 556-582
- [1.20] I. Vurgaftman, J. Meyer, and L. Ram-Mohan, Band parameters for III-V compound semiconductors and their alloys, *J. Appl. Phys.* 89 (2001) 5815
- [1.21] B. Streetman and S. Banerjee, *Solid state electronic devices*, 5th ed., New Jersey: Prentice Hall, 2000

- [1.22] Y. Varshni, Temperature dependence of the energy gap in semiconductors, *Physica* 34 (1967) 149-154
- [1.23] W. Lawson, S. Nielsen, E. Putley, and A. Young, Preparation of properties of HgTe and mixed crystals of HgTe-CdTe, *J. Phys. Chem. Solids* 9 (1959) 325-329
- [1.24] A. Rogalski, HgCdTe infrared detector material: history, status and outlook, *Rep. Prog. Phys.* 68 (2005) 2276
- [1.25] G. Hansen, and J. Schmidt, Energy gap versus alloy composition and temperature in $\text{Hg}_{1-x}\text{Cd}_x\text{Te}$, *J. Appl. Phys.* 53 (1982) 7099
- [1.26] W. Higgins, G. Seiler, R. Roy, and R. Lancaster, Standard relationships in the properties of $\text{Hg}_{1-x}\text{Cd}_x\text{Te}$, *J. Vac. Sci. Technol.* 7 (1989) 271
- [1.27] J. Peterson, J. Franklin, M. Reddy, S. Johnson, E. Smith, W. Radford, and I. Kasai, High quality large-area MBE HgCdTe/Si, *J. Electron. Mat.* 35 (2006) 1283-1286
- [1.28] A. Rogalski, K. Adamiec, and J. Rutkowski, *Narrow-gap semiconductor photodiodes*, SPIE Press, Bellingham, 2000
- [1.29] L. Kozlowski, K. Vural, J. Arias, W. Tennant, and R. DeWames, Performance of HgCdTe, InGaAs and quantum well GaAs/AlGaAs staring infrared focal plane arrays, *Proc. SPIE* 3182 (1997) 2-13
- [1.30] W.F.M. Micklethwaite, and A. Johnson, *InSb: materials and devices*, Kluwer Academic Publishers, Boston, 2000, 177-204
- [1.31] J. T. Wimmers, and D. S. Smith, Characteristics of InSb photovoltaic detectors at 77 K and below, *Proc. SPIE* 364 (1983) 123-131
- [1.32] J. T. Wimmers, R. M. Davis, C. A. Niblack, and D. S. Smith, Indium antimonide detector technology at Cincinnati Electronics Corporation, *Proc. SPIE* 930 (1988) 125-138
- [1.33] A. M. Fowler, I. Gatley, P. McIntyre, F. J. Vrba, and A. Hoffman, ALADDIN: the 1024x1024 InSb array - design, description, and results, *Proc. SPIE* 2816 (1996) 150-160
- [1.34] S. Gunapala, S. Bandara, J. Liu, C. Hill, S. Rafol, J. Mumolo, J. Trinh, M. Tidrow, and P. LeVan, 1024x1024 pixel mid-wavelength and long-wavelength infrared QWIP focal plane arrays for imaging applications, *Semicond. Sci. Technol.* 20 (2005) 473-480

- [1.35] M. Jhabvala, K. Choi, C. Monroy, and A. La, Development of 1Kx1K, 8-12 μm QWIP array, *Infrared Phys. Technol.* 50 (2007) 234-239
- [1.36] S. Gunapala, and S. Bandara, *Handbook of thin devices*, Academic, San Diego, 2000, Vol. 2
- [1.37] R. R. LaPierre, M. Robson, K. M. Azizur-Rahman, and P. Kuyanov, A review of III-V nanowire infrared photodetectors and sensors, *J. Phys. D: Appl. Phys.* 50 (2017) 123001
- [1.38] C. Haapamaki, J. Baugh, and R R. LaPierre, Critical shell thickness for InAs-Al_xIn_{1-x}As(P) core-shell nanowires, *J. Appl. Phys.* 112 (2012) 124305
- [1.39] G.E. Cirlin, V. Dubrovskii, I. Soshnikov, N. Sibirev, Y. Samsonenko, A. Bouravleuv, J. Harmand, and F. Glas, Critical diameters and temperature domains for MBE growth of III-V nanowires on lattice mismatched substrates, *Phys. Stat. Sol. (RRL)*, 3 (2019) 112-114
- [1.40] F. Glas, Critical dimensions for the plastic relaxation of strained axial heterostructures in free-standing nanowires, *Phys. Rev. B* 74 (2006) 121302
- [1.41] K. Kavanagh, Misfit dislocations in nanowire heterostructures, *Semicond. Sci. Technol.* 25 (2010) 024006
- [1.42] K. M. Azizur-Rahman, and R. R. LaPierre, Wavelength-selective absorptance in GaAs, InP and InAs nanowire arrays, *Nanotechnology* 26 (2015) 295202
- [1.43] K. M. Azizur-Rahman, and R. R. LaPierre, Optical design of a mid-wavelength infrared InSb photodetector, *Nanotechnology* 27 (2016) 315202
- [1.44] M. Robson, K. M. Azizur-Rahman, D. Parent, P. Wojdylo, D. Thompson, and R. R. LaPierre, Multispectral absorptance from large-diameter InAsSb nanowire arrays in a single epitaxial growth on silicon, *Nano Futures* 1 (2017) 035001
- [1.45] W. Wei, X. Bao, C. Soci, Y. Ding, Z. Wang, and D. Wang, Direct heteroepitaxy of vertical InAs nanowires on Si substrates for broad band photovoltaics and photodetection, *Nano Lett.* 9 (2009) 2926-2934
- [1.46] H. Shin, S. Lee, D. Kim, M. Bae, J. Heo, K. Choi, W. Choi, J. Choe, and J. Shin, Short-wavelength infrared photodetector on Si employing strain-induced growth of very tall InAs nanowire arrays, *Sci. Rep.* 5 (2015) 10764

- [1.47] H. Pettersson, I. Zubritskaya, N. Nghia, J. Wallentin, M. Borgstrom, K. Storm, L. Landin, P. Wickert, F. Capasso, and L. Samuelson, Electrical and optical properties of InP nanowire ensemble p+-i-n+ photodetectors, *Nanotechnology* 23 (2012) 135201
- [1.48] S. Zhao, H. Nguyen, and Z. Mi, Near-infrared InN nanowire optoelectronic devices on Si, *Proc. 2014 IEEE Photonics Society Summer Topical Meeting Series* (2014) 208-209
- [1.49] J. Svensson, N. Anttu, N. Vainorius B. Mattias Borg, and L. Wernersson, Diameter dependent photocurrent in InAsSb nanowire infrared photodetectors, *Nano. Lett.* 13 (2013) 1380-1385
- [1.50] M. Thompson, A. Alhodaib, A. Craig, A. Robson, A. Aziz, A. Krier, J. Svensson, L. Wernersson, A. Sanchez, and A. Marshall, Low leakage-current InAsSb nanowire photodetectors on silicon, *Nano Lett.* 16 (2016) 182-187
- [1.51] K. Azizur-Rahman, *Simulation of III-V nanowires for infrared photodetection*, McMaster University, 2016

Chapter 2 – Experimental Methods and Characterization Techniques

2.1 Characterization Methods

2.1.1 *Scanning Electron Microscopy*

Due to the diffraction of light for some given wavelength, eventually a scale can be reached where two small structures or features in the object cannot be resolved in the image with a visible light microscope. Resolution can be described by Abbe's equation as follows:

$$d = \frac{0.612\lambda}{NA} \quad (2.1)$$

where λ is the wavelength of light being used for imaging, d is the distance between features, and NA is the numerical aperture of the focusing lens [2.1]. For visible light and using an ideal NA of 1, the minimum resolvable distance is roughly 250-300 nm, about half of the wavelength of light at the shorter end of the visible spectrum. Thus, for taking high resolution images of nano- and micro-scale structures, an alternative method is required. Scanning electron microscopy (SEM) allows us to surpass this diffraction-limited resolution of visible light by utilizing a beam of electrons rather than a beam of light for sample imaging. An electron beam is generated and "lenses" utilizing electromagnetic fields focus the beam onto a region of the sample. A key parameter in SEM is the accelerating voltage, determining the momentum of the incident electrons on the sample. A lower accelerating voltage (1-5 kV) will prevent electrons from penetrating the sample as deeply, resulting in imaging of the sample surface. A higher accelerating voltage (5-15

kV) is used for energy dispersive x-ray spectroscopy (EDS) to generate characteristic x-rays for composition analysis. Figure 2.1 schematically depicts a volume of a sample with an incident electron beam.

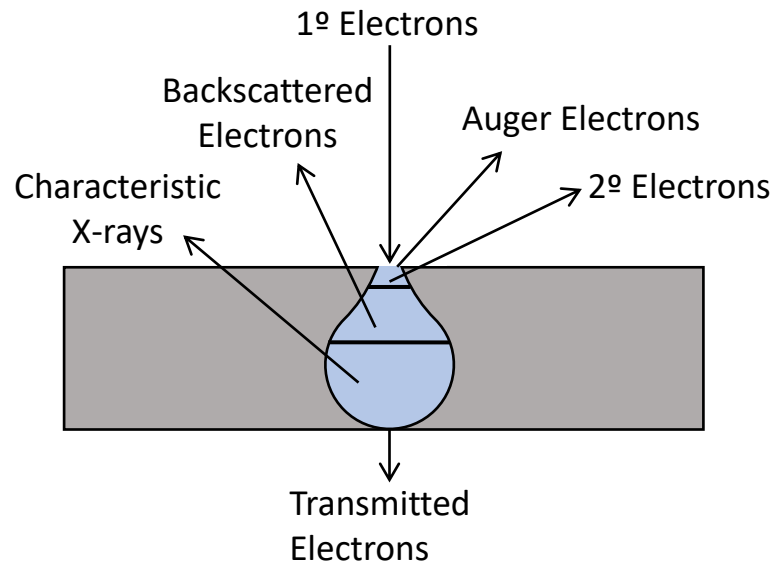


Figure 2.1 Schematic depicting the interaction volume that a beam of incident electrons creates with a sample under investigation, and the relative positions of detectable emissions used for imaging.

The incident electron beam consists of primary (1°) electrons. The incident electron beam can remove core electrons of the atoms making up the sample near the surface. An electron from a higher energy level can fill the newly made vacancy, emitting energy in the process. This energy can remove an additional electron from a higher energy level, called an Auger electron. Auger electrons are produced in the first 10 's of Angstroms in the electron interaction volume with the sample. Typically, SEM images are produced as a result of secondary (2°) electrons. These are generated in the first 10 's of nanometers of the interaction volume, and are the result of low energy loosely bound electrons in the sample

being ionized directly and collected by the detector. Since these are low energy electrons, 2° electrons are easily collected by a detector with an applied bias across the detector. Backscattered electrons occur deeper in the sample and are the result of the 1° electrons scattering off atomic nuclei. Since this interaction is dependent on the nuclei size, backscattered electrons can depict strong contrast if two materials of largely differing atomic number are present. The generation of characteristic X-rays occurs when an inner shell electron is removed by the 1° electron beam and the vacancy is filled by an electron from a higher-level shell. Different to Auger electrons, however, the energy is emitted as an X-ray emission characteristic to that atomic species, as opposed to the energy going towards the ejection of an additional electron. These X-rays can be collected and can yield material composition information, and are the basis of using an SEM system to perform EDS analysis. 2° electrons from sample surface imaging and characteristic X-ray generation for EDS are the key processes used in this thesis for sample analysis.

The JEOL 7000 and FEI Magellan 400 SEM systems were used extensively for this thesis. The JEOL 7000 SEM was used for early InSb growths to observe thin film uniformity, as well as to image finished InSb pillars, and the intermediate top-down fabrication steps. The accelerating voltage used was typically 5 kV, with a working distance of about 15 mm. The images were taken to confirm fabrication success of initial thin film growths under varying substrate temperature conditions, and the presence of nanoscale structures after reactive ion etching (RIE) and during the intermediate step of Ti mask creation. The Magellan was used later due to its higher resolution, with sub-nanometer resolution being available. This allowed for higher resolution imaging of surface textures

on the completed samples providing insights on surface damage due to etching, and higher resolution images of single nanowires/pillars. To allow for these higher resolution images, a comparable accelerating voltage of about 5 kV was typically used, but with a much smaller working distance of 2-3 mm. Both the JEOL 7000 and the Magellan have EDS capabilities; however, the Magellan was the primary microscope used for EDS measurements. This was done to determine the composition of grown InAsSb thin films to determine the bandgap of the alloy grown. A background measurement using copper on the sample holder was done to ensure adequate signal was being collected. An accelerating voltage was chosen that is sufficient to excite inner shell atoms such that characteristic X-rays are emitted; for the case of InAsSb this is around 15 kV to obtain the 10.53 keV emission from the $K\alpha$ line of As. This accelerating voltage is also sufficient to obtain emissions from the $L\alpha$ lines of In and Sb at 3.286 keV and 3.604 keV, respectively. Analysis of the characteristic X-rays yields detailed compositional analysis of the imaged region allowing for bandgap determination once the composition of InAsSb was obtained. EDS was also performed on a focused ion beam (FIB) etched InAsSb sample to observe if Ga ions used in the etch were deposited into the surface of the sample.

2.1.2 X-ray Diffraction

X-ray diffraction (XRD) was performed to better understand InSb and InAsSb thin film growth quality prior to processing into the desired nanostructures. XRD allows for obtaining crystal lattice information from the diffraction of incident X-rays due to interactions with the atomic planes of a compound [2.2]. X-ray wavelengths used in XRD experiments are in the region of 1 Å, comparable to the spacings between atoms in a crystal

lattice, allowing for incident X-rays to be scattered off the atomic planes. The path of scattered X-rays is dependent on the atomic species involved in the lattice, as well as the atomic arrangement of the solid, allowing for a uniquely determined diffraction pattern. The simplest way to understand X-ray diffraction by a crystalline solid is with Bragg's law:

$$n\lambda = 2d \sin \theta \quad (2.2)$$

where d is the spacing between a family $\langle ikl \rangle$ of atomic planes, θ is the angle of incidence of incoming X-rays, and λ is the X-ray wavelength.

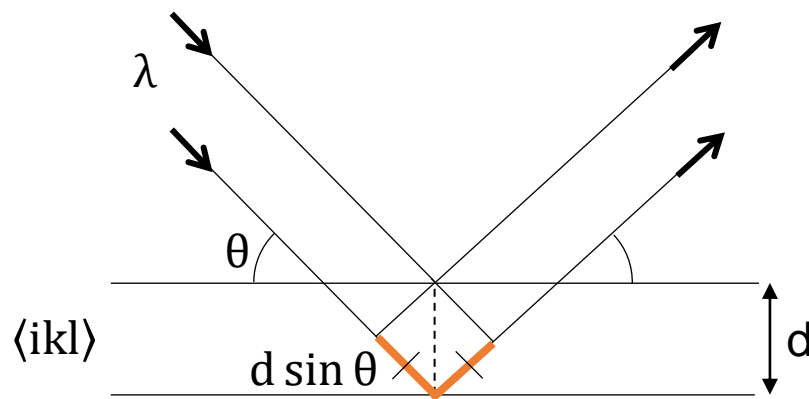


Figure 2.2 Depiction of Bragg's law, outlining the condition for constructive interference between incident X-rays reflecting off atomic planes.

The crystal lattice of a given material will take on an arrangement with an interatomic spacing d . Atomic plane families are denoted by $\langle ikl \rangle$ and incident X-rays, having a wavelength on the order of the atomic spacing and atomic nuclei sizes, will diffract providing unique information regarding crystal orientation and composition. Figure 2.2 shows an incident X-ray of some wavelength λ scattering off the first and second planes with a difference in path length equivalent to $2d \sin \theta$ (the orange segment). To ensure

constructive interference of the diffracting X-rays, this value must be equal to a multiple of the incident wavelength, leading to the result of equation (2.2).

XRD was performed with a Bruker D8 DISCOVER diffractometer. The X-ray sources used were a Co sealed tube emitting at a wavelength of $\lambda = 1.79026 \text{ \AA}$ operating with a Vantec 500 area detector, and a Rigaku RU200 Cu anode source emitting at a wavelength of $\lambda = 1.54056 \text{ \AA}$ operating with a SMART6000 detector. Phase analysis and texture analysis were performed on InSb and InAsSb thin films. Phase analysis, where the phase in question is a material's composition and crystal structure, is performed to identify unknown materials and yields information on the crystal lattice of a crystalline material. Texture analysis focuses on orientation distributions of polycrystalline samples. Understanding the distribution of crystallites in a polycrystalline sample can allow for the polycrystallinity to be controlled in future studies by observing overall trends of an increasing composition of a desired orientation.

2.1.3 Fourier-transform Infrared Spectroscopy

Fourier-transform IR spectroscopy (FTIR) was an invaluable tool for analysis of IR absorption. FTIR was primarily used on InSb and InAsSb thin films and pillar arrays to compare their absorptance and to observe the enhanced resonant absorption peaks caused by the pillar geometry in the MWIR and LWIR regions. FTIR was also performed on substrates to ensure IR transparency. FTIR operation begins with the formation of an interferogram from an IR source, allowing for high resolution wavelength scanning without the use of a diffraction grating [2.3, 2.4]. The IR light is split into two beams each taking

its own path, one path towards a stationary mirror and the other path towards a mirror that is allowed to move, allowing for altering the total path distance d travelled by the IR light in that path. The phase difference ϕ introduced for light of some wavelength λ entering the interferometer will be given by,

$$\phi = \frac{2\pi}{\lambda} d \quad (2.3)$$

It can be seen that the phase difference changes depending on the mirrors motion affecting the path difference d , and is dependent on the wavelength of light. When the path difference is an integer multiple of λ the beams meeting back up at the beam-splitting mirror will overlap such that they constructively interfere. If d is a half integer multiple of λ , they will destructively interfere. Since this is dependent on λ itself, this introduces the ability to discern spectral information from the broad IR source without a diffraction grating. Each wavelength of light in the broad source will undergo this constructive and destructive interference process, and each wavelength will overlap once completing the paths in the interferometer arms yielding the interferogram. This modulated IR light is then free to proceed towards the sample for reflectance (R) and transmittance (T) measurements. Losses in the incident IR light will occur from the sample of interest, and this will affect the interferogram. The interferogram, being a collection of overlapping wavelengths interfering, can be decomposed into its individual components through a Fourier transform, yielding information regarding the reflectance and transmittance of the incident light in terms of individual wavelengths. The final data is typically displayed in terms of wavenumber with units cm^{-1} . The absorptance (A) of the material can then be found by

$$A = 1 - R - T \quad (2.4)$$

The Bruker Vertex 70/80v FTIR system was used for this thesis. The system has a sample compartment for bulk sample use; however, in order to focus on specific sample regions of interest, the system was used in conjunction with the Hyperion 3000 microscope. The interferogram is produced in the Vertex unit from an IR source, and then is taken to the microscope through a series of mirrors. The microscope can operate in reflectance or transmittance modes, and scans from 8000-600 cm^{-1} , corresponding to roughly 1.25-17 μm . Once the IR light enters the Hyperion it can be reflected through a series of mirrors downwards or upwards for transmittance and reflectance measurements, respectively. If reflected downwards for transmittance measurements, it is incident upon the rear of the sample, focused by a condenser. If reflected upwards for reflectance measurements it is incident upon the top of the sample, and is focused by a 15x objective lens. Reflected and transmitted light is collected by the objective lens and is then reflected to a liquid nitrogen cooled MCT detector. A knife edge hard aperture can be used to limit illumination to specific regions on the sample surface. A visible light source is used in conjunction with a live-feed camera to locate the point of interest on the sample, as well as to focus on a gold film on the sample stage for reflectance reference measurements, and through the opening on the sample stage for transmittance measurements. A depiction of the FTIR setup used is presented in figure 2.3.

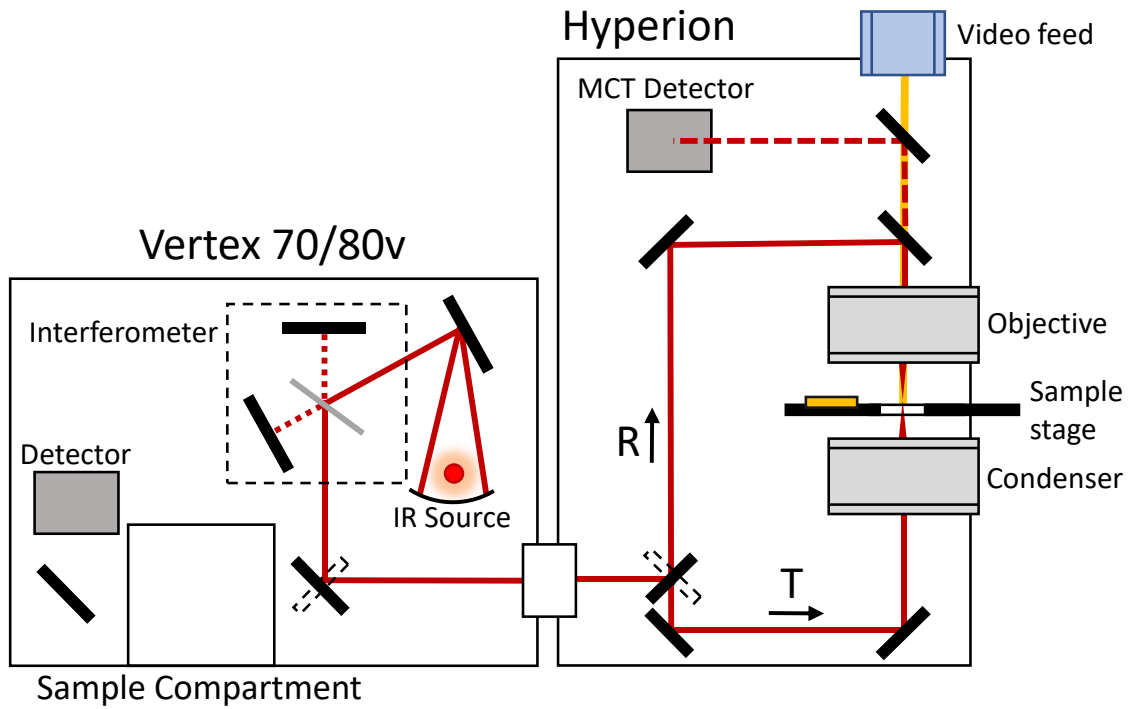


Figure 2.3 Schematic layout of the Vertex 70/80v and Hyperion 3000 microscope setup used for FTIR measurements. Beam paths in the Hyperion are labeled with R and T for reflectance and transmittance, respectively. The interferometer in the Vertex is highlighted. The mirror arrangement is simplified.

2.1.4 The Hall Effect

Hall effect measurements were performed on InAsSb thin films grown on insulating Si (100) substrates to determine doping levels and the type of majority charge carrier to confirm doped MBE growths. During Hall effect measurements, 4 probes are placed on the sample of interest [2.5]. A voltage V is applied across the sample from 2 probes driving the motion of charge carriers in the semiconductor. When a magnetic field is introduced perpendicular to the sample surface, the moving charge carriers will experience a force moving them to one side of the device. The separation of charge carriers by the magnetic field then causes a voltage, called the Hall voltage V_{Hall} , to be induced in a direction transverse to the initial applied voltage and charge carrier flow. This Hall voltage is measured by 2 probes and can yield information regarding carrier concentration and mobility. The insulating Si substrates are used to ensure current flow is through the thin film growth itself and that the Si substrate is not offering an alternative conduction pathway. A schematic demonstrating a Hall effect measurement is shown in figure 2.4.

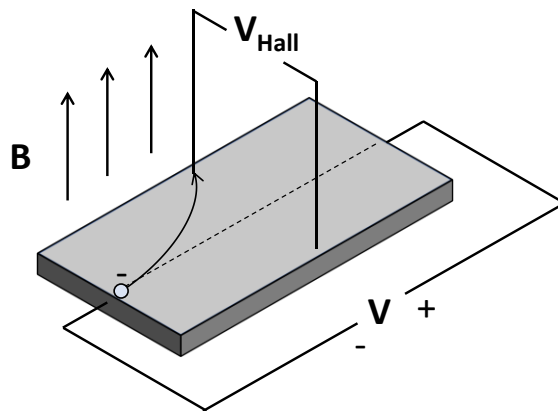


Figure 2.4. Schematic demonstrating probe arrangement for a Hall effect measurement.

2.2 Top-down Pillar Fabrication Method

As mentioned in chapter 1, NWs can be grown by the VLS method using an MBE system. This method of NW growth is diffusion-driven with surface kinetics of adatoms of relevant atomic species forming NW structures epitaxially from the substrate. Since this growth is diffusion-driven, length-wise axial NW growth is competing with radial NW growth, resulting in difficulty in achieving larger diameter NW structures. It can be seen from equation (1.25) that $\lambda_{\text{HE}_{1n}} \propto D$, and thus larger diameter NWs are required for absorption in the IR region. Due to the difficulty of achieving the desired NW diameters by VLS growth, a top-down etching method was used in this thesis for NW fabrication. The length of the NWs (or “pillars”) is determined by the thickness of an initial thin film grown on Si substrates, and the diameter of the pillars is determined by a mask formed by electron beam lithography (EBL) and a Ti deposition. Reactive ion etching (RIE) was then used to etch away unwanted material. This process is depicted in figure 2.5.

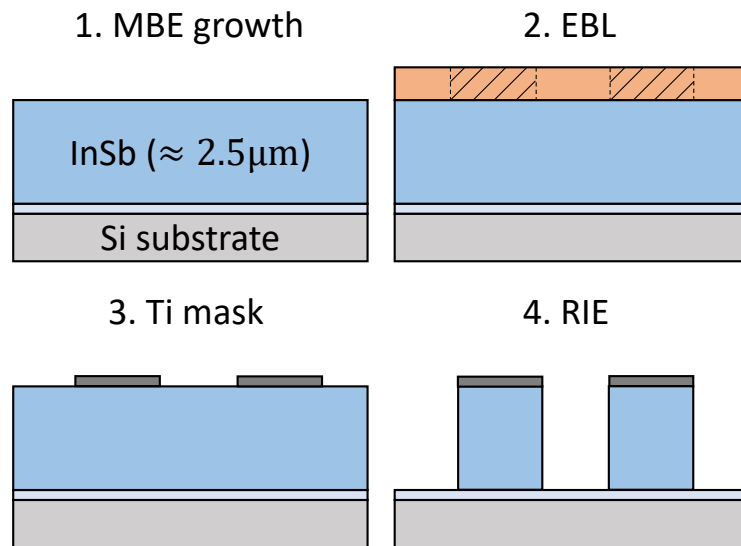


Figure 2.5 Depiction of the top-down fabrication process used to obtain the large diameter pillars.

2.2.1 Molecular Beam Epitaxy

Molecular beam epitaxy (MBE) was first demonstrated in the 1970's and has since become a core method of growing high quality semiconductor materials on a given substrate wafer [2.6, 2.7]. The main growth chamber of an MBE system will have multiple solid sources (effusion cells) and/or gas sources and allow for the required atomic species to impinge on the substrate. The rate of growth of the semiconductor is dictated by the evaporation of the atomic species and can be accurately controlled for alloy growth and doping. MBE is a powerful technique over other crystal growth techniques due to its ultra-high vacuum (UHV) environment ($p < 10^{-9}$ torr) and the beam nature of the atomic species flux. This UHV environment allows for the impinging atomic species to arrive on the substrate surface as individual atomic species called adatoms on the sample surface. The adatoms are then driven by surface kinetics and may bind to the substrate and begin semiconductor growth, or may desorb back into the growth chamber. MBE is typically done at low growth rates of about $1 \mu\text{m/h}$ ($1 \text{ monolayer s}^{-1}$), to ensure that adatoms are given time to migrate on the substrate surface and crystallize to a high degree of quality, with a smooth crystalline growth surface. The fluxes of atomic species are controlled through mechanical shutters that can instantaneously start and end the deposition. The UHV environment of the growth chamber also allows for the unique ability of in situ growth characterization. Techniques such as reflection high-energy electron diffraction (RHEED), Auger electron spectroscopy (AES), ellipsometry, or optical reflection measurements, can be performed in real time during semiconductor growth and yield live feedback on growth quality, and material thickness over time. These real time in situ techniques, in conjunction

with the low general growth rates and highly controlled beam-like flux, allow for the growth of complex layered semiconductor structures with abrupt boundaries and varied doping levels and types.

The beam collimation in MBE is preserved due to the long mean free path that the incident atomic species travel in the UHV conditions of the MBE. Once the impinging molecular species reach the substrate they can adsorb to the surface and begin diffusing as individual adatoms allowing for epitaxial growth. While diffusing, they can incorporate with the substrate's crystal lattice through either physisorption or chemisorption. During physisorption, the attractive forces are van der Waals and there is no electron transfer between the adatoms and the atoms in the substrate lattice. During chemisorption, electron transfer and chemical binding occurs. The energies required for physisorption are lower than those required for chemisorption. In general, for MBE crystal growth, adatom condensation occurs through a two-stage process in which physisorption leads into chemisorption. Three growth modes may occur depending on the strength of the binding forces between the adatoms, other adatoms, and the substrate. The Volmer-Weber growth mode (island growth mode) occurs when the adatoms are more strongly bound to each other rather than the substrate. Adatoms diffusing on the surface will bind to each other and begin to coalesce into islands formed by the impinging atomic species. The islands act as nucleation sites due to their lower surface energies, and diffusing adatoms will continue to bind to the growing islands that eventually meld together and form the thin film growth. The Frank van der Merwe growth mode (layer-by-layer) occurs when the impinging adatoms have a stronger attraction to the substrate than to each other. Adatoms begin to

bind to the substrate and form a thin film layer; however, as the diffusing adatoms are more strongly bound to the substrate, the substrate surface is covered with an initial layer before the next layer begins to form. Since the adatoms are not as strongly attracted to one another they tend to spread out forming thin film layers during growth as opposed to nucleating into islands. The final growth mode, the Stranski-Krastanov growth mode, is a combination of the previous two. After initial monolayers of layer-by-layer growth, island nucleation becomes preferential resulting in island formation on the underlying initial thin film layers. These growth modes are depicted in figure 2.6.

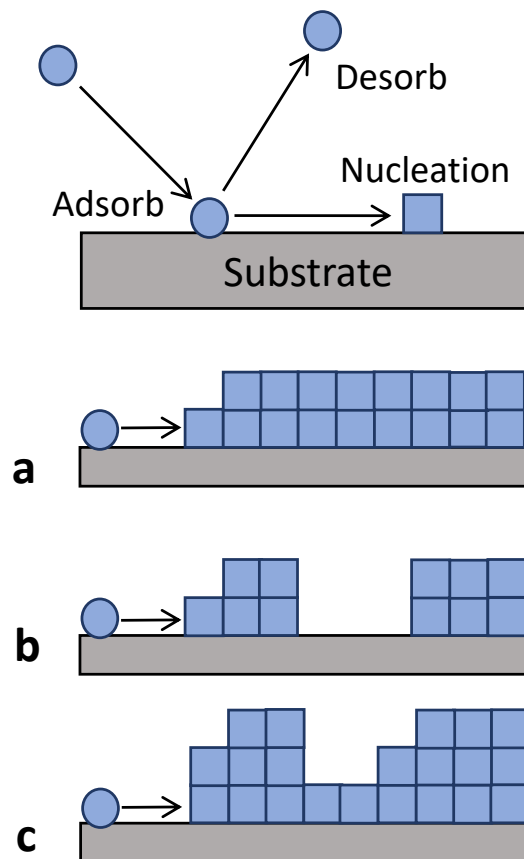


Figure 2.6 Depiction of the various growth modes that diffusing adatoms may undergo to lead to thin film formation. a) Frank van der Merwe (layers), b) Volmer-Weber (islands), and c) Stranski-Krastanov (layer + islands).

In this work, MBE was used to grow InSb and InAsSb thin films. These thin films formed the basis for the top-down etching process used to arrive at large diameter InSb and InAsSb pillars for MWIR and LWIR absorption (step 1, figure 2.4). Initial thin film growths consisted of undoped InSb grown on undoped ($> 100 \Omega \text{ cm}$) Si (100) substrates. This undoped substrate was used in order to perform IR transmission measurements on the completed pillar arrays by ensuring that the substrate would be highly transparent in the IR regime without free carrier absorption. Transparency of the substrate was demonstrated with FTIR measurements prior to MBE growth. Si (100) substrates were 4" in diameter and cleaved into 4 quarters. Prior to loading into the MBE load lock, the silicon substrate was etched for 1 min in buffered HF to remove native oxide. The substrate was then loaded and degassed at 300 °C for 15 min in a preparation chamber before being transferred into the main growth chamber. The initial InSb growths were performed to optimize InSb thin film quality by adjusting substrate temperature during growth (500 °C, 550 °C, 600 °C) and by introducing a thin AlSb buffer layer (~ 10 nm thick, 550 °C substrate temperature). It was immediately made clear from SEM imaging that the presence of the AlSb buffer substantially promoted uniform thin film growth. Due to the large lattice mismatch between InSb and Si, a buffer is necessary to promote thin film growth and relieve mismatch-induced lattice strain and reduce the presence of defects. The specific mechanism by which the AlSb buffer layer on Si promotes thin film growth was studied in chapter 3.

InAsSb thin films were also grown by MBE. These were grown on the same undoped ($> 100 \Omega \text{ cm}$) Si (100) substrates for optical measurements. InAsSb allows for bandgap tuning through material composition and the intent was to grow a thin film with as low a

bandgap energy as possible by introducing As to an InSb growth, and then manipulating absorption wavelengths in the LWIR region by tuning pillar geometry. The composition $\text{InAs}_{0.36}\text{Sb}_{0.64}$ yields the lowest bandgap energy of 0.08 eV, as discussed in chapter 1. Si substrates for InAsSb growths were prepared for MBE in the same way as for InSb growths. An AlSb buffer layer was also used for InAsSb. Preliminary growths were performed to observe the effect of temperature on growth quality with SEM and XRD performed, as with the InSb growths. This work is explained in chapter 4.

2.2.2 Electron Beam Lithography and Ti Mask

Electron beam lithography (EBL) was performed with a Vistec EBPG 5000+ system at the University of Toronto's nanofabrication center (TNFC). EBL operates on the same principle as SEM; what SEM is to light microscopy, EBL is to photolithography. In EBL, the electron beam interacts with a resist polymer spun onto the surface of a sample, altering the chemical composition, and allowing for easy removal with a developing solvent. The Vistec system is typically operated at 100 kV, with higher accelerating voltages used for EBL to minimize exposure of resist outside of the pattern area. With standard photolithography, either with a mask or using a direct write system, the resolution of exposure of the resist is limited by the diffraction of light. EBL allows for much finer features to be obtained as with SEM. The Vistec system allows for sub-10 nanometer resolution allowing for accurate patterning of small diameter circles to fabricate the Ti mask for pillar etching. The photoresist used was PMMA A5 and the sample was prepared for EBL at the TNFC. The pattern used for mask fabrication consisted of arrays of circles of varying diameter and pitch combinations. The circle arrays were arranged into a larger grid

consisting of diameter variation when moving along a row, and pitch variation moving down a column, as shown in figure 2.7.

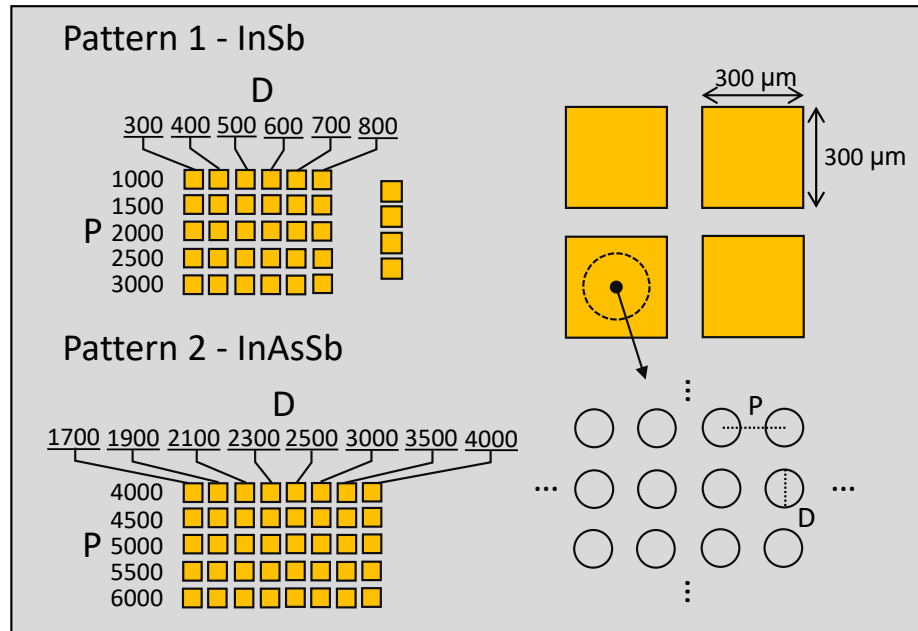


Figure 2.7 Layout of the EBL pattern used for mask fabrication on InSb and InAsSb thin films. Pitches were varied moving down columns, and diameters were varied moving along rows.

The InSb thin film sample used diameters ranging from 300 nm to 800 nm in 100 nm steps, and pitches (spacing between pillars) ranging from 1000 nm to 3000 nm in 500 nm steps. This pattern had an additional column consisting of diameter and pitch combinations (D, P) of (900 nm, 3000 nm), (1100 nm, 3000 nm), (1300 nm, 3500 nm), and (1500 nm, 4000nm). The InAsSb thin film sample used diameters ranging from 1700 nm to 2500 nm in 200 nm steps, and then increasing to 4000 nm in 500 nm steps, and pitches ranging from 4000 nm to 6000 nm in 500 nm steps. The size of each (D, P) combination array is $300 \times 300 \mu\text{m}^2$. The arrangement of the patterns is depicted in figure 2.7. After EBL, development of the PMMA A5 resist was confirmed by SEM imaging. After EBL patterning, electron beam

physical vapor deposition (EBPVD) was used to deposit 120 nm of Ti onto the developed pattern at a rate of roughly 2 \AA/s . Sonication in acetone was used for liftoff to remove the resist leaving behind the arrays of Ti discs to serve as the mask for RIE. Liftoff was confirmed through SEM.

2.2.3 Reactive Ion Etching

With the Ti mask formed by EBL and EBPVD, RIE was used to etch away the thin film leaving the desired pillar structures behind. RIE is a dry etching technique based on plasma generation of desired atomic species that will react with the sample [2.8]. Gasses are introduced into an etching chamber and an electric field is produced between two electrodes (one being the sample stage), typically with a radio frequency (RF) power of 13.56 MHz. The RF power will ionize atoms, removing and accelerating electrons into other atoms, leading to further ionization in a cascading avalanche fashion. This process results in the plasma formation, consisting of electrons, ions, and neutral radicals. Electrons generated in the plasma are attracted to and pushed away from the bottom electrode, where the sample stage is located, by a bias generated in conjunction with the RF power. When the bias is negative, electrons are repelled from the stage and in general electrons do not exist in a region above the sample stage electrode. This region is called the ion sheath and is mainly populated by ions that continuously travel as they are too massive to be affected by the RF power. Etching in the RIE system is primarily done through interactions with these ions and radicals. When the reactive ions or radicals reach the sample, they react creating an etch byproduct, which then desorbs and is pumped out of the etch chamber. RIE was performed at the University of Waterloo's Quantum Nanofabrication Center (QNFC).

The system was an Oxford Instruments ICP380 inductively coupled plasma RIE (ICP-RIE) system. ICP-RIE differs from standard RIE by the introduction of an induction coil which controls ion travel towards the substrate, offering an additional parameter to control the etching process by decoupling plasma generation and ion acceleration, whereas with standard RIE the ion acceleration is controlled by the bias formed on the sample stage electrode coupled to the main RF power that generates the plasma. A depiction of an ICP-RIE etch chamber is presented in figure 2.8.

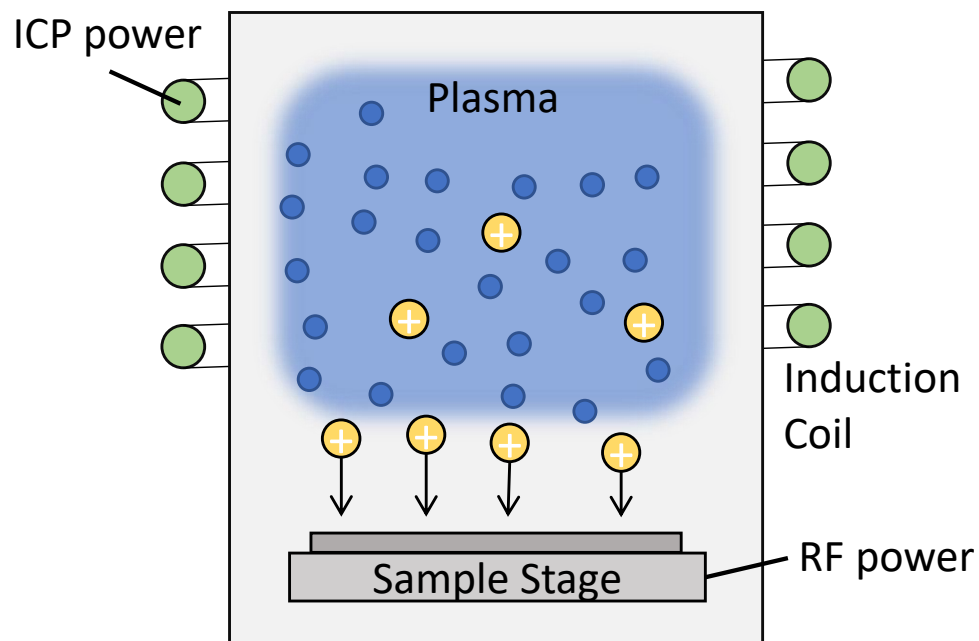


Figure 2.8 Schematic of an ICP-RIE etch chamber depicting the sample stage electrode for RF power, the generated plasma, positive ions in the ion sheath above the sample, and the induction coils around the chamber to direct ion motion.

For both InSb and InAsSb etches, a gas mixture of $\text{CH}_4/\text{H}_2/\text{Ar}$ was used at gas flow rates into the etch chamber of 15/50/5 sccm [2.9]. When CH_4 and H_2 is introduced to the etch chamber, methyl and H radicals are expected to be formed in the plasma. The methyl

radicals react with the In, and the H ions react with Sb to form the hydride SbH_3 . An increase in etch rate is observed as the ratio of CH_4 to H_2 increases; however, the effect of the gas ratio on sidewall morphology is not known, and the ratio is typically kept at less than 1/3 to avoid the deposition of carbon on the material surface. Ar acts to promote a smooth etch surface by incident Ar ions accelerating the desorption process of etch byproducts. At Ar partial pressures greater than 0.1 Pa, however, Ar ions may damage the sample surface.

2.2.4 Focused Ion Beam Etching

In addition to using RIE for top-down fabrication of pillar arrays, focused ion beam (FIB) etching of InAsSb thin films on undoped Si substrates was also performed to create pillar structures. Due to the unique optical properties of NWs outlined in section 1.3.3, the enhancement of optical absorption through coupling into HE_{1n} guided modes leads to enhanced optical absorption over an area larger than the NW cross-sectional area. InP single NWs demonstrated an absorption cross-section that is 50 times greater than the NW cross-sectional area [2.10]. Studies regarding GaAs single NW structures with a diameter of 126 nm demonstrated optical absorption over an area with a diameter of nearly a magnitude higher than that of the NW itself at the peak absorption wavelength [2.11]. At wavelengths that coupled minimally into the NW (away from the HE_{1n} resonance peaks), the diameter of the absorption area was still nearly 5 times the diameter of the NW. This ability of NW structures to enhance absorption in a larger area around them, and not only at the immediate NW surface, has led to the demonstration of high efficiency single NW

devices [2.12]. In the present thesis, optical absorption was measured by FTIR from single pillars and 2x2 pillar arrays produced by FIB etching.

FIB etching was performed with a FEI Versa 3D Dual beam system. The system allows for 5-7 nm resolution on ion beam etching at an accelerating voltage of 30 kV. FIB etch systems operate on similar principles to an SEM system but with an ion beam rather than an electron beam [2.13-2.16]. Ga ions are generated from a liquid metal ion source and a tungsten needle. Ga has a low melting temperature allowing for generation of Ga ions without affecting the tungsten needle. Ions are generated from field emission from the needle tip and directed to the sample. The ions can be reflected, secondary electrons can be generated and collected, x-rays can be generated, and sample atoms can be removed from the surface through sputtering. Because of this, imaging of the sample can be performed through secondary electron collection and etching of the sample can be performed by sputtering material from the surface. The process typically results in ion implantation in the sample surface.

2.3 References

- [2.1] W. Zhou, R. Apkarian, Z. Wang, and D. Joy, Scanning microscopy for nanotechnology, Springer, New York, 2006
- [2.2] B. He, Two-dimensional X-ray diffraction, 2nd ed., John Wiley & Sons, Inc., 2018
- [2.3] M. Vitha, Spectroscopy: principles and instrumentation, John Wiley & Son, Inc., 2018
- [2.4] M. Sardela, Practical materials characterization, Springer, 2014
- [2.5] O. Lindberg, Hall effect, Proc. IRE 40 (1952) 1414-1419
- [2.6] M. Herman, and H. Sitter, Molecular beam epitaxy: fundamentals and current status, Springer Series in Materials Science, 1996

- [2.7] E.H.C. Parker, *The technology and physics of molecular beam epitaxy*, Springer, New York, 1985
- [2.8] K. Nojiri, *Dry etching technology for semiconductors*, Springer, 2015
- [2.9] G. D. Zhang, W. G. Sun, S. L. Xu, H. Y. Zhao, H. Y. Su, and H. Z. Wang, Inductively coupled plasma-reactive ion etching of InSb using CH₄/H₂/Ar plasma, *J. Vac. Sci. Technol., A* 27 (2009) 681
- [2.10] N. Anttu, Absorption of light in a single vertical nanowire and a nanowire array, *Nanotechnology* 30 (2019) 104004
- [2.11] R. Frederiksen, G. Tutuncuoglu, F. Matteini, K. Martinez, A. Fontcuberta i Morral, and E. Alarcon-Llado, Visual understanding of light absorption and waveguiding in standing nanowires with 3D fluorescence confocal microscopy, *ACS Photonics* (2017) 2235-2241
- [2.12] P. Krogstrup, H. Jørgensen, M. Heiss, O. Demichel, J. Holm, M. Aagesen, J. Nygard, and A. Fontcuberta i Morral, Single-nanowire solar cells beyond the Shockley-Queisser limit, *Nat. Photonics* 7 (2013) 306-310
- [2.13] S. Reyntjens, and R. Puers, A review of focused ion beam applications in microsystem technology, *J. Micromech. Microeng.* 11 (2001) 287
- [2.14] S. Matsui, and Y. Ochiai, Focused ion beam applications to solid state devices, *Nanotechnology* 7 (1996) 247
- [2.15] J. Gierak, Focused ion beam technology and ultimate applications, *Semicond. Sci. Technol.* 24 (2009) 043001
- [2.16] C. Volkert, and A. Minor, Focused ion beam microscopy and micromachining, *MRS Bulletin* 32 (2007) 389-399

Chapter 3 – InSb Nanowires for Multispectral Infrared Detection

The results presented in this chapter are a part of the publication,

C. Goosney, V. Jarvis, D. Wilson, N. Goktas, and R. LaPierre, InSb nanowires for multispectral infrared detection, *Semicond. Sci. Technol.* 34 (2019) 035023

This work discusses InSb pillar fabrication for MWIR detection. Discussion is included in chapter 3.4 not in the original publication providing additional FTIR measurements and SEM images of InSb pillars.

3.1 Abstract

InSb nanowire arrays fabricated by a top-down etching process were investigated for multispectral infrared photodetection. A 2.5 μm thick film of InSb was grown on Si (100) by molecular beam epitaxy using an AlSb buffer layer to alleviate defects associated with lattice mismatch strain, as confirmed by scanning electron microscopy and x-ray diffraction. Using a Ti mask patterned by electron beam lithography, InSb nanowire arrays with diameters ranging from 300 nm to 1300 nm (100 nm steps) and pitches ranging from 1000 nm to 3500 (500 nm steps) were reactive ion etched from the thin film. For each 100 nm increase in nanowire diameter, the peak absorptance wavelength, as measured by Fourier transform infrared spectroscopy, increased by $0.53 \pm 0.2 \mu\text{m}$. The ability for InSb nanowires to produce highly tunable absorptance from 1.61 μm to 6.86 μm was demonstrated.

3.2 Introduction

Currently, the most widely utilized material for infrared (IR) photodetection is $\text{Hg}_{1-x}\text{Cd}_x\text{Te}$ (MCT) due to the ability to tune the direct bandgap from short wavelength IR to very long wavelength IR [3.1-3.4]. MCT, however, suffers from material instabilities due to weak Hg-Te bonds in the crystal structure [3.1]. The substrate used for MCT devices, CdZnTe, while being lattice matched with MCT, is expensive and difficult to integrate with silicon readout integrated circuits [3.3]. Attempts to use much more cost-efficient Si substrates as an alternative to CdZnTe resulted in poor MCT film quality [3.4]. To address these challenges, alternative photodetection technologies are being investigated, including nanowire (NW) arrays of various semiconductor materials [3.5].

A recent finite element analysis study of InSb NW arrays showed tunable optical absorption from 1.5 μm to 6.5 μm by altering the NW diameter [3.6]. NWs support an HE_{11} guided mode resonance that allows incident light to couple strongly with the NWs. As a result, optical absorptance in NWs can exceed that from a thin film of equivalent thickness [3.6-3.9]. Furthermore, this coupling of incident light with the HE_{11} guided mode produces a sharp absorptance peak at a wavelength proportional to the NW diameter, enabling multispectral photodetection in a single material system simply by tuning the NW diameter. Robson et al. [3.10] demonstrated multispectral absorption in large diameter (440 – 520 nm) InAsSb NWs in the short wavelength IR region. The NWs were grown catalyst-free on a Si substrate by selective-area molecular beam epitaxy (MBE). The growth conditions allowed control of the InAsSb NW diameter, leading to the ability to tune the peak

absorptance wavelength of InAsSb without bandgap engineering. In the present article, the first demonstration of multispectral optical absorptance in the short- and mid-IR regions in top-down etched InSb NWs is shown.

3.3 Experimental Details and Results

3.3.1 Thin Film Growth and Characterization

InSb thin films were grown by molecular beam epitaxy (MBE) on Si (100) substrates. The Si substrates had resistivity $>100 \Omega \cdot \text{cm}$ to prevent free carrier absorption in FTIR transmission measurements. The Si substrate underwent a 1 min buffered HF etch to remove any native oxide, followed by degassing at 300 °C for 15 min in a preparation chamber before transfer into the MBE. Antimony was supplied by a valved cracker cell, while aluminum and indium were supplied by a standard effusion cell. An AlSb buffer layer was grown at a substrate temperature of 500 °C, 550 °C and 600 °C for three different growths. A V/III flux ratio of 2, a growth rate of 0.1 $\mu\text{m/h}$, and a growth duration of 6 min resulted in an AlSb buffer layer thickness of 10 nm. Following the AlSb buffer layer, an InSb film was grown at a substrate temperature identical to that of the AlSb buffer. The InSb films were grown with a V/III flux ratio of 1.2 and a growth rate of 0.5 $\mu\text{m/h}$ for 5 h, resulting in a film thickness of 2.5 μm . An additional InSb film was grown at 550 °C with no AlSb buffer to observe the effect of the buffer on the InSb film quality.

A JEOL 7000F scanning electron microscope (SEM) was used to characterize the thin film and NW morphology. The plan view SEM image in figure 3.1(a) shows InSb grown at 550 °C on Si (100) with no AlSb buffer layer. Figure 3.1(b)–(d) show plan view

SEM images of an InSb thin film grown on Si (100) with an AlSb buffer layer. The AlSb buffer growth temperature was 500 °C, 550 °C and 600 °C in figure 3.1(b)-(d), respectively, with the InSb layer grown at the same temperature as AlSb in all cases. With no AlSb buffer layer, the surface morphology in figure 3.1(a) indicates the formation of InSb islands on the Si (100) substrate. Comparing figure 3.1(a) without the AlSb buffer layer and 3.1(c) with the AlSb buffer layer (both at the same growth temperature) indicated that the AlSb buffer layer resulted in smoother InSb films. Similar results were observed in a series of studies performed by Hosseini Vajargah et al. [3.11-3.13] and Woo et al. [3.14] for GaSb epitaxial growth on Si (100). GaSb tends to form in the Volmer-Weber growth mode on Si due to a high surface energy and large lattice mismatch. Due to the long diffusion length of Ga adatoms, Ga also tends to accumulate into droplets on the Si surface. We speculate that a similar process occurs with In during the growth of InSb films. Without an AlSb buffer layer, InSb forms islands along with In droplets on the Si (100) substrate in the Volmer-Weber growth mode. Misfit dislocations, twinning, and anti-phase domains are also expected in the InSb film due to the large lattice mismatch and polar/non-polar nature of InSb on Si. Previous studies have shown that the AlSb buffer layer also forms islands on the Si surface, but at an increased island density due to the low surface diffusion length of Al on Si [3.12]. The AlSb islands interrupt the long diffusion length of In adatoms, and act as sites for nucleation of the InSb film heterogeneously at the facets of the AlSb islands due to the decreased interfacial energies at these sites. The InSb islands spread laterally and coalesce to form a smoother thin film of improved crystalline quality as compared to the case without the AlSb buffer layer. The AlSb buffer is also expected to effectively relax

the mismatch strain by localizing misfit dislocations at the interface with Si [3.11]. The crystal structure of the InSb film improved further with increasing InSb growth temperature, as evident from the smoother surface morphology in figure 3.1(d) as compared to 3.1(b) or (c). The diffusion length of In increases with temperature, further promoting the nucleation at the AlSb island edges.

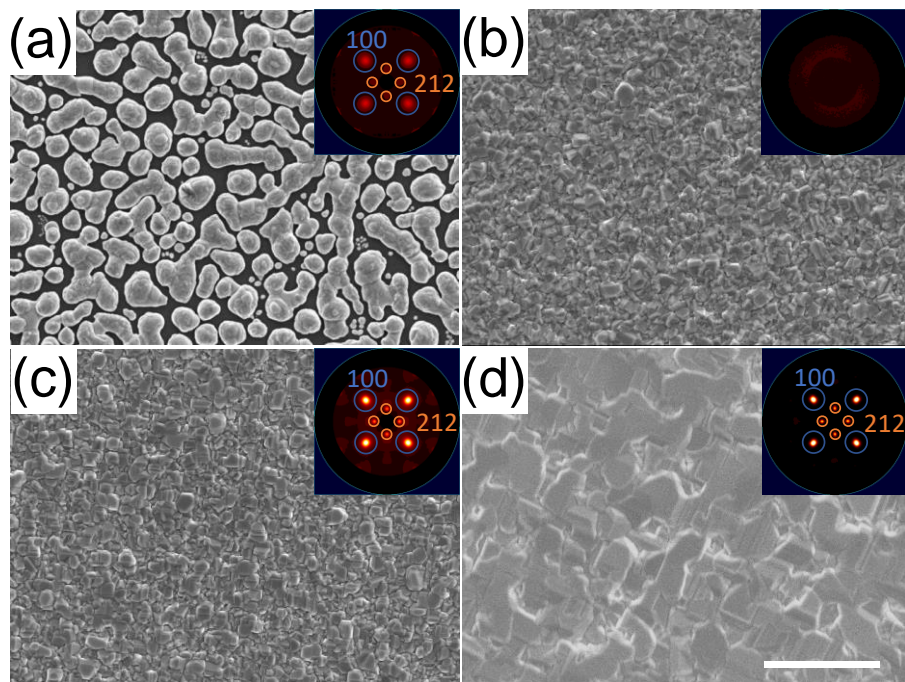


Figure 3.1 Plan view SEM images of InSb thin films grown (a) without an AlSb buffer layer at 550 °C, and with an AlSb buffer layer at (b) 500 °C, (c) 550 °C, and (d) 600 °C. Insets show the corresponding (220) X-ray diffraction pole figures. The scale bar in (d) indicates 5 μm , applicable to all images.

To further investigate the crystal quality of the thin films, X-ray diffraction (XRD) was performed with a Bruker D8 DISCOVER diffractometer equipped with a Co sealed tube source ($\lambda = 1.79026 \text{ \AA}$) and Vantec 500 area detector, and a Rigaku RU200 Cu rotating anode source ($\lambda = 1.54056 \text{ \AA}$) with a SMART6000 detector. The insets in figure 3.1 show

the (220) XRD pole figures for the InSb thin films grown at 550 °C without an AlSb buffer (figure 3.1(a)); and with an AlSb buffer grown at 500 °C (figure 3.1(b)), 550 °C (figure 3.1(c)), and 600 °C (figure 3.1(d)). All four films showed evidence of a randomly oriented polycrystalline component. In each (220) pole figure depicted, the four outer spots (blue outline) correspond to growth in the [100] direction normal to the substrate surface. The four inner spots (orange outline) indicate a secondary set of growth directions consisting of four equivalent [212] directions normal to the substrate surface. Analysis of the oriented components of the films was performed by the integrated intensity of each pole minus the integrated background, and evaluating the intensity contribution for each orientation component. The (100) and (212) spots are sharper for the InSb film grown at 550 °C with an AlSb buffer ((100) fraction = 42%) as compared to the reflections for the InSb film grown at 550 °C without AlSb ((100) fraction = 30%), indicating that the films become more highly oriented along the [100] direction with the addition of an AlSb buffer layer. The film grown at 500 °C with an AlSb buffer did not show any preferential growth directions and only random polycrystalline diffraction, as indicated by the lack of high intensity spots. The increase in temperature to 600 °C caused an observed increase in crystal quality and increase in (100) orientation fraction to 74%. Phase analysis (not shown) indicated a zincblende crystal structure for the InSb thin film in all cases. The film grown with no AlSb buffer exhibited a pure indium phase corresponding to indium accumulation on the Si surface. Thus, the polycrystalline structure improved with increasing InSb growth temperature when the AlSb buffer was present, as evident from the increasing polycrystalline grain size in the surface morphology of SEM images, and the absence of a

diffuse background and a narrowing in diffraction peaks in the pole figures. An increase in growth temperature allows for In adatoms to diffuse further before nucleation. This allows for the adatoms having a higher probability of nucleation at the edges of AlSb islands, inhibiting the growth of InSb islands and promoting smoother epitaxial film growth.

3.3.2 Nanowire Fabrication and Characterization

PMMA A5 photoresist was spin-coated onto the InSb thin film at 2000 rpm for 45 s, producing a layer approximately 400 nm in thickness. A Vistec EBPG 5000+ electron beam lithography (EBL) system was used to pattern separate 300 μm x 300 μm areas, each containing holes of different diameter (ranging from 300 nm to 1300 nm) and pitch (ranging from 1000 nm to 3500 nm) as confirmed by SEM (figure 3.2(a)). The resist was developed with a 1 min rinse in MIBK:IPA mixture at a 1:3 volume ratio, followed by an additional 1 min rinse in IPA. 120 nm of Ti was deposited by electron beam deposition at ~ 2 $\text{\AA}/\text{s}$. Lift-off was performed by sonication in acetone, leaving behind Ti discs as an etch mask (figure 3.2(b)).

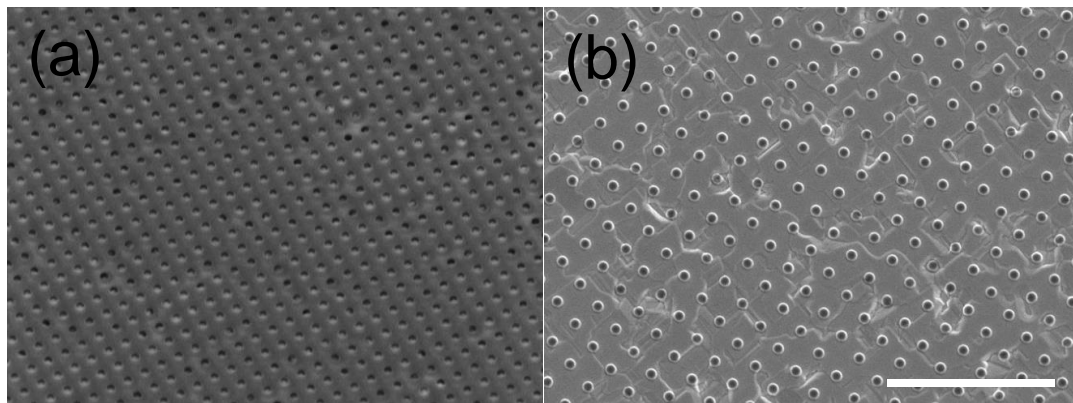


Figure 3.2 (a) 30° tilted SEM image of PMMA A5 resist showing an EBL pattern of holes with a pitch of 1000 nm and diameter of 400 nm. (b) Plan view SEM image of Ti mask remaining after liftoff for a pitch of 1500 nm and diameter of 600 nm. The scale bar indicates 5 μm for both images.

Reactive ion etching (RIE) was performed with an Oxford Instruments model ICP380 inductively coupled plasma RIE (ICP-RIE) using a gas mixture of $\text{CH}_4/\text{H}_2/\text{Ar}$ (15/50/5 sccm) [3.15]. The etch was performed for 1 hr and 55 min at a rate of 22 nm/min, thereby etching the entire InSb thin film and AlSb buffer layer down to the Si substrate. After RIE etching, a wet etch was performed in 10:1 H_2O :49% HF for 45 s to remove the Ti remaining on the top of the NWs [3.16]. The Ti etch did not have any observable effect on the NWs as observed by SEM. Representative SEM images of the resulting NW arrays are presented in figure 3.3.

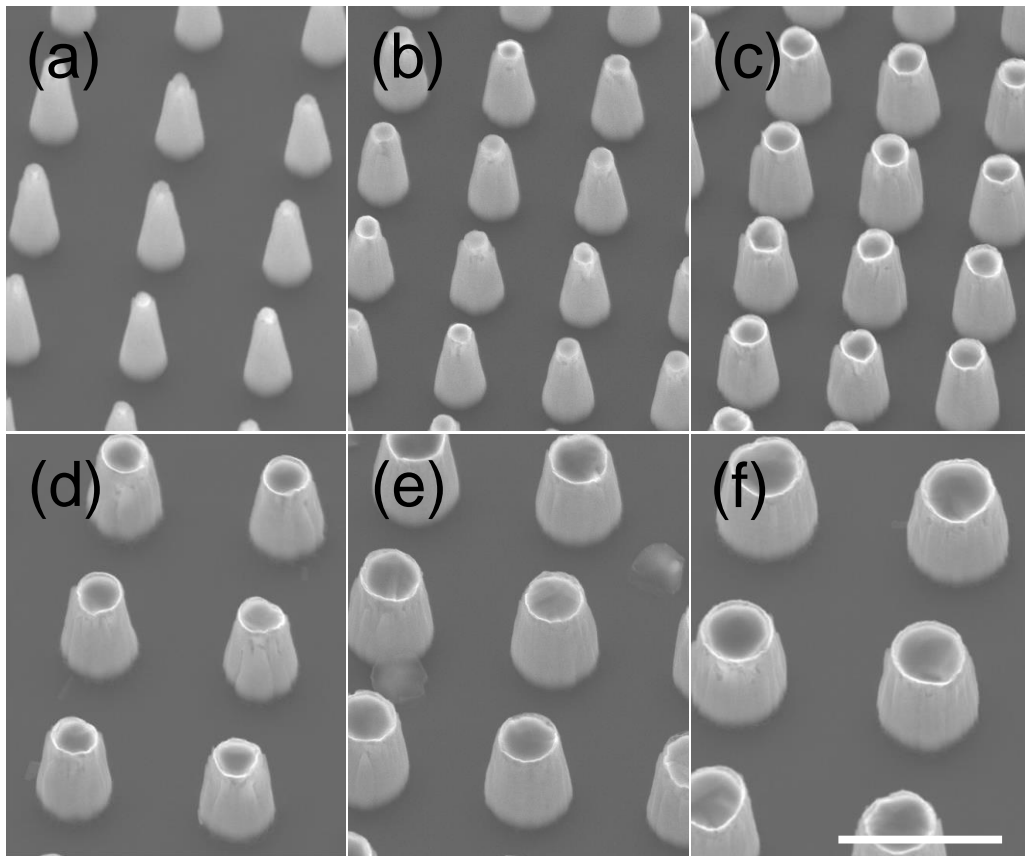


Figure 3.3 30° tilted SEM images of InSb NW arrays with diameter (D) and pitch (P) of (a) D = 300 nm, P = 2000 nm; (b) D = 500 nm, P = 2000 nm; (c) D = 700 nm, P = 2000 nm; (d) D = 900 nm, P = 3000 nm; (e) D = 1100 nm, P = 3000 nm, and (f) D = 1300 nm, P = 3500 nm. The scale bar in (f) indicates 3 μm , applicable to all images.

The length of the NWs was measured by SEM to be $2.3\ \mu\text{m}$, equal to the total thin film thickness (InSb and AlSb buffer). The NWs were observed to have tapered sidewalls with a taper angle between 2.0° to 6.2° . The values for the top and bottom diameters of the etched NWs are shown in figure 3.4. The top diameter is determined by the diameter of the Ti mask present during etching. The resultant tapering can be attributed to an “edge sheltering effect” during the RIE process, which may be improved by increasing the pressure [3.15].

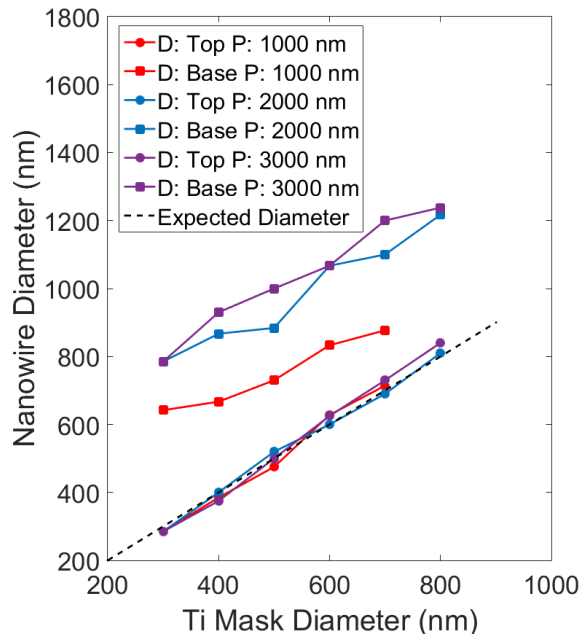


Figure 3.4 The top and base diameter of NWs obtained by SEM as compared to the Ti disc diameter (dashed line) for the indicated pitches (P: 1000 nm, 2000 nm, 3000 nm). The colored lines are a guide to the eye.

Scanning transmission electron microscopy (TEM), using a JEOL 2010F, was used to characterize the NW structure. The NW arrays were prepared for TEM by cutting a lamella through the center of a row of NWs of diameter 300 nm and pitch 1000 nm using

a FEI VERSA 3D focused ion beam (FIB) system. A layer of Pt was deposited on the selected NWs in preparation for FIB to protect them from damage during the milling process. Figure 3.5(a) shows a bright-field TEM image for two NWs including the underlying Si substrate prepared by FIB. Selected area electron diffraction (SAD) of a single NW was performed (figure 3.5(b)) on the circled region indicated in figure 3.5(a). The SAD pattern is indicative of a zincblende structure with twinning. An energy dispersive x-ray spectroscopy (EDX) line scan (figure 3.5(c)), performed in the TEM along the length of a single NW, confirmed that the films were etched completely down to the Si substrate.

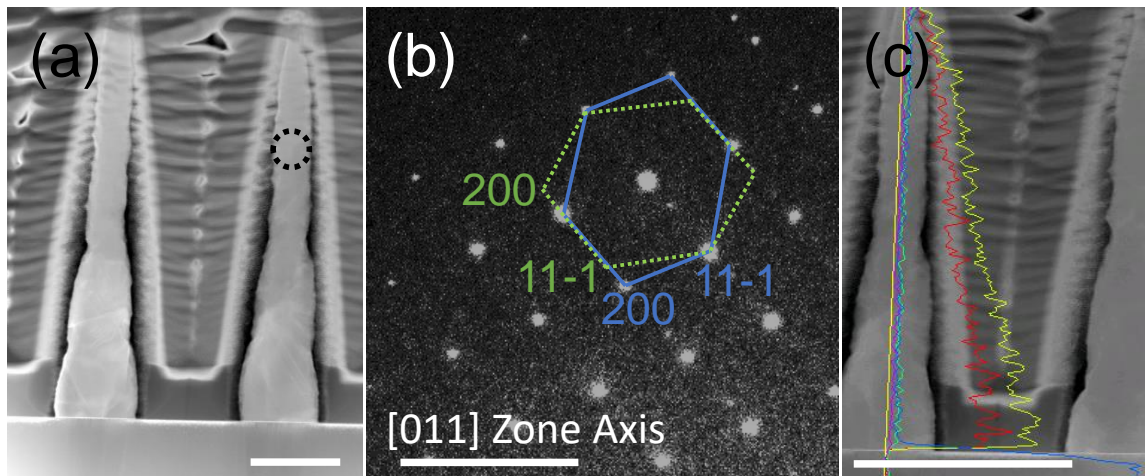


Figure 3.5 (a) TEM image of NWs with top diameter of 300 nm and pitch of 1000 nm. The space between NWs is filled with Pt for the FIB process. The scale bar depicts 0.5 μm . (b) Electron diffraction pattern from the selected area indicated by a circle in (a). The scale bar depicts 5 nm^{-1} . (c) EDX line scan along the length of a NW, showing the NW composition. Green, red, and blue represent In, Sb and Si, respectively. The scale bar depicts 1 μm .

Optical measurements were performed by Fourier transform infrared spectroscopy (FTIR) using a BRUKER Hyperion 3000 system with a halogen source and MCT detector. Reflectance ($R(\lambda)$) and transmittance ($T(\lambda)$) spectra were measured using a 15x objective lens, and the absorbance spectra ($A(\lambda)$) were calculated as $A(\lambda)=1-R(\lambda)-T(\lambda)$. A knife-edge

aperture was used to selectively illuminate only a single NW array. The same aperture was used to obtain a background measurement for the reflectance and transmittance spectra. A measurement performed on a gold-coated glass slide was used as a background measurement for the reflectance spectrum, while a measurement performed through unobstructed air was performed as a background measurement for the transmittance spectrum. The same technique was used to measure the absorptance from the thin film, prior to etching the film for the NW fabrication. Figure 3.6(a) shows the optical absorptance measured by FTIR for various diameters and pitches. Due to the high resistivity ($>100 \Omega\cdot\text{cm}$) of the Si substrate, negligible absorptance was obtained from the Si substrate as confirmed by FTIR measurements.

3.4 Discussion

The measured absorptance of the NWs spanned $1.61 \mu\text{m}$ to $6.86 \mu\text{m}$, with a peak absorptance which exceeded that due to the InSb thin film (dashed line). Figure 6(b) shows the expected absorptance simulated by COMSOL Multiphysics using the finite element method, as reported previously [3.6]. For ease of simulation and since absorption occurs mostly near the top of the NWs, each NW array was approximated by NWs of a constant diameter corresponding to the top diameter of the NWs. Comparison of figure 3.6(a) and (b) indicate reasonable agreement between the experimental and simulated spectra, confirming that the absorptance spectra were due to the HE_{11} resonant mode. The peak wavelength of the absorptance spectra shifted linearly with NW diameter, increasing by $0.53 \pm 0.2 \mu\text{m}$ for each 100 nm increase in NW diameter. The measured FTIR spectra

appeared broader than the theoretical data which can be attributed to the tapering of the NW sidewalls allowing for coupling of a wider range of wavelengths into the NWs.

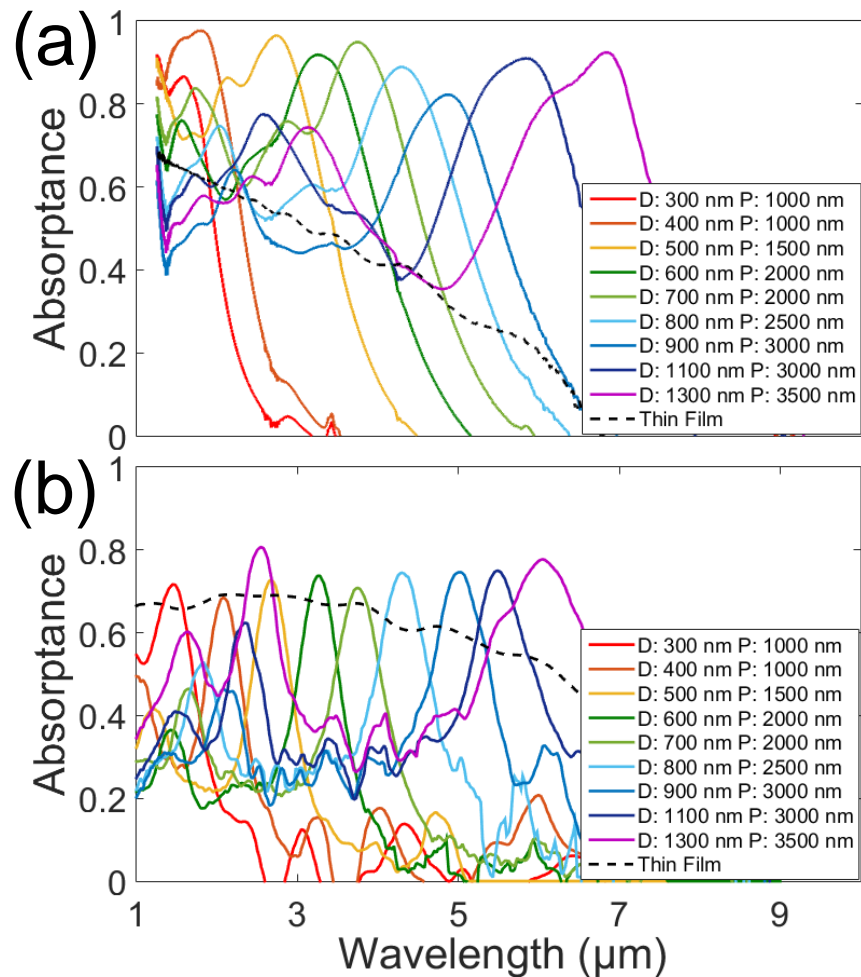


Figure 3.6 (a) FTIR absorbance spectra of NW arrays with the indicated diameter (D) and pitch (P). (b) Simulated absorbance spectra.

The peak absorbance measured in the NW arrays were approximately 10 to 20% greater than the theoretical peak absorbance obtained from the simulations. The reason for this discrepancy is not presently clear, but is likely due to differences between the

experimental illumination conditions and that used in the simulations. The infrared beam was confocal in the FTIR measurements with reflection measurements performed by illumination of the top of the samples (the NW side), and transmission measurements performed by illumination of the rear of the sample (the substrate side). On the other hand, for simplicity, the simulations were performed by plane wave illumination only on the top of the NWs. Conversely, the measured thin film absorptance showed a greater slope than the predicted absorptance. This discrepancy may be due to scattered light, caused by the film roughness and defects (polycrystalline nature of the film), that is not collected by the FTIR objective. The simulations do not include this light scattering effect.

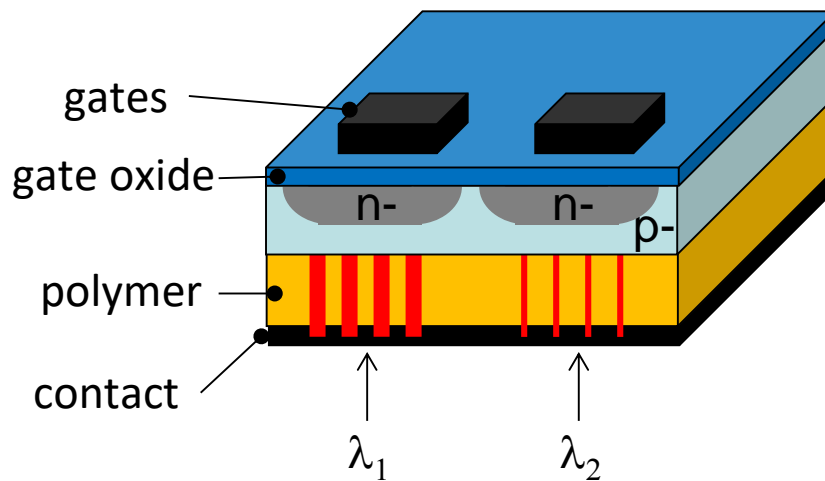


Figure 3.7 Schematic (not to scale) of possible NW IR sensor.

A potential device architecture is depicted in figure 3.7, consisting of NW arrays as IR absorbers monolithically integrated with a back-illuminated charge-coupled device (CCD). Gates and a gate oxide are added to a Si substrate (full read-out integrated circuit is not shown for simplicity). NWs are grown on the Si substrate, with a single pixel

comprised of two or more NW arrays (only two pixels are depicted in figure 3.7). Each NW array has a wavelength selective diameter. The NWs are planarized by a polymer [3.17] to facilitate contacting by a thin, IR-transparent metal film [3.18]. When illuminated, excess photoelectrons are collected from the NWs into the potential wells below each gate by a voltage bias. These electrons are then read out in a shift registry to form the IR image.

As mentioned, following ICP-RIE of the thin films, an etch in 10:1 H₂O:49% HF for 45 s was performed to completely remove the Ti mask from the NW tips to prevent unwanted light reflection. FTIR results demonstrating the optical absorption before and after the HF etch are presented in figure 3.8 for three NW diameters. Figure 3.8(a) presents FTIR data for NW arrays of 500 nm, 600 nm, and 700 nm diameter and a 2000 nm pitch. After the HF etch, a roughly 1% decrease in absorptance is observed, with a blue-shift of the HE₁₁ resonant peak by roughly 0.05 μm. Figure 3.8(b) presents similar FTIR data for NW arrays with the same NW diameter as figure 3.8(a), but with pitch increased to 3000 nm. The small blue-shift of the resonance peaks may be due to a diameter reduction of the pillars by the wet etching. The results of figure 3.8 show that the resonance peaks are due to a HE₁₁ resonance, rather than a plasmonic resonance associated with the Ti metal.

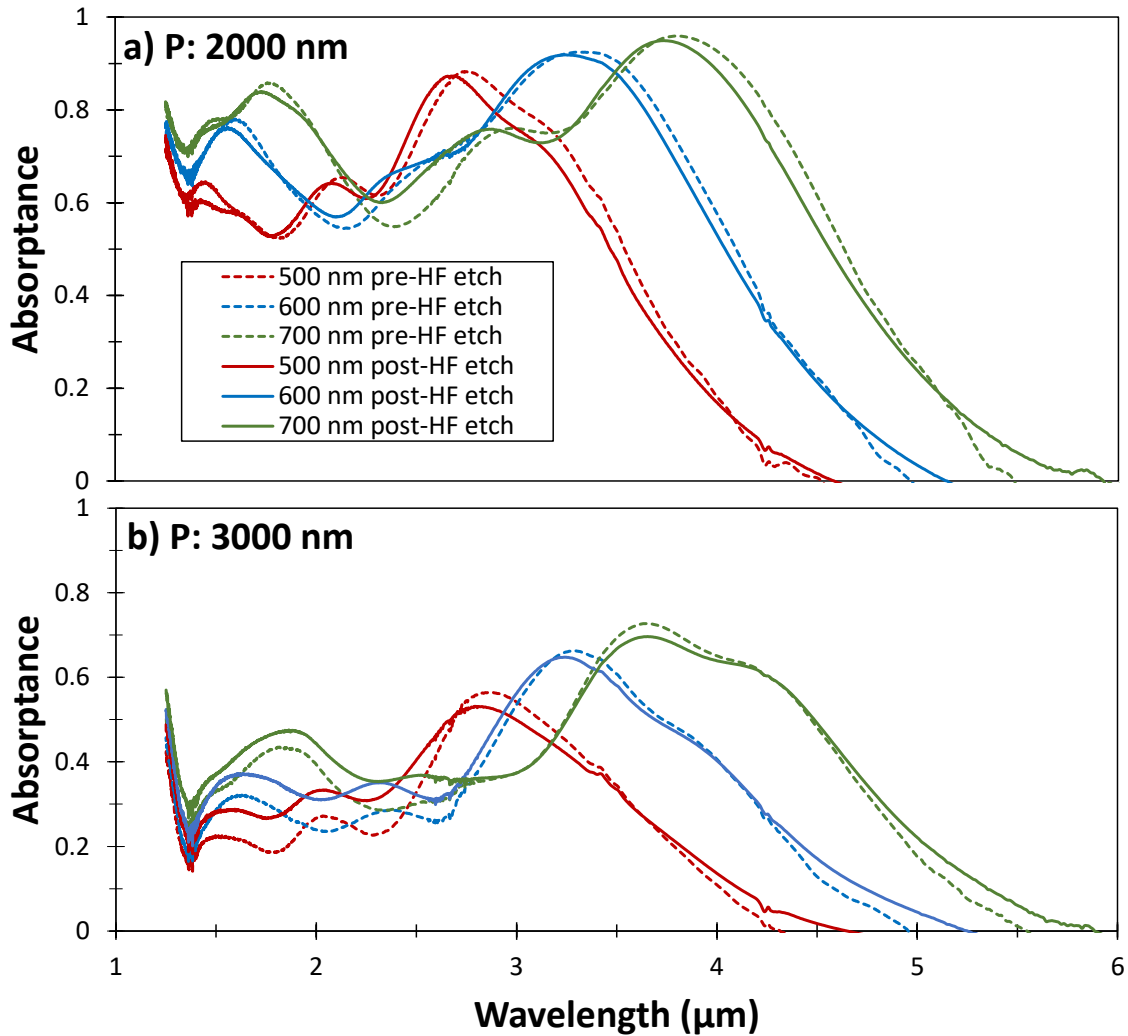


Figure 3.8 FTIR results demonstrating the absorbance before (dashed) and after (solid) an HF etch performed on InSb NWs. Arrays presented have diameter D : 500 nm, 600 nm, 700 nm, and pitch P : a) 2000 nm and b) 3000 nm.

SEM performed with the JEOL 7000 before and after Ti etching of a 1500 nm diameter and 4000 nm pitch array are presented in figure 3.9. After the etch, the polycrystalline grain boundaries of the InSb are observed, verifying removal of the Ti mask, although some NWs are observed with the Ti mask remaining. Higher resolution SEM

images taken with the FEI Magellan 400 are presented in figure 3.10(a) for 300 nm diameter and 1000 nm pitch arrays, and figure 3.10(b) for 800 nm diameter and 2000 nm pitch. Partial or full removal of Ti was observed.

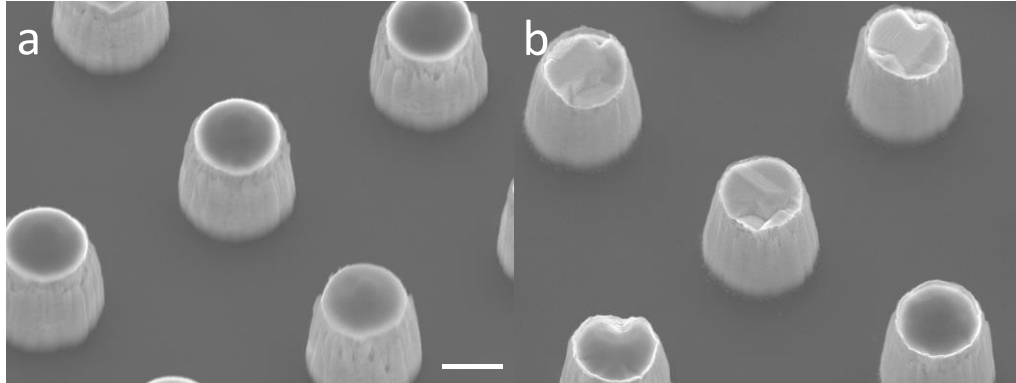


Figure 3.9 30° tilt SEM images of a 1500 nm diameter and 4000 nm pitch NW array (a) before and (b) after Ti mask removal. The scale bar in (a) corresponds to 1 μm and applies to both images.

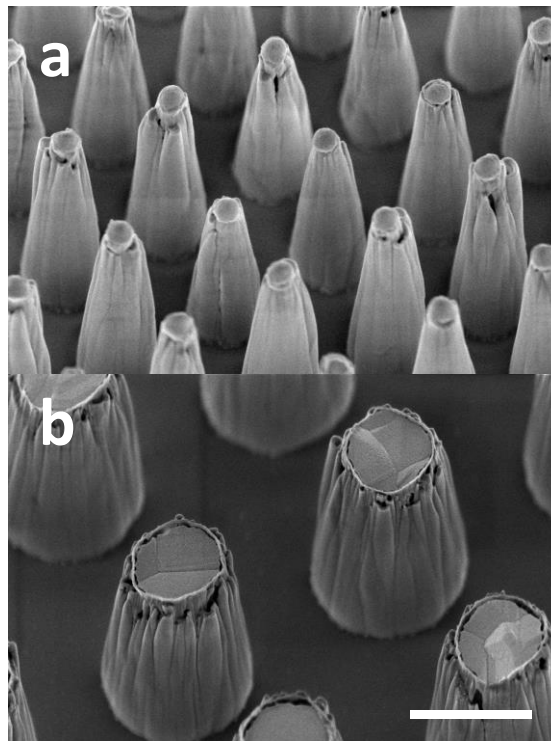


Figure 3.10 SEM images taken with the FEI Magellan 400 of two NW arrays post-HF etch to remove the Ti mask. (a) P: 1000 nm D: 300 nm, and (b) P: 2000 nm D: 800 nm. The scale bar in (b) corresponds to 1 μm and is applicable to both images.

3.5 Conclusion

InSb thin films were grown successfully on (100) Si by molecular beam epitaxy utilizing an AlSb buffer layer to alleviate island growth due to the large lattice mismatch between InSb and Si as confirmed by SEM and XRD. A top-down etching process provided a reliable method of fabricating InSb NW arrays with tunable diameter and pitch. The NWs were observed to have peak absorptance wavelength that was dependent on NW diameter and spanned the near-IR and mid-IR spectrum from 1.61 μm to 6.86 μm . Thus, multispectral absorptance was demonstrated with high wavelength tunability. The resulting InSb NWs may be used as IR filters, or as active photodetector pixel elements integrated with Si.

3.6 References

- [3.1] P. Martyniuk, J. Antoszewski, M. Martyniuk, L. Faraone and A. Rogalski, New concepts in infrared photodetector designs, *Appl. Phys. Rev.* 1 (2014) 041102
- [3.2] A. Rogalski, HgCdTe infrared detector material: history, status and outlook, *Rep. Prog. Phys.* 68 (2005) 2267
- [3.3] A. Rogalski, Infrared detectors for the future, *Acta Phys. Pol. A* 116 (2009) 389
- [3.4] A. Rogalski, J. Antoszewski and L. Faraone, Third-generation infrared photodetector arrays, *J. Appl. Phys.* 105 (2009) 091101
- [3.5] R.R. LaPierre, M. Robson, K.M. Azizur-Rahman and P. Kuyanov, A review of III-V nanowire infrared photodetectors and sensors, *J. Phys. D: Appl. Phys.* 50 (2017) 123001
- [3.6] K.M. Azizur-Rahman and R.R. LaPierre, Optical design of a mid-wavelength infrared InSb nanowire photodetector, *Nanotech.* 27 (2016) 315202
- [3.7] K.M. Azizur-Rahman and R.R. LaPierre, Wavelength-selective absorptance in GaAs, InP and InAs nanowire arrays, *Nanotech.* 26 (2015) 295202

- [3.8] N. Anttu and H. Xu, Efficient light management in vertical nanowire arrays for photovoltaics, *Opt. Exp.* 21 (2013) A558
- [3.9] B. Wang and P. Leu, Tunable and selective resonant absorption in vertical nanowires, *Opt. Lett.* 37 (2012) 3756
- [3.10] M. Robson, K.M. Azizur-Rahman, D. Parent, P. Wojdylo, D.A. Thompson, and R.R. LaPierre, Multispectral absorptance from large-diameter InAsSb nanowire arrays in a single epitaxial growth on silicon, *Nano Futures* 1 (2017) 035001
- [3.11] S. Hosseini Vajargah, M. Couillard, K. Cui, S. Ghanad-Tavakoli, B. Robinson, R.N. Kleiman, J.S. Preston and G.A. Botton, Strain relief and AlSb buffer layer morphology in GaSb heteroepitaxial films grown on Si as revealed by high-angle annular dark-field scanning transmission electron microscopy, *Appl. Phys. Lett.* 98 (2011) 082113
- [3.12] S. Hosseini Vajargah, S. Ghanad-Tavakoli, R.N. Kleiman, J.S. Preston and G.A. Botton, Growth mechanisms of GaSb heteroepitaxial films on Si with an AlSb buffer layer, *J. Appl. Phys.* 114 (2013) 113101
- [3.13] S. Hosseini Vajargah, S.Y. Woo, S. Ghanad-Tavakoli, R.N. Kleiman, J.S. Preston and G.A. Botton, Atomic-resolution study of polarity reversal in GaSb grown on Si by scanning transmission electron microscopy, *J. Appl. Phys.* 112 (2012) 093101
- [3.14] S.Y. Woo, S. Hosseini Vajargah, S. Ghanad-Tavakoli, R.N. Kleiman and G.A. Botton, Direct observation of anti-phase boundaries in heteroepitaxy of GaSb thin films grown on Si (001) by transmission electron microscopy, *J. Appl. Phys.* 112 (2012) 074306
- [3.15] G. Zhang, W. Sun, S. Xu, H. Zhao, H. Su and H. Wang, Inductively coupled plasma-reactive ion etching of InSb using $\text{CH}_4/\text{H}_2/\text{Ar}$ plasma, *J. Vac. Sci. Technol. A* 27 (2009) 681
- [3.16] K.R. Williams, K. Gupta and M. Wasilik, Etch rates for micromachining processing- Part II, *J. Microelectromech. Sys.* 12 (2003) 761
- [3.17] A.C.E. Chia and R.R. LaPierre, Contact planarization of ensemble nanowires, *Nanotechnology* 22 (2011) 245304
- [3.18] D. S. Ghosh, L. Martinez, S. Giurgola, P. Vergani and V. Pruneri, Widely transparent electrodes based on ultrathin metals, *Optics Lett.* 34 (2009) 325

Chapter 4 – InAsSb Pillars for Multispectral Long-wavelength Infrared Absorption

The results presented in this chapter are a part of the publication,

C. Goosney, V. Jarvis, J. Britten, and R. LaPierre, InAsSb pillars for multispectral long-wavelength infrared absorption, *Infrared Phys. Technol.* 111 (2020) 103566

This work discusses InAsSb pillar fabrication for LWIR detection. Hall effect results not included in the original publication were added to the end of section 4.4.

4.1 Abstract

InAsSb pillars were investigated for multispectral photodetection in the long wavelength infrared (LWIR) region. An $\text{InAs}_{0.19}\text{Sb}_{0.81}$ thin film was successfully grown on Si (100) substrate, utilizing an AlSb buffer layer to alleviate the large lattice mismatch. X-ray diffraction studies showed a majority [100] orientation of the as-grown films, with minor orientations arising as a result of twinning. Arrays of $\text{InAs}_{0.21}\text{Sb}_{0.79}$ pillars with diameters ranging from 1700 nm to 4000 nm were fabricated by a top-down reactive ion etching process. The arrays showed resonant optical absorption peaks in the LWIR region from 8 to 16 μm wavelength, dependent on the pillar diameter. The peak absorbance wavelength increased by 0.46 μm for each 100 nm increase in pillar diameter, demonstrating the multispectral tunability of such arrays.

4.2 Introduction

The majority of available infrared (IR) detectors are based on the principle of semiconductor materials that absorb photons with energy exceeding the material bandgap [4.1]. Currently, the II-VI material mercury cadmium telluride (MCT), $\text{Hg}_{1-x}\text{Cd}_x\text{Te}$, is most widely used for IR photodetection. The prominence of this material arises due to its direct bandgap that can be widely tuned throughout the short-wavelength IR (SWIR), mid-wavelength IR (MWIR) and long-wavelength IR (LWIR) regions by altering the composition [4.2-4.6]. Also, the high charge carrier mobility and low room temperature recombination rate of MCT are desirable for IR photodetectors [4.3]. Alternative materials for IR applications have been investigated due to various issues with MCT. CdZnTe substrates, although lattice-matched with MCT, are expensive and difficult to integrate with silicon readout integrated circuits [4.4, 4.5]. There are also issues with stability, uniformity, and toxicity of MCT detectors due to the use of mercury (Hg).

To address the aforementioned issues, III-V semiconductors may be used as an alternative to MCT [4.6, 4.7]. Among the III-V materials, the $\text{InAs}_{1-x}\text{Sb}_x$ compound semiconductor alloy is of particular interest for IR photodetection due to its small bandgap. Specifically, due to the large bandgap bowing parameter of the $\text{InAs}_{1-x}\text{Sb}_x$ material system [4.8], a bandgap minimum of 0.082 eV can be obtained (at the composition $\text{InAs}_{0.36}\text{Sb}_{0.64}$). This corresponds to a bandgap wavelength of 15.1 μm , enabling both MWIR and LWIR ranges. Various III-V photodetector technologies are available such as bulk substrates, quantum dots, and superlattices. These technologies are well described in Ref. [4.5, 4.6].

Infrared sensors must be integrated with Si electronics for image read-out and processing. Like MCT, III-V materials are not easily integrated with Si due to lattice-mismatch. To circumvent this issue, III-V materials are generally grown on expensive but lattice-matched III-V substrates. Alternatively, III-V materials may be grown directly on Si using buffer layers [4.9, 4.10], or transferred to Si using epitaxial lift-off and wafer bonding methods [4.11, 4.12].

It is also of great interest to develop multispectral or wavelength discriminating infrared detectors and cameras. Current multispectral cameras are fabricated using a multi-junction approach comprised of different material bandgaps grown on top of one another to absorb different regions of the infrared spectrum. These bandgaps are generally restricted to lattice-matched materials, which imposes a restriction on the possible absorption bands.

Previous studies have shown that semiconductor nanowires or pillars support an HE_{11} guided mode optical resonance, allowing for incident light to strongly couple with the allowed optical modes within the structure [4.13-4.16]. As a result, an array of semiconductor pillars can demonstrate higher optical absorption than that of a thin film of the same material and equivalent thickness. In addition, the HE_{11} mode coupling results in a resonant absorption peak at a wavelength proportional to the pillar diameter, allowing for multispectral absorption by tuning pillar geometry. Using this principle, Wu et al. [4.17] demonstrated red-shifting of absorption peaks in the SWIR region with increasing diameter (40 nm to 110 nm) of InAs nanowires grown by chemical beam epitaxy. Robson et al. [4.18] demonstrated multispectral absorption in the MWIR region with large diameter (440 – 520 nm) InAsSb nanowires grown by selective-area molecular beam epitaxy (MBE).

Svensson et al. [4.19] demonstrated diameter-dependent photocurrent in the MWIR region from InAsSb nanowires grown by metal-organic vapor phase epitaxy. Our recent work [4.20] demonstrated large diameter (300 nm – 1500 nm) InSb nanowires (pillars) fabricated by a top-down method on a Si (100) substrate using Ti discs as an etch mask. We demonstrated resonant absorptance peaks ranging from 1.61 μm to 6.86 μm in the SWIR and MWIR regions. To our knowledge, the principle of geometric tuning for multispectral absorption has not been demonstrated in the LWIR region.

In the present study, InAsSb thin films were grown directly on Si using an AlSb buffer layer. Large diameter InAsSb pillars were then fabricated by a top-down etching approach, similar to Ref. [4.20]. Multispectral absorption with wavelength tunability was achieved by adjusting the pillar diameter as opposed to the material composition. Hence, multispectral absorption is demonstrated in the LWIR range from a single material system without the need for bandgap tuning. This principle can be used as a new concept for multispectral imaging with improved wavelength selection compared to existing detectors.

4.3 Material and Methods

Molecular beam epitaxy (MBE) was used to grow InAsSb thin films on high resistivity ($> 100 \Omega\cdot\text{cm}$) Si (100) substrates. The high resistivity of the Si substrate minimized free carrier absorption, allowing optical transmission measurements of the films. The Si substrates were rinsed in a buffered HF bath for 1 min to remove native oxide prior to loading in the MBE preparation chamber. The substrates were degassed at 300 $^{\circ}\text{C}$ for 15 min in a preparation chamber before transfer into the MBE deposition chamber. Antimony

flux was supplied by a 3-stage valved cracker effusion cell, arsenic (As_2) flux was supplied by a hydride (AsH_3) gas cracker, and aluminum and indium were supplied by a standard solid-source effusion cell. For all samples, a 10 nm thick AlSb buffer layer was first grown on the Si substrate at a V/III flux ratio of 2, a growth rate of $0.1 \mu\text{m h}^{-1}$, and a growth duration of 6 min. Following the initial AlSb buffer layer, InAsSb was grown at the same temperature as that of the AlSb buffer. The InAsSb films were grown with an arsenic V/III flux ratio of approximately 2, and an antimony V/III flux ratio of 1. The growth rate was $0.5 \mu\text{m h}^{-1}$ for 5 h, yielding an InAsSb thin film of $2.5 \mu\text{m}$ thickness. The AlSb buffer layer and the InAsSb film were grown at $530 \text{ }^\circ\text{C}$ based on our previous studies [4.20]. Sample A was grown without dopants, while sample B and C were doped p-type with Be ($p \sim 5 \times 10^{18} \text{ cm}^{-3}$) and n-type with Te ($n \sim 5 \times 10^{18} \text{ cm}^{-3}$), respectively. This doping level is typical of that used for device structures to be considered in later studies. Be was supplied by a standard effusion cell, and Te from a GaTe effusion cell. The dopant flux was calibrated based on Hall effect measurements on thin films.

Pillars with controlled diameter were fabricated from sample A by etching the InAsSb film in a top-down approach. A PMMA A5 resist film was spin-coated onto the InAsSb film at 2000 rpm for 45 s, resulting in a layer approximately 400 nm thick. A Vistec EBPG 5000+ electron beam lithography (EBL) system was used to pattern an array of holes in the resist film. The PMMA A5 resist was developed with a 1 min rinse in MIBK:IPA mixture at a 1:3 vol ratio, followed by a 1 min rinse in IPA, revealing 40 different squares of $300 \mu\text{m} \times 300 \mu\text{m}$ area, each with different hole diameter and pitch (spacing between holes). Each square array consisted of holes of fixed diameter ranging from 1700 nm to 2500 nm

in 200 nm increments, and from 2500 nm to 4000 nm in 500 nm increments. The pitch (spacing between holes) ranged from 4000 nm to 6000 nm in 500 nm increments. The hole pattern in the resist was filled with approximately 120 nm of Ti deposited by electron beam deposition at a rate of $\sim 2 \text{ \AA/s}$. Metal lift-off was performed by sonication in acetone to remove the PMMA A5 resist, leaving behind an array of Ti discs. Pillars were fabricated by reactive ion etching (RIE), using the Ti discs as an etch mask. The etching was performed with an Oxford Instruments model ICP380 inductively-coupled plasma RIE (ICP-RIE) using a gas mixture of $\text{CH}_4/\text{H}_2/\text{Ar}$ (15/50/5 sccm) [4.21]. A study was performed to observe the effects of the RIE chamber pressure (7.5, 10, or 12.5 mTorr) on pillar sidewall tapering and surface damage by etching InSb thin films with an identical gas mixture. Based on the results of this study, the InAsSb film was etched for 1 h 10 min at an etch pressure of 12.5 mTorr.

After etching, the pillar morphology was characterized by scanning electron microscopy (SEM) using a FEI Magellan 400 instrument. Energy dispersive x-ray spectroscopy (EDS) was performed in the SEM to determine the InAsSb composition. 3D X-ray diffraction (XRD^3) texture analysis was performed with a Bruker D8 DISCOVER diffractometer utilizing a Cu sealed tube source ($\lambda = 1.54056 \text{ \AA}$) with a Vantec500 area detector. GADDS (Bruker) v4.1.6 software was used for X-ray data collection and pole figure analysis. Mercury 4.0 software was used for twin visualization [4.22].

Fourier transform infrared spectroscopy (FTIR) was performed using a BRUKER Hyperion 3000 system with a halogen source and MCT detector. Absorbance spectra ($A(\lambda)$) were calculated as $A(\lambda) = 1 - R(\lambda) - T(\lambda)$, where the reflectance spectra ($R(\lambda)$) and

transmittance spectra ($T(\lambda)$) were measured with a $15\times$ objective lens. A knife edge aperture was used to ensure only a single pillar array was illuminated. The same measurement parameters were used to collect background reference spectra using a gold-coated glass slide for reflectance measurements and unobstructed air for transmittance measurements. The identical setup was used to measure absorptance from the Si substrate and the InAsSb thin film prior to pillar etching.

4.4 Results and Discussion

The SEM images in figure 4.1(a) to (c) show the surface morphology of sample A, B, and C, respectively, after thin film deposition, indicating a polycrystalline film structure. To quantify the nature of the polycrystalline growth, XRD texture analysis was performed. Phase analysis (not shown) indicated a zincblende crystal structure of the $\text{InAs}_{1-x}\text{Sb}_x$ films. The film growth was dominated by a single orientation with the 3D XRD texture data indicating that the main film orientation for each sample was $[100]$ normal to the Si substrate. The 220 pole figures for each sample are shown in figure 4.2.

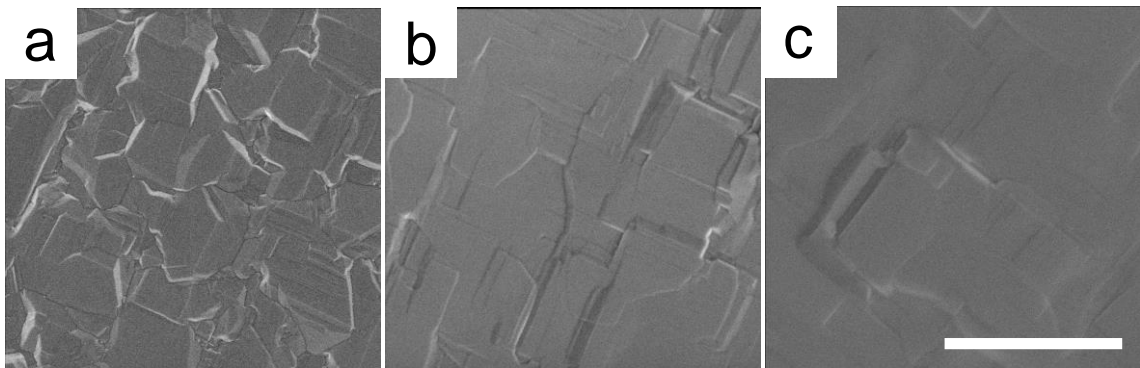


Figure 4.1 Plan view SEM images of InAsSb thin films for (a) sample A (undoped), (b) sample B (Be doped), and (c) sample C (Te doped). The scale bar in (c) corresponds to $2\ \mu\text{m}$ and is applicable to all images.

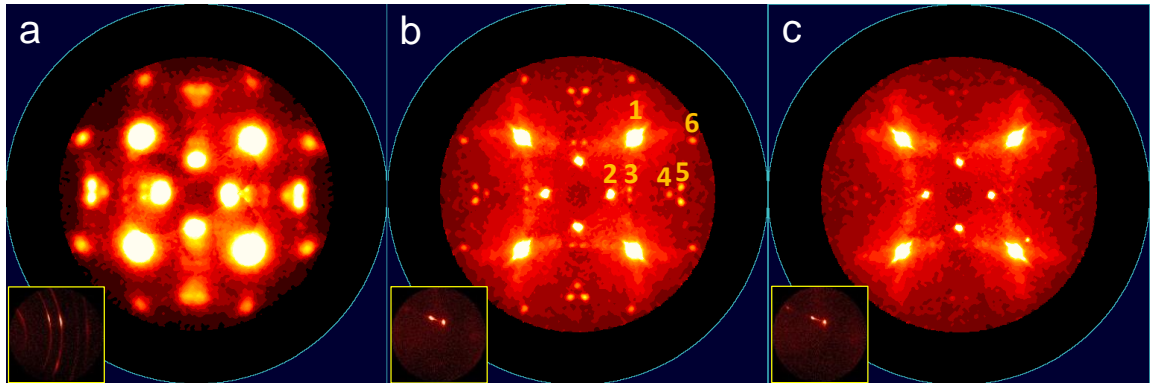


Figure 4.2 220 Pole figures of InAsSb thin films from (a) sample A (undoped), (b) sample B (Be doped) and (c) sample C (Te doped). The insets are single 2D frames from each 3D texture scan, taken from a similar region of reciprocal space, showing 200, 220 and 311 diffraction features for the corresponding samples. The spots labeled 1-6 in (b) are discussed in the text.

The insets in figure 4.2 are single 2D frames from each 3D texture scan, taken from a similar region of reciprocal space, showing 200, 220 and 311 diffraction spots for the corresponding samples. The inset for sample A shows that it contains a significant amount of randomly oriented grains; however, the other two samples are highly oriented. The intermediate intensity spots in the pole figures can be accounted for by [111] twinning in the film (Twin1), as depicted in figure 4.3. This occurs in multiple symmetry-related directions, giving rise to symmetry-related Twin1 spots. The Twin1 grains have their [122] direction normal to the substrate surface. The remaining minor spots on the pole figures can be predicted by a secondary [111] twinning on the Twin1 grains (Twin2). Twin2 grains have an approximate [184] direction normal to the substrate surface. The unique set of 220 pole figure spots are labeled 1 through 6 in figure 4.2(b). The intensity of spot 1 is from the main [100] orientation with contributions from two symmetry-related Twin1 orientations and two Twin2 orientations. Spot 2 arises from a Twin1 orientation and two Twin2

orientations. Spots 3, 4, 5 and 6 each have a single contribution from a Twin2 orientation.

Approximate orientation fractions are summarized in table 4.1.

Table 4.1 XRD texture analysis.

Sample	[100] (%)	Twin1 (%)	Twin2 (%)
A	70.3	28.3	1.4
B	94.4	5.3	0.3
C	97.7	2.0	0.3

Continuous diffraction rings and higher pole figure diffusivity are evident in sample A. The addition of Be or Te dopants in sample B and C, respectively, increased the [100] film orientation. Diffuse lines of scattering that connect spots from different twin components were observed in the 3D diffraction patterns of sample B and C. The insets in figure 4.2 show diffuse scattering between 220 and 113 reflections from twin-related grains. Figure 4.3 shows a random [111] layering model for the origin of the diffuse scattering.

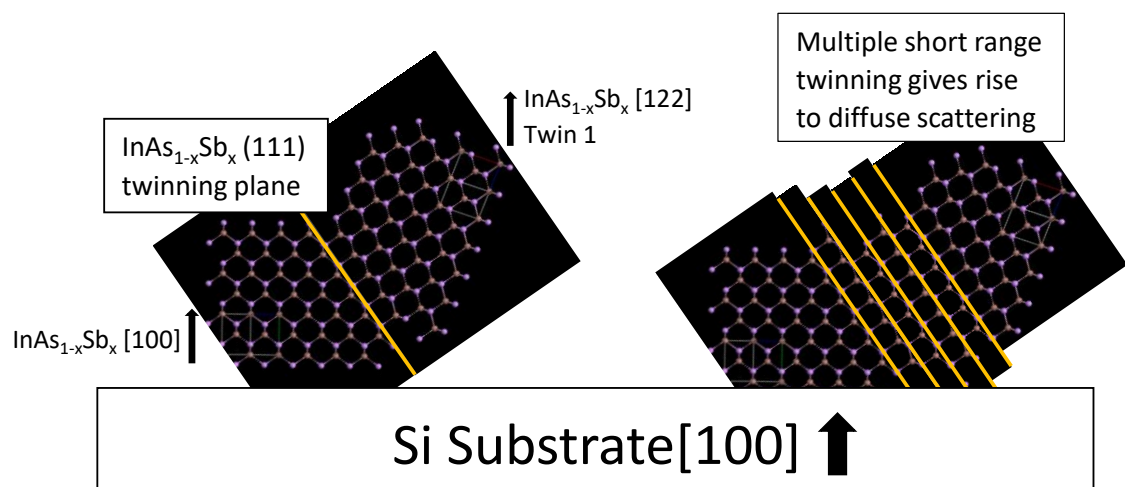


Figure 4.3 Twinning by 180° (or $\pm 60^\circ$) rotation about the [111] face of $\text{InAs}_{1-x}\text{Sb}_x$. Regions of multiple layer twinning account for the diffuse scattering observed in the 3D diffraction pattern. Twin planes are indicated by yellow lines.

EDS analysis indicated an $\text{InAs}_{1-x}\text{Sb}_x$ film composition of $x = 0.81 \pm 0.03$, 0.79 ± 0.03 and 0.79 ± 0.03 , averaged from 6 measurements across each sample, corresponding to a bandgap wavelength of 11.8, 12.4 and 12.4 μm [4.8] for sample A, B and C, respectively.

The effect of the AlSb buffer layer on InSb film growth was previously studied by the author in Ref. [4.20], and in a series of studies performed by Vajargah et al. [4.23-4.25] and Woo et al. [4.26]. InAsSb tends to form via the Volmer-Weber growth mode on the Si surface due to the large lattice mismatch. AlSb forms in a similar way, but at a much higher island density due to the lower diffusion length of Al on Si, as compared to In [4.24]. The AlSb islands interrupt the long diffusion length of In adatoms at the island facets during the initial stage of InAsSb deposition, promoting smoother epitaxial film growth and [100] film orientation rather than island nucleation.

Based on the texture analysis, the introduction of Be and Te dopant atoms during MBE growth of the InAsSb films appeared to promote (100) epitaxial growth. Although the Be and Te dopant fluxes are a fraction ($\sim 0.1\%$) of the film atomic density, the dopant atoms may accumulate (segregate) and form a monolayer on the sample surface rather than incorporate into the thin film. Te is well known to segregate and act as a surfactant during growth by promoting adatom incorporation, similar to the effect of an AlSb buffer layer [4.27-4.36]. Be has also been shown to exhibit surface segregation [4.37]. Hence, the addition of a Te or Be dopant flux substantially improved the crystalline quality of the thin films and promoted [100] orientation as shown in table 4.1. Further studies are needed to understand the effect of dopants on the InAsSb film morphology.

The SEM images of figure 4.4 show the morphology of the InAsSb pillar arrays after RIE etching of sample A. The Ti mask is still observable on the top of the pillars, although some etching of the Ti is observable in figure 4.4(d). The RIE etch resulted in pillars with near vertical sidewalls. The height of the pillars was $\sim 2.1 \mu\text{m}$ in length, almost equal to the InAsSb film thickness ($2.5 \mu\text{m}$), indicating that the RIE etch nearly reached the Si substrate.

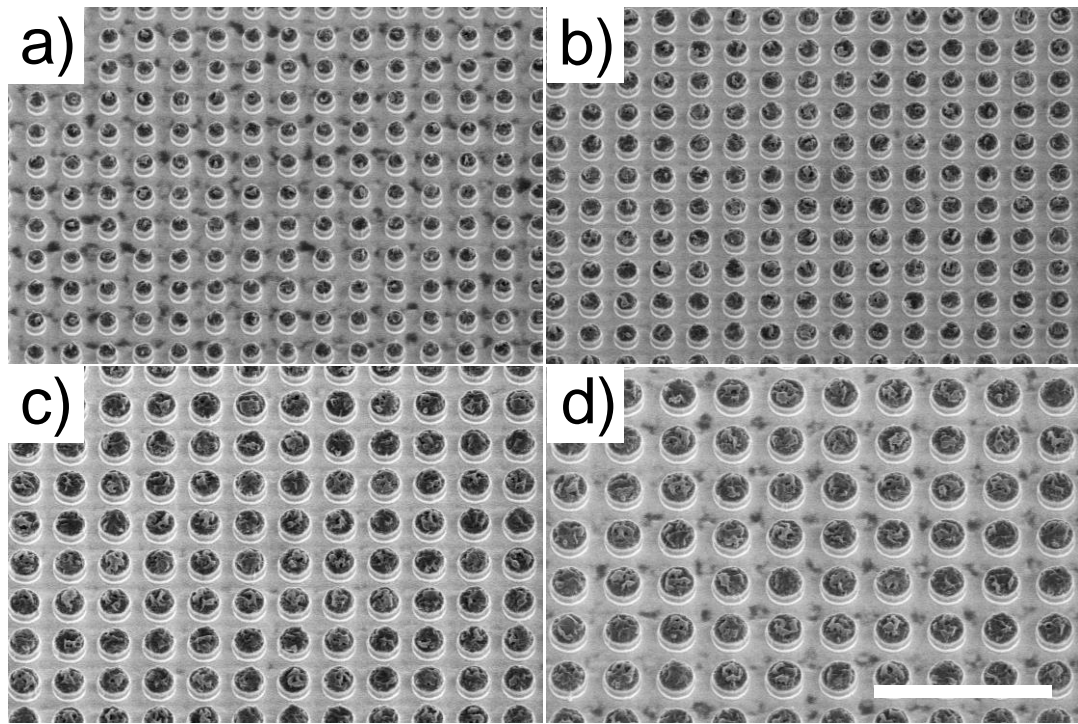


Figure 4.4 30° tilted SEM images of InAsSb pillars, corresponding to arrays with (a) 4000 nm pitch and 1900 nm diameter, (b) 4000 nm pitch and 2300 nm diameter, (c) 5000 nm pitch and 3500 nm diameter, and (d) 6000 nm pitch and 4000 nm diameter. The scale bar in (d) corresponds to $20 \mu\text{m}$ and is applicable to all images.

The absorptance of the Si substrate used in the present study is shown as the dashed line in figure 4.5a. This measurement confirms that the absorptance from the Si substrate was negligible, except for an absorption peak near $16 \mu\text{m}$, which is also observed in all

other spectra. This peak is caused by Si-Si vibrational modes in the Si substrate contributing to IR absorptance at approximately 615 cm^{-1} [4.38]. Hence, the dominant spectral features observed from the pillar arrays in figure 4.5a must be attributed to absorption in the pillars and not the Si substrate.

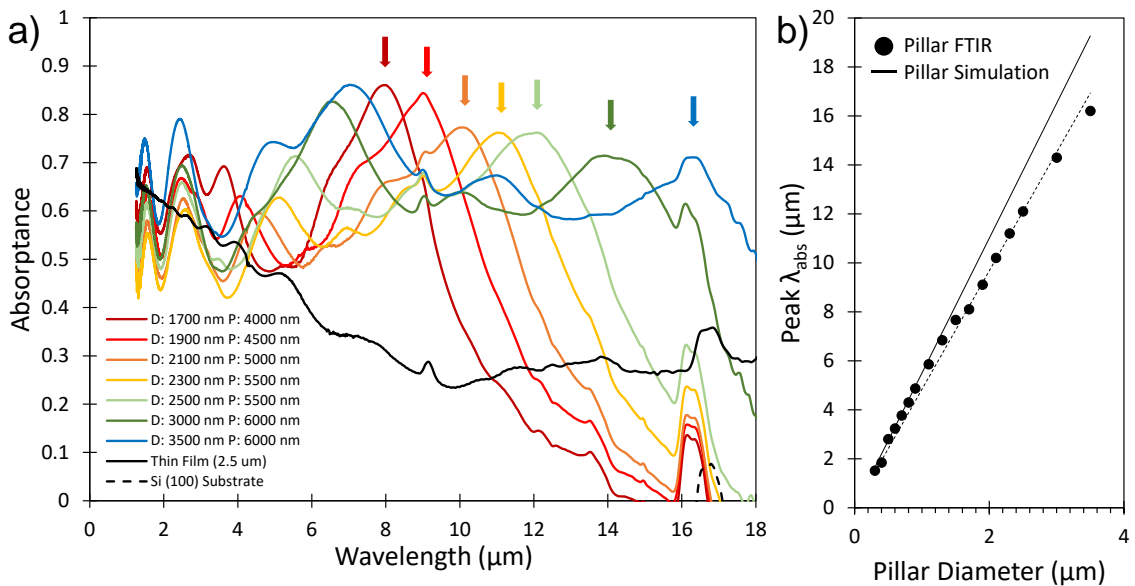


Figure 4.5 (a) FTIR absorbance spectra of InAsSb pillar arrays with different diameter (D) and pitch (P), absorbance from the as-grown thin film (black line), and absorbance from the Si substrate (dashed line). Arrows indicate the peak absorbance wavelengths. (b) Peak absorbance wavelength versus diameter for the HE_{11} mode. Solid circles are InSb pillars (chapter 3) and InAsSb pillars (chapter 4). Solid line shows the theoretical fit to the MWIR results obtained from Ref. [4.13], dashed line is the linear fit to experimental data.

As discussed in the introduction, the absorption peaks in the pillars of figure 4.5a (spanning from $8.1\ \mu\text{m}$ to $16.2\ \mu\text{m}$, indicated by an arrow) are due to the HE_{11} optical resonance mode in the pillar. Due to the electromagnetic boundary conditions of the HE_{11} mode, the peak absorbance wavelength roughly corresponds to the condition $D \sim \lambda/2n$ where λ is the incident wavelength and n is the refractive index of the pillar; i.e., a half-

wavelength of light “fits” within the pillar diameter. Hence, the peak absorptance wavelength is proportional to the pillar diameter, and red-shifts with increasing diameter. It is noteworthy that the optical absorption from the pillar arrays exceeded that from the thin film (black line in figure 4.5) due to the strong coupling of incident light into the HE_{11} mode. As the pillar diameter increases, new absorption peaks appear at shorter wavelengths due to the HE_{12} and higher order HE_{1n} modes; i.e., the pillars become multi-mode waveguides. In addition, the HE_{1n} resonance peaks broaden with increasing diameter due to increasing near-field coupling between adjacent pillars [4.13].

The average composition of sample A, as measured by XRD ($x = 0.81$), corresponds to a bandgap wavelength of $\sim 11.8 \mu\text{m}$ [4.8]. Hence, a cut-off is expected in the absorptance spectrum of the thin film above the bandgap wavelength of $11.8 \mu\text{m}$. Instead, the measured absorptance of the thin film in figure 4.5a saturated at a finite absorptance of ~ 0.3 above the expected cut-off wavelength. This finite absorptance is possibly due to tail states arising from the material doping and band-edge defect states at the pillar surface or inside the bulk (polycrystalline grain boundaries).

Figure 4.5b depicts the relation between pillar diameter and peak absorptance wavelength for previous results in the MWIR range [4.20] and the present results in the LWIR range. In the present study, each 100 nm increase in pillar diameter produced a $0.46 \mu\text{m}$ increase in peak absorptance wavelength (λ_{abs}), similar to that observed previously [4.20]. As discussed above, the peak absorption wavelength is expected to be proportional to the pillar diameter as confirmed in figure 4.5b. Prior optical simulations in the MWIR

range also confirmed this red-shift of the peak wavelength with pillar diameter [4.13], as shown by the dashed line in figure 4.5b. The present results in the LWIR range are a simple extension of that theory to larger pillar diameters.

Hall effect measurements were performed on the described undoped, p-type doped (Be, $5 \times 10^{18} \text{ cm}^{-3}$), and n-type doped (Te, $5 \times 10^{18} \text{ cm}^{-3}$) InAsSb thin films grown on semi-insulating ($> 100 \ \Omega \text{ cm}$) Si (100) substrates (sample A, B, and C, respectively). The results are presented in table 4.2. In the table, negative doping values indicates n-type behavior and positive doping values indicate p-type behavior.

Table 4.2 Hall effect measurement results

Dopant	Measured Mobility ($\text{cm}^2\text{V}^{-1}\text{s}^{-1}$)	Measured Doping (cm^{-3})	Intended Doping (cm^{-3})
Undoped	1.9×10^3	-3.5×10^{17}	/
Be (p-type)	6.2×10^2	-6.9×10^{17}	$+5 \times 10^{18}$
Te (n-type)	4.11×10^3	-1.5×10^{18}	-5×10^{18}

The Hall effect results indicated that, although the Be doped layer was expected to exhibit p-type doping, the measured doping was n-type with a doping concentration of $6.9 \times 10^{17} \text{ cm}^{-3}$. The undoped InAsSb film also demonstrated n-type doping. It has been observed that InAs and InAsSb thin films may report n-type results through Hall effect characterization [4.39-4.41]. This occurs due to the presence of an electron accumulation layer at the thin film surface as this accumulation layer acts as a parallel conductance channel [4.41]. This effect is observed more strongly in p-type layers [4.39]. For p-type layers, the significantly lower hole mobilities compared to electron mobilities will cause p-type layers to present n-type behavior with an overall lower measured electron mobility.

The surfactant behavior of the dopants may also lead to lower than unexpected doping values. Further studies are required to understand the doping behavior.

4.5 Conclusion

The ability to grow InAsSb thin films by MBE on Si (100) substrates, utilizing AlSb as a buffer layer, was demonstrated. The films were analyzed extensively via XRD and were shown to have grown epitaxially on the Si (100) surface with a dominant orientation along [100] normal to that of the substrate, and minor orientations caused by twinning. Large diameter InAsSb pillars were fabricated by a top-down RIE etching procedure, demonstrating the ability to produce consistent diameter and pitch over a wide range of values. Multispectral absorption from 8.1 to 16.2 μm was demonstrated due to the HE_{11} resonance with a peak absorptance controlled by the pillar diameter. The peak absorptance wavelength increased by 0.46 μm for each 100 nm increase in pillar diameter.

4.6 References

- [4.1] A. Rogalski, *Infrared Detectors*, Boca Raton, FL. CRC Press, 2010
- [4.2] P. Martyniuk, J. Antoszewski, M. Martyniuk, L. Faraone, and A. Rogalski, New concepts in infrared photodetector designs, *Appl. Phys. Rev.* 1 (2014) 041102
- [4.3] A. Rogalski, HgCdTe infrared detector material: history, status and outlook, *Rep. Prog. Phys.* 68 (2005) 2267
- [4.4] A. Rogalski, Infrared detectors for the future, *Acta Phys. Pol. A* 116 (2009) 389
- [4.5] A. Rogalski, J. Antoszewski, and L. Faraone, Third-generation infrared photodetector arrays, *J. Appl. Phys.* 105 (2009) 091101

- [4.6] M. Kinch, The Future of Infrared; III-Vs or HgCdTe?, *J. Electron. Mater.* 44 (2015), 2969-2976
- [4.7] S. Bianconi and H. Mohseni, Recent advances in infrared imagers: toward thermodynamic and quantum limits of photon sensitivity, *Rep. Prog. Phys.* 83 (2020) 044101
- [4.8] I. Vurgaftman, J. Meyer, and L. Ram-Mohan, Band parameters for III-V compound semiconductors and their alloys, *J. Appl. Phys.* 89 (2001) 5815
- [4.9] Q. Durlin, J.P. Perez, L. Cerutti, J.B. Rodriguez, T. Cerba, T. Baron, E. Tournie, and P. Christol, Midwave infrared barrier detector based on Ga-free InAs/InAsSb type-II superlattice grown by molecular beam epitaxy on Si substrate, *Infrared Physics and Technology* 96 (2019) 39
- [4.10] E. Delli, V. Letka, P.D. Hodgson, E. Repiso, J.P. Hayton, A. P. Craig, Q. Lu, R. Beanland, A. Krier, A.R.J. Marshall, and P.J. Carrington, Mid-Infrared InAs/InAsSb superlattice nBn photodetector monolithically integrated onto silicon, *ACS Photonics* 6 (2019) 538
- [4.11] Y. Zhang, A. Haddadi, R. Chevallier, A. Dehzangi, and M. Razeghi, Thin-film antimonide-based photodetectors integrated on Si, *IEEE J. Quant. Electron.* 54 (2018) 4000207
- [4.12] M. Zamiri, B. Klein, T. Schuler-Sandy, S. Myers, V. Dahiya, F. Cavallo, and S. Krishna, Indium-bump-free antimonide superlattice membrane detectors on silicon substrates, *Appl. Phys. Lett.* 108 (2016) 091110
- [4.13] K.M. Azizur-Rahman, and R.R. LaPierre, Optical design of a mid-wavelength infrared InSb nanowire, *Nanotech.* 27 (2016) 315202
- [4.14] K.M. Azizur-Rahman, and R.R. LaPierre, Wavelength-selective absorptance in GaAs, InP and InAs nanowire arrays, *Nanotech.* 26 (2015) 295202
- [4.15] N. Anttu, and H. Xu, Efficient light management in vertical nanowire arrays for photovoltaics, *Opt. Exp.* 21 (2013) A558
- [4.16] B. Wang and P. Leu, Tunable and selective resonant absorption in vertical nanowires, *Opt. Lett.* 37 (2012) 3756
- [4.17] P. Wu, N. Anttu, H. Xu, L. Samuelson, and M. Pistol, Colorful InAs nanowire arrays: from strong to weak absorption with geometrical tuning, *Nano. Lett.* 12 (2012) 1990

- [4.18] M. Robson, K.M. Azizur-Rahman, D. Parent, P. Wojdylo, D.A. Thompson, and R.R. LaPierre, Multispectral absorptance from large-diameter InAsSb nanowire arrays in a single epitaxial growth on silicon, *Nano Futures* 1 (2017) 035001
- [4.19] J. Svensson, N. Anttu, N. Vainorius, B. Borg, and L. Wernersson. Diameter-dependent photocurrent in InAsSb nanowire infrared photodetectors, *Nano Lett.* 13 (2013) 1380
- [4.20] C. Goosney, V. Jarvis, D. Wilson, N. Goktas, and R. LaPierre, InSb nanowires for multispectral infrared detection, *Semicond. Sci. Technol.* 34 (2019) 035023
- [4.21] G. Zhang, W. Sun, S. Xu, H. Zhao, H. Su, and H. Wang, Inductively coupled plasma-reactive ion etching of InSb using $\text{CH}_4/\text{H}_2/\text{Ar}$ plasma, *J. Vac. Sci. Technol. A* 27 (2009) 681
- [4.22] C.F. Macrae, I. Sovago, S.J. Cottrell, P.T.A. Galek, P. McCabe, E. Pidcock, M. Platings, G.P. Shields, J.S. Stevens, M. Towler, and P.A. Wood, Mercury 4.0: from visualization to analysis, design and prediction, *J. Appl. Cryst.* 53 (2020) 226
- [4.23] S. Hosseini Vajargah, M. Couillard, K. Cui, S. Ghanad-Tavakoli, B. Robinson, R.N. Kleiman, J.S. Preston, and G.A. Botton, Strain relief and AlSb buffer layer morphology in GaSb heteroepitaxial films grown on Si as revealed by high-angle annular dark-field scanning transmission electron microscopy, *Appl. Phys. Lett.* 98 (2011) 082113
- [4.24] S. Hosseini Vajargah, S. Ghanad-Tavakoli, R.N. Kleiman, J.S. Preston, and G.A. Botton, Growth mechanisms of GaSb heteroepitaxial films on Si with an AlSb buffer layer, *J. Appl. Phys.* 114 (2013) 113101
- [4.25] S. Hosseini Vajargah, S.Y. Woo, S. Ghanad-Tavakoli, R.N. Kleiman, J.S. Preston, and G.A. Botton, Atomic-resolution study of polarity reversal in GaSb grown on Si by scanning transmission electron microscopy, *J. Appl. Phys.* 112 (2012) 093101
- [4.26] S.Y. Woo, S. Hosseini Vajargah, S. Ghanad-Tavakoli, R.N. Kleiman, and G.A. Botton, Direct observation of anti-phase boundaries in heteroepitaxy of GaSb thin films grown on Si (001) by transmission electron microscopy, *J. Appl. Phys.* 112 (2012) 074306
- [4.27] M. Bennett, C. Dunscombe, A. Cafolla, J. Cairns, J. Macdonald, and R. Williams, Photoemission studies of the surfactant-aided growth of Ge on Te-terminated Si (100), *Surf. Sci.* 380 (1997) 178
- [4.28] N. Grandjean, J. Massies, and V. Etgens, Delayed relaxation by surfactant action in highly strained III-V semiconductor epitaxial layers, *Phys. Rev. Lett.* 69 (1992) 796

- [4.29] S. Lee and G. Stringfellow, Influence of tellurium doping on step bunching of GaAs (001) vicinal surfaces grown by organometallic vapor phase epitaxy, *Appl. Phys. Lett.* 73 (1998) 1703
- [4.30] S. Lee, C. Fetzer, G. Stringfellow, D. Lee, and T. Seong, Te doping of GaInP: ordering and step structure, *J. Appl. Phys.* 85 (1999) 3590
- [4.31] P. Dai, M. Tan, Y. Wu, L. Ji, L. Bian, S. Lu, and H. Yang, Solid-state tellurium doping of AlInP and its application to photovoltaic devices grown by molecular beam epitaxy, *J. Cryst. Growth* 413 (2015) 71
- [4.32] R. Wixom, L. Rieth, and G. Stringfellow, Te surfactant effects on the morphology of patterned (001) GaAs homoepitaxy, *J. Cryst. Growth* 269 (2004) 276
- [4.33] F. Newman, M. Stan, S. Murray, and C. Murray, Tellurium surfactant effects in the growth of lattice mismatched $\text{InAs}_x\text{P}_{1-x}$ by metal organic vapor-phase epitaxy, *J. Cryst. Growth* 272 (2004) 650
- [4.34] B. Paquette, B. Ilahi, V. Aimez, and R. Arès, Inhibition of Te surfactant effect on the surface morphology of heavily Te-doped GaAs, *J. Cryst. Growth* 383 (2013) 30
- [4.35] T. Orzali, A. Vert, R. Lee, A. Norvilas, G. Huang, J. Herman, R. Hill, and S. Papa Rao, Heavily tellurium doped n-type InGaAs grown by MOCVD on 300 mm Si wafers, *J. Cryst. Growth* 426 (2015) 243
- [4.36] R. Miwa, A. Ferraz, W. Rodrigues, and H. Chacham, Adsorption and dimer exchange processes in surfactant-mediated epitaxial growth of GaAs/InAs, *Surf. Sci* 415 (1998) 20
- [4.37] S.V. Ivanov, P.S. Kop'ev, and N.N. Ledentsov, Interplay of beryllium segregation and diffusion in heavily doped GaAs and AlGaAs grown by molecular beam epitaxy (thermodynamic analysis), *J. Cryst. Growth* 108 (1991) 661
- [4.38] D. Chandler-Horowitz and P. M. Amirtharaj, High-accuracy, midinfrared ($450 \text{ cm}^{-1} \leq \omega \leq 4000 \text{ cm}^{-1}$) refractive index values of silicon, *J. Appl. Phys.* 97 (2005) 123526
- [4.39] T. Krug, L. Botha, P. Shamba, T. Baisitse, A. Venter, J. Engelbrecht, and J. Botha, Electrical properties of undoped and doped MOVPE-grown InAsSb, *J. Cryst. Growth* 298 (2007) 163-167
- [4.40] O. Pitts, D. Lackner, S. Cherng, and S. Watkins, Growth of InAsSb/InPSb heterojunctions for mid-IR detector applications, *J. Cryst. Growth* 310 (2008) 4858-4861

[4.41] H. Wieder, Transport coefficients of InAs epilayers, *Appl. Phys. Lett.* 25 (1974) 206

Chapter 5 – Current-Voltage Characterization of InSb Photoconductor and Photovoltaic Devices

Following the work presented in chapter 3 and 4 regarding InSb and InAsSb thin film growths and pillar etching, doped p-i-n thin film devices were fabricated to further characterize the InSb thin films.

5.1 Introduction

InSb is a material of interest for infrared (IR) photodetection. The bandgap of InSb is 0.17 eV at 300 K, corresponding to a wavelength of 7.3 μm , enabling the mid-wavelength infrared (MWIR) regime [5.1]. Of the relevant IR materials for operation in the IR wavelengths, InSb has the highest electron mobility at room temperature of $80,000 \text{ cm}^2 \text{ V}^{-1} \text{ s}^{-1}$, compared to a HgCdTe (MCT) electron mobility of $10,000 \text{ cm}^2 \text{ V}^{-1} \text{ s}^{-1}$, making it a desirable alternative [5.2]. As with MCT, however, InSb has proven difficult to integrate with silicon electronics due to the large lattice mismatch of 19.3% between them. InSb detectors have been grown on InSb substrates [5.3] or substrates of other III-V's such as GaAs with a lower lattice mismatch of 14.5% in conjunction with a buffer layer [5.4]. InSb has also been grown on Si utilizing a buffer layer consisting of 450 nm of Ge, 200 nm of GaAs, and 100 nm of unintentionally doped InSb to alleviate defects caused by lattice mismatch [5.5]. A photodetector device, containing an InAsSb barrier layer, demonstrated a responsivity of 0.7 A/W and a quantum efficiency of 16.3% at 80 K [5.5]. A more complicated buffer system on Si, consisting of AlSb, GaSb and the formation of InSb

quantum dots, was used for InSb growth on (100) Si [5.6]. If the buffer layer was formed in a way to ensure a top layer of AlSb before the primary InSb growth, the InSb film demonstrated a higher mobility and responsivity than if it was on GaSb. Previous studies demonstrated the ability for a thin 10 nm AlSb buffer layer on a Si (100) surface to greatly promote epitaxial growth of InSb through the formation of AlSb islands [5.7]. To obtain bandgap tunability, a ternary alloy of $\text{InAs}_{1-x}\text{Sb}_x$ can be made, allowing for a minimum bandgap of 0.082 eV at the composition $\text{InAs}_{0.36}\text{Sb}_{0.64}$, corresponding to a wavelength of 15.1 μm [5.8]. In this chapter, p-i-n InSb thin films grown on Si (100) are processed into InSb photoconductor and photovoltaic devices.

5.2 Experimental Details

5.2.1 Thin Film Growth

Molecular beam epitaxy (MBE) was used to grow a p-i-n junction thin film structure of InSb on an n-type (As-doped, $\leq 0.005 \Omega \text{ cm}$) Si (100) substrate, utilizing a thin AlSb buffer layer to assist in mitigating defects caused by a large lattice mismatch, as reported in the earlier chapters. A schematic of the intended device structure is shown in figure 5.1. Prior to loading into the MBE, the substrates were rinsed in buffered HF for 1 min to remove native oxide. The substrates were degassed at 300 °C for 15 min in a preparation chamber before transfer into the main deposition chamber. Antimony flux was supplied through a 3-stage valved cracker effusion cell, aluminum and indium were supplied through a standard solid-source effusion cell, and arsenic was supplied as As_2 by a gas cracker from an AsH_3 source. To start the growth, a V/III ratio of 2 and a growth rate of 0.1 $\mu\text{m h}^{-1}$ for 6

min yielded an AlSb buffer layer of 10 nm thickness. The InSb layers were grown with a V/III ratio of 1.2 and a growth rate of $0.5 \mu\text{m h}^{-1}$. The undoped InSb region was grown for 4 h resulting in a $2 \mu\text{m}$ thickness. The p-type region was doped with nominally $2 \times 10^{18} \text{ cm}^{-3}$ of Be from a solid-source effusion cell, and was grown for 1 h resulting in a $0.5 \mu\text{m}$ thickness. The substrate was held at $600 \text{ }^\circ\text{C}$ for all portions of the growth, since prior 3D X-ray diffraction (XRD³) studies demonstrated higher quality epitaxial growth on the lattice mismatched Si substrate at this temperature [5.7]. In Figure 5.1, i-InSb indicates intrinsic InSb, although unintentional doping means the film will not be intrinsic but likely n-doped as described by Hall measurements in chapter 4.

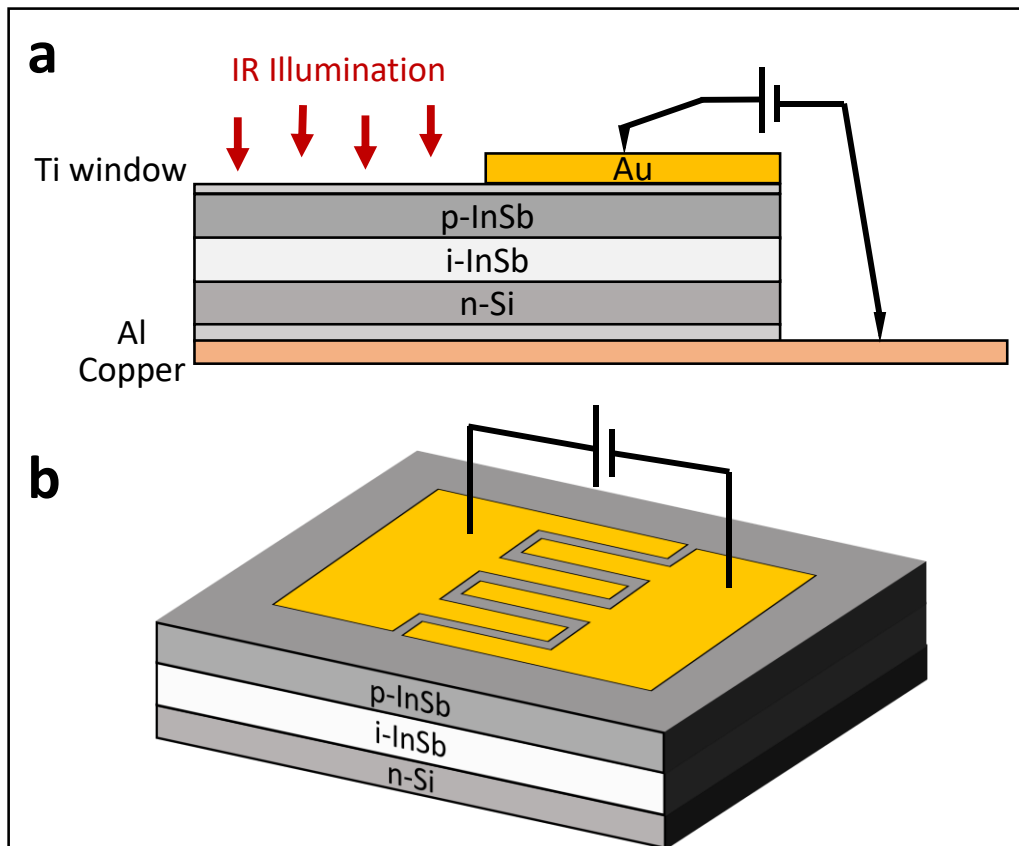


Figure 5.1 a) Cross-sectional view of thin film growth and photovoltaic device structure. b) Schematic of the photoconductive device.

5.2.2 Photolithography and Pattern Description

MicroChem LOR 5A lift-off resist was spun onto the InSb thin film sample at 4000 RPM for 30 s and soft-baked at 185 °C for 3 min. This initial layer of LOR 5A is intended to aid with lift-off after metal deposition, specifically with the smaller 5 μm and 10 μm features of the interdigitated photoconductor contact pattern. MICROPOSIT S1818 was then spun onto the sample at 4000 RPM for 30 s and soft-baked at 110 °C for 2 min.

The Heidelberg μPG 101 direct write system was used to transfer two custom designed patterns corresponding to a photoconductive and photovoltaic device, as shown in figure 5.2. The interdigitated photoconductor pattern consisted of a 4x4 grid of two 0.5x1.0 mm² rectangular contact pads separated by 1 mm long interdigitated fingers of varying width (W) and separation (S) combinations of 5 μm , 10 μm , 30 μm and 100 μm . The convention used to identify a pad is Wx Sy, indicating a x μm width and y μm separation. The square top contacts for photovoltaic devices consisted of three initial square patterns of 500x500 μm^2 , 250x250 μm^2 , and 100x100 μm^2 areas comprised of a thin (12.5 nm) Ti layer, allowing for illumination of the thin film through the semi-transparent Ti window. Contact pads overlapped each Ti window, leaving 350x350 μm^2 , 180x180 μm^2 and 60x70 μm^2 exposed for illumination.

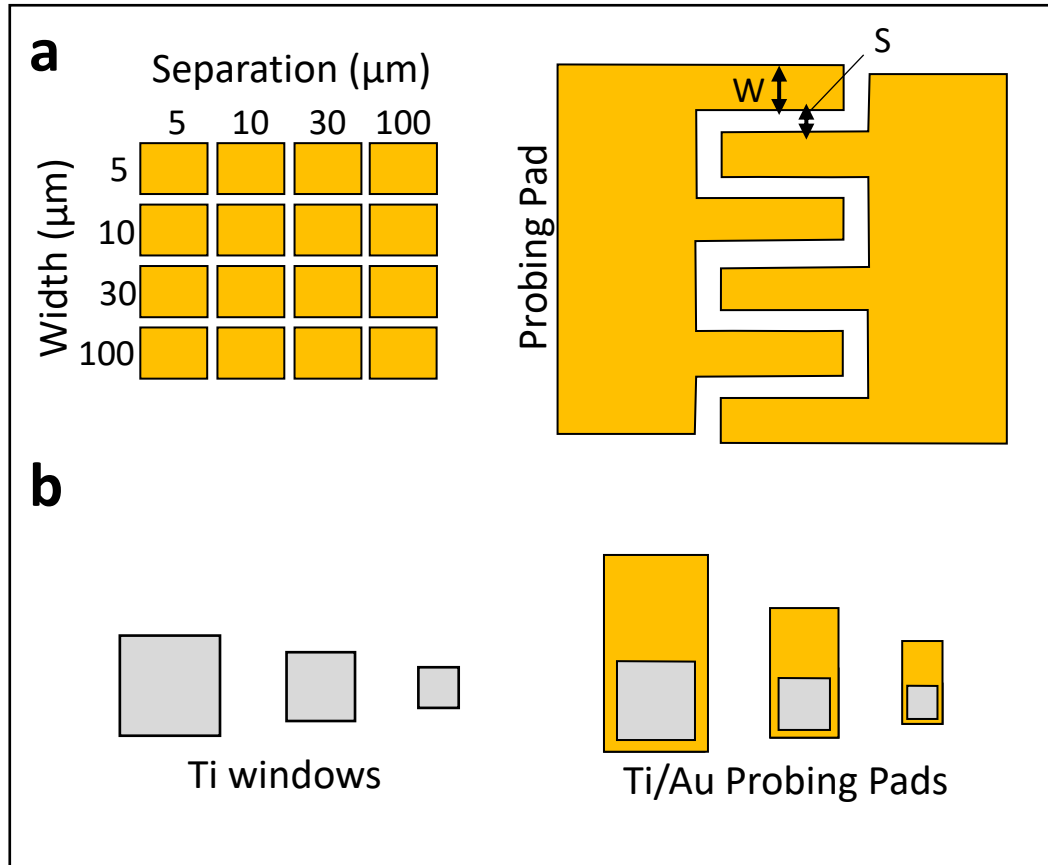


Figure 5.2 Schematic depicting Au the patterns for contacting the InSb thin film. (a) The photoconductor interdigitated finger pattern with various finger width (W) and separation (S) combinations in a 4x4 array, along with a magnified example of a single width and separation combination. (b) The photovoltaic top-contact pattern demonstrating the square pattern for the thin Ti windows (grey) and the Au overlay (yellow) used to border the Ti windows for electrical probing.

Following photoresist exposure, the samples were given a toluene bath for 6 min to prevent development of unexposed regions. The samples were then developed in MICROPOSIT MF319 for 75 s checking with a light microscope periodically to ensure adequate development of the exposed regions. Following development, the metal top contacts for both the photovoltaic and photoconductive devices were deposited by electron-beam physical vapor deposition (EBPVD). The thin Ti window for the photovoltaic device

was deposited at a rate of 1 \AA/s until a Ti layer of approximately 12.5 nm thickness was attained. After Ti deposition, an overlapping contact pad was deposited for electrical probing, which consisted of 15 nm of Ti deposited at a rate of 0.5 \AA/s followed by 150 nm of Au deposited at a rate of 2 \AA/s . The latter Ti/Au deposition was also used for the square photovoltaic contact pads.

Following EBPVD, lift-off was performed to obtain the final contacts. Lift-off was performed with a Remover PG bath overnight, followed by a brief sonication and gentle agitation in acetone, followed by observation with a light microscope to check lift-off success prior to scanning electron microscopy (SEM). Post lift-off, an Al back contact was deposited on the Si substrates via a Torr International sputtering system. Al was sputtered at a rate of $\sim 1 \text{ \AA/s}$ until a thickness of 4000 \AA was achieved. To ensure Ohmic contacts, rapid thermal annealing was performed at $315 \text{ }^\circ\text{C}$ for 30 s [5.9]. For probing purposes, the finished samples were bound to copper, Si side down, with EPO-TEK H20E silver epoxy and cured on a hotplate at $120 \text{ }^\circ\text{C}$ for 15 min. SEM images of the finished photoconductive devices are shown in figure 5.3.

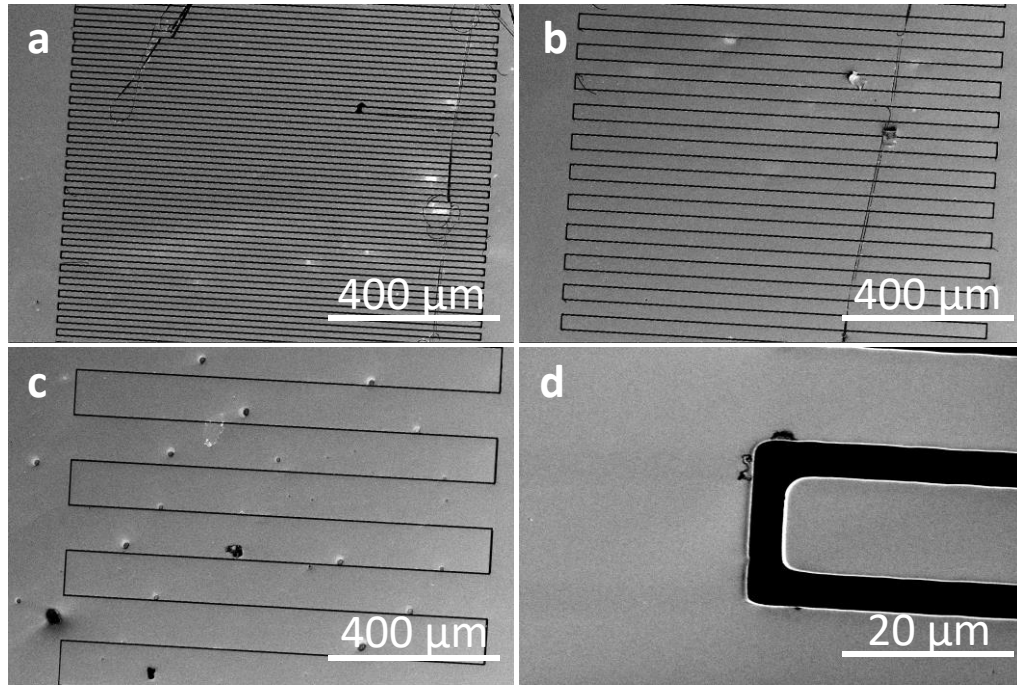


Figure 5.3 SEM images of the completed interdigitated finger top-contact for photoconductive studies. The finger separations presented in all images is 5 μm . The finger widths are a) 10, b) 30, and c) 100 μm . Image d) depicts W10 S5 at a higher magnification, showing the end of an individual finger.

FTIR was performed on a separately grown InSb thin film. An undoped 2.5 μm thick InSb thin film was grown on an undoped Si (100) substrate to avoid free-carrier absorption, allowing transmittance measurements by FTIR. This undoped InSb thin film growth was previously reported in detail in chapter 3. FTIR was performed using a BRUKER Hyperion 3000 with a halogen source and MCT detector. The thin film absorbance spectra was measured with a 15x objective lens and was calculated as $A=1-R-T$ where A is the absorbance, R was the measured reflectance spectrum and T was the measured transmittance spectrum. Identical measurement conditions were used to obtain background spectra prior to each measurement. Reflectance background measurements were taken on

a gold-coated glass slide, and transmittance background measurements were taken through unobstructed air through an opening in the sample stage.

J-V characteristic measurements were performed with a custom-built measurement setup. A Keithley 2400 sourcemeter was used to apply a voltage ranging from -0.2 V to 0.2 V between the interdigitated finger contacts for the photoconductor arrangement, and through the p-i-n structure for the photovoltaic arrangement as depicted in figure 5.1. Measured current values were normalized to the area between the interdigitated contacts for the photoconductor devices, or the Ti window area for the photovoltaic devices.

Photocurrent measurements were performed using both IR and solar illumination. IR illumination was provided by a Thorlabs SLS203L with a silicon carbide global light source. The global source provides emission in the wavelength range of 500 – 9000 nm and a spectrum that is comparable to a blackbody source at 1500 K. The output of the IR source was focused with a CaF₂ lens to a spot 5 mm in diameter centered on the Ti window for the photovoltaic devices, and on the interdigitated fingers for the photoconductive devices. The Thorlabs IR source specifies a power of 1.5 W at the output port. When focused to a spot diameter of 5 mm in our J-V measurement setup, this corresponds to a power density of 7500 mW/cm². Assuming each photon generates one EHP, a maximum photocurrent of 1.2×10^4 mA/cm² is expected from devices under the IR illumination. For solar illumination of the samples, a Newport 150 W xenon arc lamp was used to simulate the AM1.5G solar spectrum. Assuming each photon generates one EHP, a maximum photocurrent of 70 mA/cm² is expected from devices under the solar illumination.

5.3 Results and Discussion

5.3.1 SEM and FTIR of InSb Thin Films

The SEM image in figure 5.4(a) depicts a planar view of the p-i-n InSb thin film surface, indicating a polycrystalline film structure. Clear grain boundaries are seen with size between 1 μm and 5 μm . Measured and expected FTIR data are presented and compared in figure 5.4(b). The expected absorptance data is calculated from InSb complex refractive index data [5.10], with measured data performed on the undoped InSb thin films grown on transparent undoped ($>100 \Omega\cdot\text{cm}$) Si (100) substrates outlined in chapter 3. The p-i-n structure InSb thin film on an n-type (As-doped, $< 0.005 \Omega\cdot\text{cm}$) Si (100) substrate used for the devices is also presented, showing complete absorption in the IR region. Measurements performed on the n-type Si substrates themselves demonstrated the same complete absorptance indicating significant absorptance of the doped Si substrate in the IR region due to free carrier absorption. The bandgap energy of InSb at 300 K is about 0.17 eV [5.1], corresponding to a wavelength of 7.29 μm . The absorptance data measured by FTIR for the InSb demonstrated a good comparison to theoretical data with a downwards trend to roughly 7.3-7.4 μm before leveling off beyond this. In general, the measured absorptance is higher than the theoretical absorptance. This can potentially be attributed to reflectance scattering from the polycrystalline surface leading to a perceived higher absorptance.

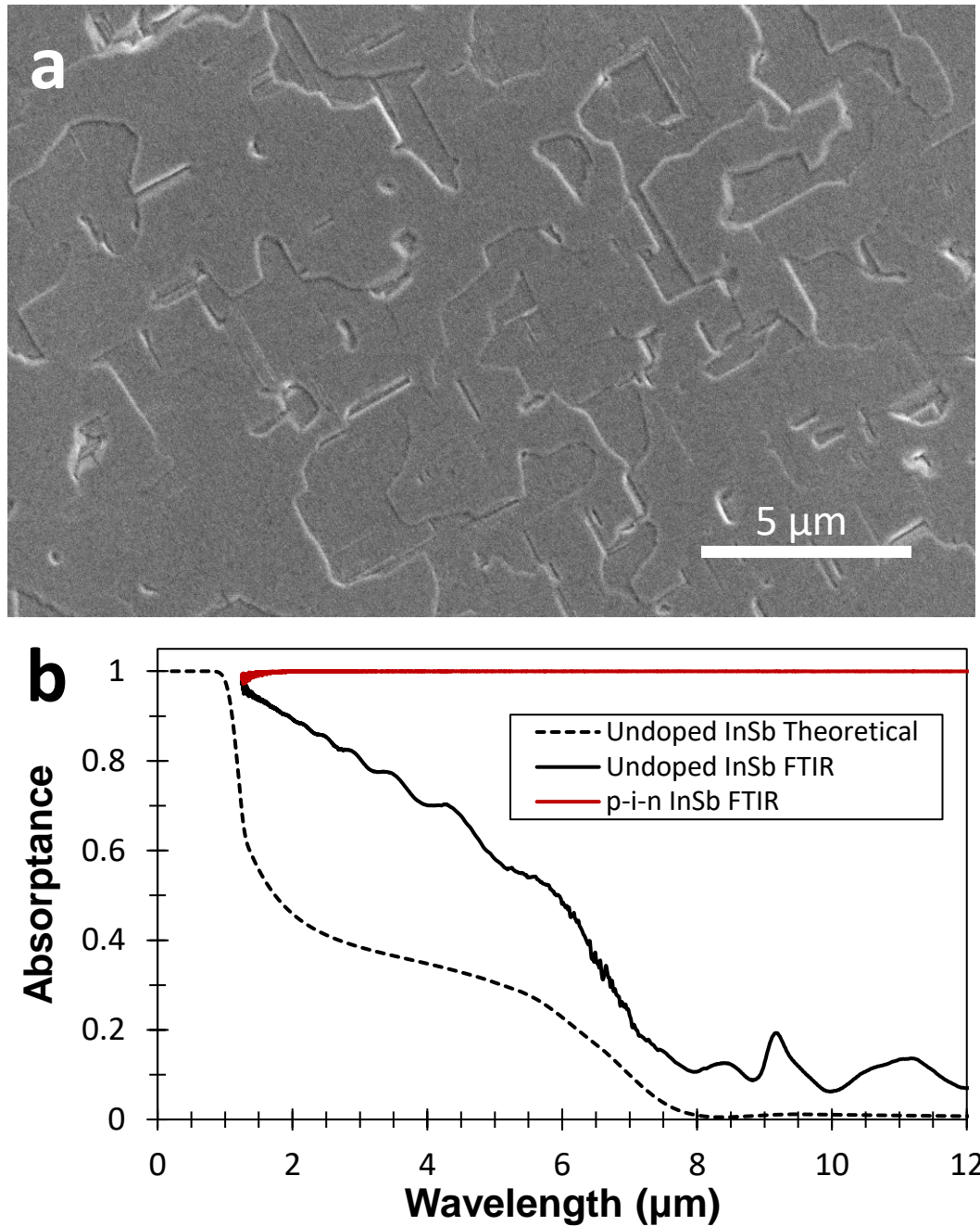


Figure 5.4 Analysis of InSb thin films. (a) Plan view SEM image of the p-i-n InSb thin film growth. (b) FTIR results comparing measured undoped InSb data (black-solid) to expected data (black-dashed), and to p-i-n structured InSb on an As doped ($< 0.005 \Omega \cdot \text{cm}$) Si (100) substrate (red-solid).

5.3.2 Dark J-V Characteristics of InSb Thin Film Photoconductor Devices

Dark current-voltage (J-V) measurements performed at room temperature on the InSb thin film photoconductor devices are presented in figure 5.5. The measured dark current was symmetric under positive and negative bias, and linear near 0 V bias as seen in the inset of figure 5.5. This behavior is expected for a photoconductor device that behaves essentially as a resistor. The non-linear behavior with increasing bias may be due to Schottky barriers associated with the metal-semiconductor contacts, or barriers formed at the polycrystalline grain boundaries of the InSb film. Figure 5.6(a) shows the J-V characteristics for fixed finger separation ($S=100\ \mu\text{m}$) and varying finger width ($W=10, 30, 100\ \mu\text{m}$). Figure 5.6(b) shows the J-V characteristics for fixed finger width ($W=10\ \mu\text{m}$) and varying finger separation ($S=5, 10, 30, 100\ \mu\text{m}$). It is seen that for a fixed finger separation distance of $S = 100\ \mu\text{m}$, increasing the finger width from $W = 10\ \mu\text{m}$ to $W = 100\ \mu\text{m}$ acted to increase the measured current (figure 5.6(a)). This may be explained by a decrease in finger resistance as finger width increases. It is also seen that for a fixed finger width of $W = 10\ \mu\text{m}$, decreasing the finger separation distance from $S = 100\ \mu\text{m}$ to $S = 5\ \mu\text{m}$ acted to increase the measured current (figure 5.6(b)). This may be explained by fewer polycrystalline grain boundaries along the conduction path as the contact separation decreases, since the polycrystalline grain size is on the order of microns. Our observations have similarly been observed on GaAs interdigitated contact devices [5.11]. It should be noted that the p-InSb and i-InSb layers of the photoconductor device may actually be n-doped, similar to the InAsSb Hall data (chapter 4). Thus, the entire InSb structure as well

as the Si substrate may contribute to an n-type conduction path, yielding the high current densities observed in figure 5.5.

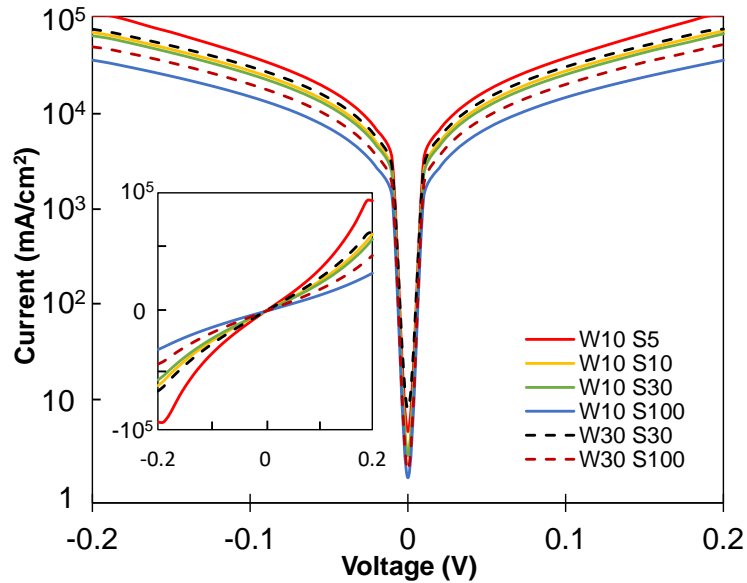


Figure 5.5 Dark J-V characteristics for select finger width and separation combinations presented on a semi-log plot. The inset depicts the same data in a linear plot.

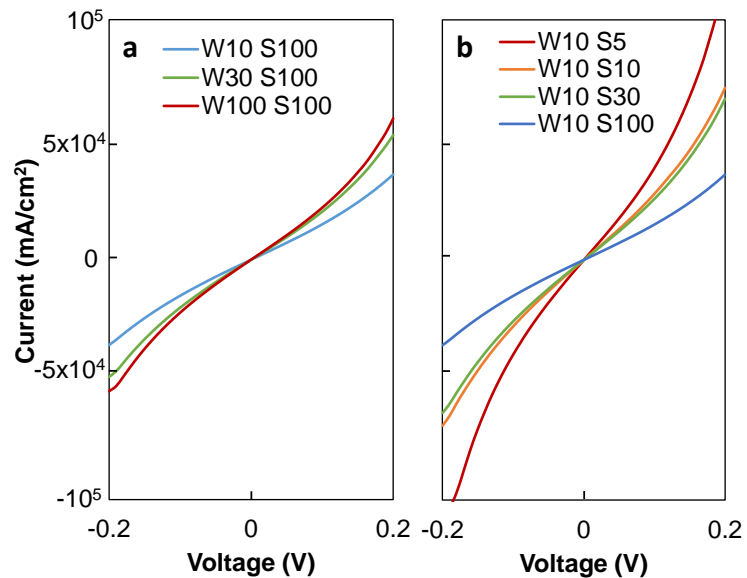


Figure 5.6 Dark J-V characteristics demonstrating the trends for (a) a fixed finger separation, and (b) a fixed finger width.

5.3.3 Dark J-V Characteristics of InSb Thin Film Photovoltaic Devices

Dark current-voltage (J-V) measurements performed at room temperature on the InSb photovoltaic devices are presented in figure 5.7. The measured dark currents of the photovoltaic devices showed negligible rectification and were similar in magnitude to the photoconductor results in figure 5.5. This suggests that the p-i-n structure was not providing an effective diode. Indeed, as mentioned above, the Hall measurements described in chapter 4 indicated that the intended p-type doping may actually be n-type. Thus, the p-i-n structure is acting essentially as a resistor (photoconductor device) between the top and bottom contacts.

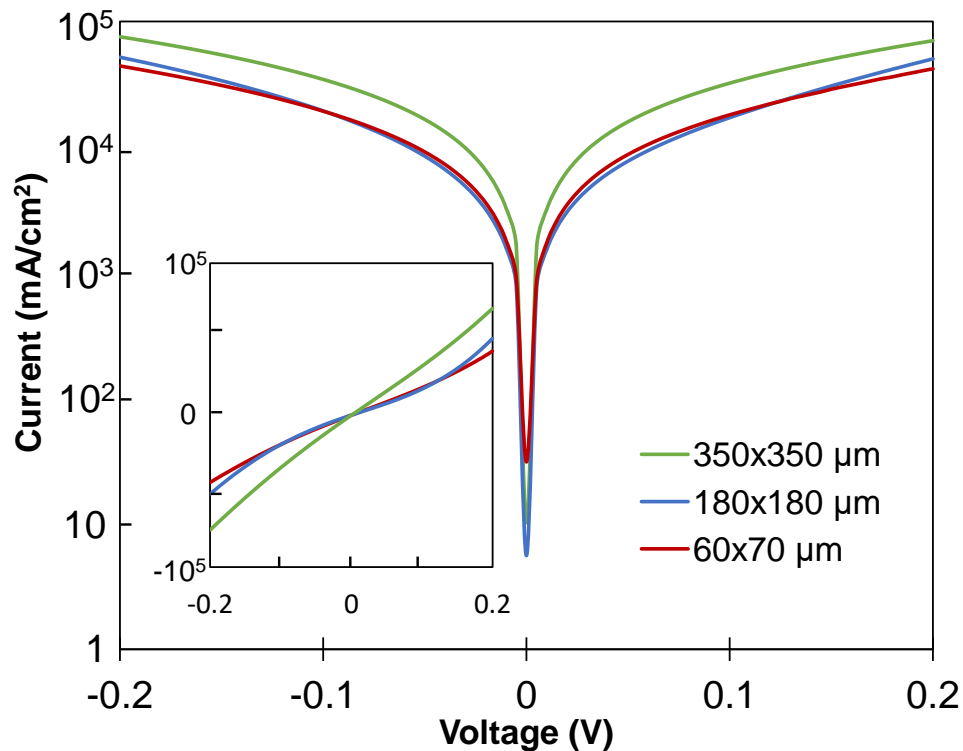


Figure 5.7 Dark J-V characteristics for select square contact areas on a semi-log plot. The inset depicts the same data in a linear plot.

5.3.4 Thin Film Photocurrent Results

J-V measurements were performed on the photoconductor device and photovoltaic device under IR and solar illumination as presented in figure 5.8. Figure 5.8 shows the difference between the current measured under illumination and dark conditions (i.e., the photogenerated current). An increase in measured current consistently occurred for both the photoconductor and photovoltaic devices under both IR illumination and solar illumination, indicating electron-hole pair (EHP) generation.

Under IR illumination, the main contributor to EHPs is expected to be the InSb thin film. However, the doped n-type Si substrate was observed to be opaque in the IR region by FTIR, indicating absorption from the Si substrate as well. The W10 S5 interdigitated contact photoconductor device (figure 5.8(a)) showed a much higher IR photocurrent compared to the other devices, with a value of about 3500 mA/cm² at ±0.2 V. This increase in photocurrent with decreasing contact separation could be attributed to fewer InSb crystallites between the contacts, as discussed earlier. In general, the remaining interdigitated contacts yielded more tightly grouped IR photocurrent values up to 500 mA/cm² at ±0.2 V.

Under solar illumination (figure 5.8(b)), the photocurrent from the photoconductor devices tended to be higher than under IR illumination. The photocurrent ranged from 500 mA/cm² to 1500 mA/cm² at a reverse bias of -0.2 V, and 1000 mA/cm² to 3000 mA/cm² at a forward bias of 0.2 V. These photocurrents exceeded the maximum value expected under solar illumination (70 mA/cm²) by several orders of magnitude, suggesting that the device

structure was behaving as a photoconductor with internal gain. Further studies are required to determine the origin of this gain mechanism, but it may be due to the Si substrate acting as the photoconductor.

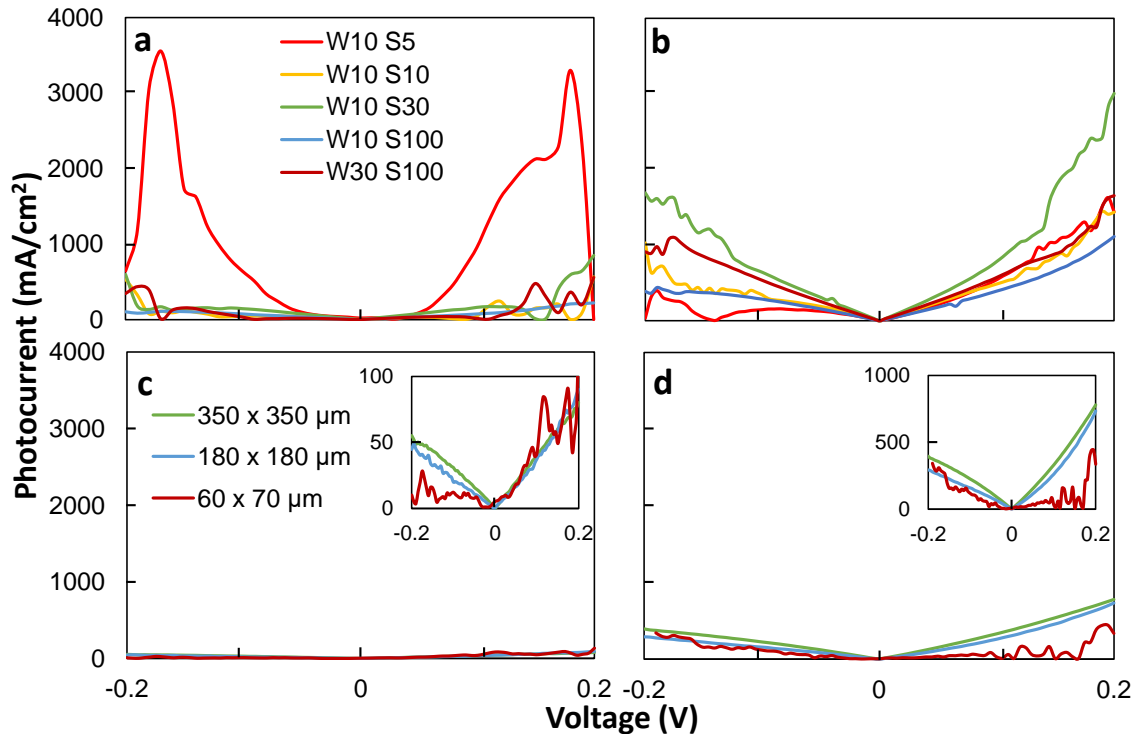


Figure 5.8 Measured photocurrent obtained from the InSb photoconductor and photovoltaic devices. The photoconductor device under (a) IR illumination and (b) solar illumination and the photovoltaic device under (c) IR illumination and (d) solar illumination. The inset of c and d present the photocurrent on a smaller current range.

For the photovoltaic devices under both IR illumination (figure 5.8(c)) and solar illumination (figure 5.8(d)), the photocurrents measured were between one and two orders of magnitude lower than for the photoconductor devices. Under IR illumination, the measured photocurrent from the photovoltaic devices ranged from 50 mA/cm² under

reverse bias to 85 mA/cm^2 under forward bias. Under solar illumination, the photocurrent ranged from 350 mA/cm^2 under reverse bias to 730 mA/cm^2 under forward bias. The photocurrents collected from the $350 \times 350 \text{ }\mu\text{m}^2$ area window and the $180 \times 180 \text{ }\mu\text{m}^2$ area window were comparable, with the current measured from the $60 \times 70 \text{ }\mu\text{m}^2$ window containing more noise. As with the photoconductor device, the photovoltaic device's photocurrent was higher under solar illumination and exceeded the maximum expected photocurrent of 70 mA/cm^2 . Again, this suggests that the photovoltaic devices were behaving as photoconductors with internal gain, probably from the Si substrate. Negligible open-circuit voltage was obtained from the photovoltaic devices, again indicating issues with creation of the p-i-n junction.

5.4 Preliminary InSb Pillar Device

5.4.1 InSb Pillar Device Fabrication

Completed pillar arrays outlined in chapter 3 were fabricated into a device for preliminary testing. During device processing, benzocyclobutene (BCB) was deposited by spin-coating onto the pillars to planarize the surface for contact deposition. The spun BCB is thicker than the length of the pillars, but is back-etched by RIE to expose the tops of the pillars for contacting. An SEM image of the exposed pillar tips of InAsSb pillars outlined in chapter 4 is shown in figure 5.9(a) to demonstrate the process (SEM images of the back-etched BCB of the preliminary InSb pillar device were not obtained). To assess the effect of the BCB on the optical absorptance, FTIR was performed on the pillars post-BCB back-etch, and on BCB spun on a transparent undoped Si (100) substrate. The pillar array

presented has D: 1700 nm and P: 4000 nm. The FTIR spectrum, shown in figure 5.9(b), shows absorbance peaks associated with BCB predominantly in the LWIR, with a narrow peak at 8 μm , a large broad peak at about 9.5 μm , and a pair of overlapping peaks from 11.5-13 μm . These are seen clearly in the measurement performed on BCB itself (black), and are seen interfering with the HE_{11} resonant absorption peak of the back-etched BCB coated pillar array (blue), when compared to the pillar array with no BCB (red). The overall absorbance of the resonant peak is reduced, with obfuscation due to the peaks attributed to the BCB. Although the BCB interferes to a degree, the HE_{11} peak is still visible.

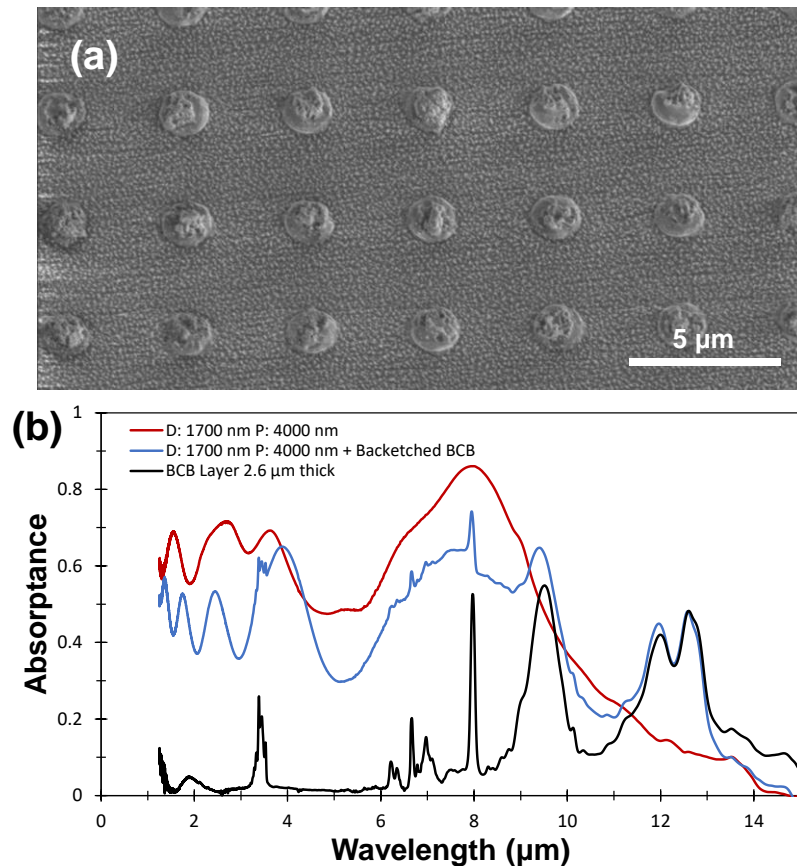


Figure 5.9 (a) SEM images of back-etched BCB-coated InAsSb pillar structures. (b) FTIR results demonstrating the effect of back-etched BCB on pillar absorption for a select array of D: 1700 nm and P: 4000 nm. FTIR performed on a ~ 2.6 μm thick BCB layer on the same undoped Si (100) substrate is included for comparison.

With the BCB back-etched and FTIR performed, Al was sputtered on the rear of an InSb sample (on the Si substrate) at a rate of $\sim 1 \text{ \AA/s}$ until a thickness of 4000 \AA was achieved as a back-contact. Thin ($\sim 10 \text{ nm}$) semi-transparent Ni windows were deposited by EBPVD on four individual pillar arrays with (D, P) combinations of (900 nm, 3000 nm), (1100 nm, 3000 nm), (1300 nm, 3500 nm), and (1500 nm, 4000 nm). Following the Ni window, a top contact was then deposited by EBPVD slightly overlapping the Ni window, consisting of Ni/Ge/Au at thicknesses of 25/50/225 nm. The area of the Ni window covering the InSb pillar array is approximately $400 \times 400 \text{ \mu m}^2$, corresponding to 0.0016 cm^2 . The measured current was normalized to this area.

5.4.2 InSb Pillar Dark Current Results

Dark J-V measurements performed at room temperature on the InSb pillar devices are presented in figure 5.10. The measured dark current was asymmetric under positive and negative bias ranging from -2 to 2 V. The inset presenting the data on a linear scale demonstrates the asymmetry more clearly with current rectification characteristic of a photodiode. A steady reverse saturation current I_0 is observed for each pillar array under dark conditions with the D: 900 nm P: 3000 nm array yielding a lower I_0 of 0.04 mA/cm^2 , and the other three arrays being more tightly grouped in the range of $0.16\text{-}0.22 \text{ mA/cm}^2$. Under forward bias, an exponential increase in current occurs. Although diode rectification is observed, the origin of it within the sample is not clear as the sample consisted of a single undoped InSb thin film growth on an undoped ($>100 \text{ \Omega}\cdot\text{cm}$) Si (100) substrate. The rectification may be due to the band offsets at the InSb/Si heterointerface, or a Schottky contact on the InSb and/or Si substrate.

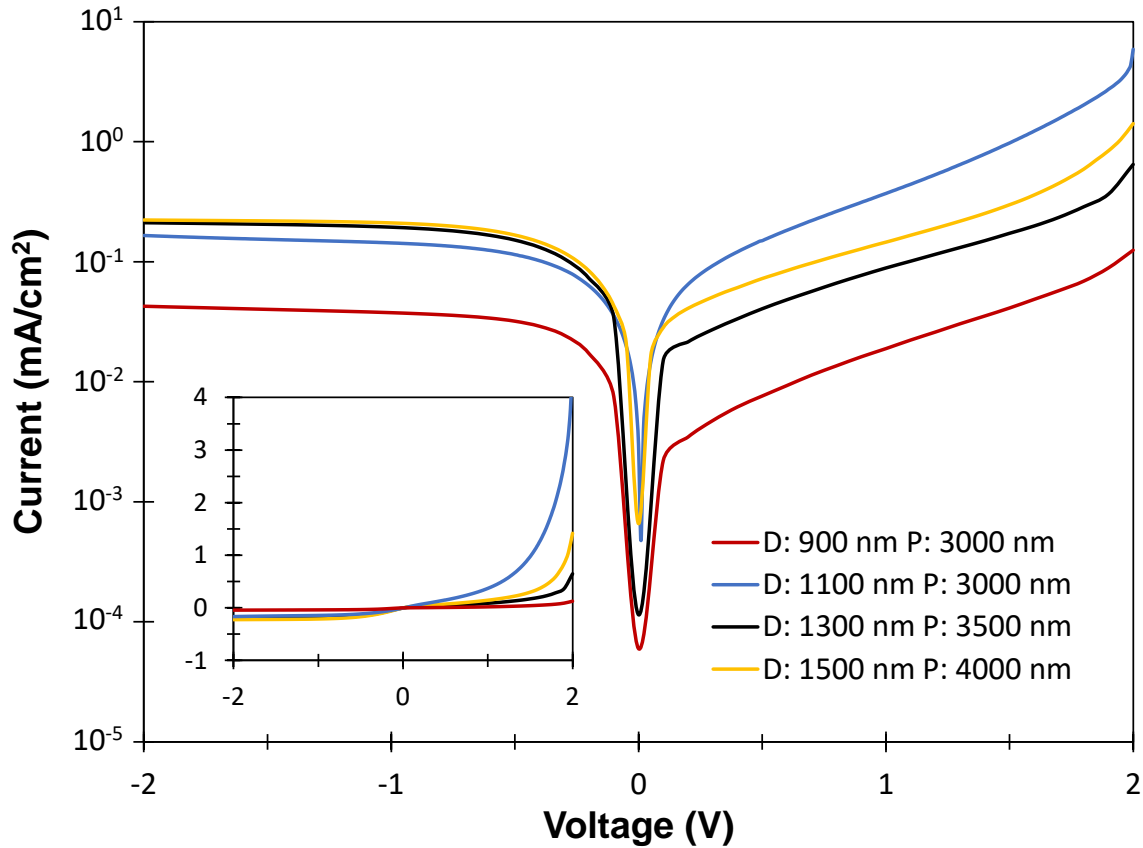


Figure 5.10 Dark J-V characteristics for four InSb pillar diameter and pitch combinations presented on a semi-log plot. The inset depicts the same data in a linear plot.

5.4.3 InSb Pillar Photocurrent Results

J-V characterization was performed on the pillar devices under IR illumination, with representative data presented in figure 5.11 for the D: 1100 nm and P: 3000 nm array. The inset shows the data on a linear plot. Although photocurrent is generated, an unusual kink is observed near zero bias. The photocurrent generated from each pillar array, taken to be the absolute value of the difference between IR illuminated and dark current, is presented in figure 5.12(a). To confirm that photocurrent generation was occurring in the InSb pillars and not the Si substrate itself, bandpass filters were used to isolate wavelength regions

centered at 4.75 μm , 5.75 μm , 6.5 μm , and 7.5 μm . Each filter had a full-width-at-half-maximum of about 0.5 μm . J-V characterization performed with the filters in place is presented in figure 5.12(b), demonstrating the photocurrent measured with each filter for the pillar array with D: 900 nm and P: 3000 nm. The photocurrent measured under full IR illumination for each array ranges from roughly 1.12 to 4.24 mA/cm^2 at -2 V. For the D: 900 nm P: 3000 nm array, the value is 1.93 mA/cm^2 at -2 V. With the filters in place, the photocurrent measured for this array at -2 V is in the range of 0.006-0.0075 mA/cm^2 , 2 orders of magnitude lower than during full IR illumination, but still discernable from the dark current. With the array of interest having a peak absorption wavelength of roughly 4.85 μm , it was expected that illumination while using the bandpass filter centered at 4.75 μm would yield the highest measured photocurrent, but this was not the case. In general, J-V characterization using the filters was not consistent with what would be expected, although photocurrent generation was still observed with the filters in place, possibly indicating contribution from the InSb pillars. The small values of photocurrent measured with the filters in place, on the order of $\mu\text{A}/\text{cm}^2$, may require cooling of the device or processing with a lock-in amplifier to study further.

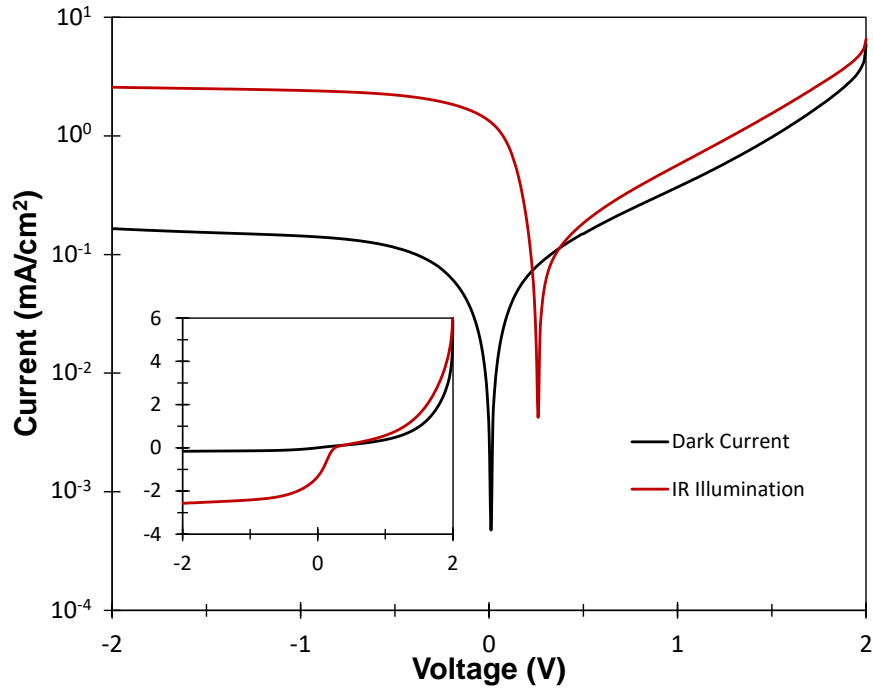


Figure 5.11 J-V characterization under IR illumination compared to dark current for the pillar array with D: 1100 nm and P: 3000 nm on a semi-log plot. The inset depicts a linear plot.

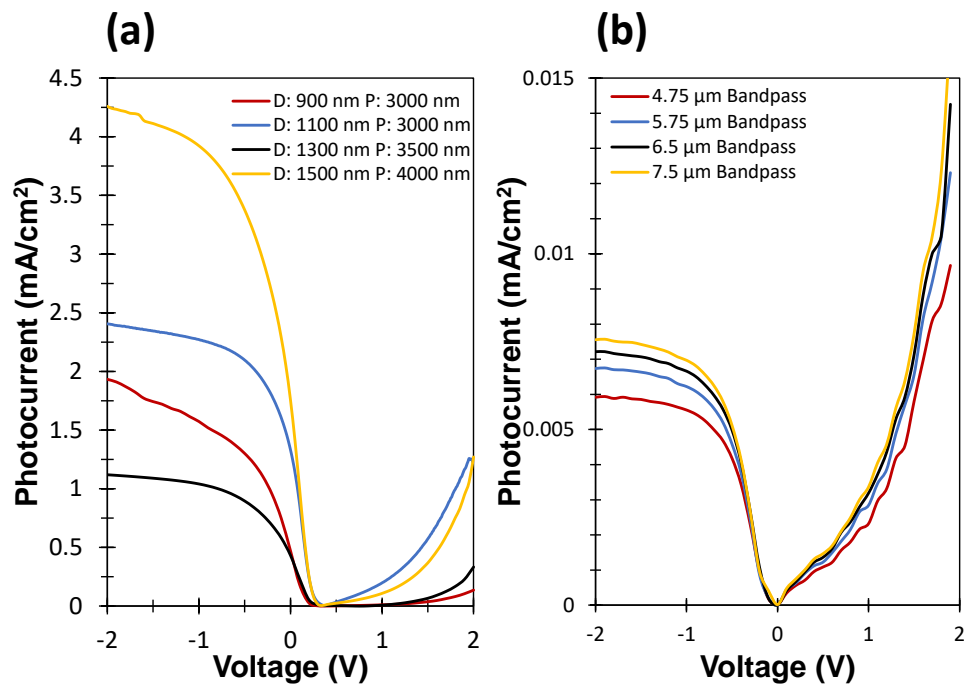


Figure 5.12 (a) Photocurrent measured for each pillar array under full IR illumination. (b) Photocurrent measured for the D: 900 nm P: 3000 nm pillar array taken under filtered IR illumination.

5.5 Conclusion

p-i-n structure InSb thin films were grown on n-Si (100) substrates via MBE and processed into thin film IR devices; photoconductor devices with varying interdigitated finger contact geometry, and photovoltaic devices with varying top-contact collection window areas. Dark current values measured for both the photoconductor and photovoltaic devices were high and ohmic, indicating that the p-i-n diode was ineffective at rectification due to doping issues. Photocurrent measurements were obtained for both the photoconductor and photovoltaic devices under IR and solar illumination, indicating the presence of photogenerated EHPs for both devices. The highest measured photocurrent of about 3500 mA/cm² was obtained from the W10 S5 interdigitated contact, with all the other combinations showing lower photocurrents of about 500 mA/cm² at ± 0.2 V. The higher photocurrent of the W10 S5 contact geometry is explained by this contact's finger width being much closer to the grain size of crystallites in the thin film.

Preliminary InSb pillar devices were fabricated from undoped InSb pillars on a highly resistive Si (100) substrate. Although no intentional p-n junction was introduced, the pillar devices demonstrated current rectification. Photocurrent generation was observed under full IR illumination for each of the four pillar devices. The use of bandpass filters in the LWIR region demonstrated contribution of the InSb pillars in photocurrent generation.

5.6 References

- [5.1] I. Vurgaftman, J. Meyer, and L. Ram-Mohan, Band parameters for III-V compound semiconductors and their alloys, *J. Appl. Phys.* 89 (2001) 5815
- [5.2] A. Rogalski, HgCdTe infrared detector material: history, status and outlook, *Rep. Prog. Phys.* 68 (2005) 2276
- [5.3] A. Evirgen, J. Abautret, J. Perez, A. Cordat, A. Nedelcu, and P. Christol, Midwave infrared InSb nBn photodetector, *Electron. Lett.* 50 (2014) 1472-1473
- [5.4] I. Kimukin, N. Biyikli, and E. Ozbay, InSb high-speed photodetectors grown on GaAs substrate, *J. Appl. Sci.* 94 (2003) 5414
- [5.5] B. Jia, K. Tan, W. Loke, S. Wicaksono, K. Lee, and S. Yoon, Monolithic integration of InSb photodetector on silicon for mid-infrared silicon photonics, *ACS Photonics* 5 (2018) 1512-1520
- [5.6] B. Jia, K. Tan, W. Loke, S. Wicaksono, and S. Yoon, Growth and characterization of InSb on (100) Si for mid-infrared application, *Appl. Surf. Sci.* 440 (2018) 939-945
- [5.7] C. Goosney, V. Jarvis, D. Wilson, N. Goktas, and R. LaPierre, InSb nanowires for multispectral infrared detection, *Semicond. Sci. Technol.* 34 (2019) 035023
- [5.8] C. Goosney, V. Jarvis, J. Britten, and R. LaPierre, InAsSb pillars for multispectral long-wavelength infrared absorption, *Infrared Phys. Technol.* 111 (2020) 103566
- [5.9] K. Hosotani, T. Ito, Y. Yasui, K. Nakayama, A. Kadoda, M. Mori, and K. Maezawa, Low resistance ohmic contacts to n-InSb employing Sn-alloys, 2013 IEEE International Meeting for Future of Electron Devices, Kansai, 2013 72-73
- [5.10] S. Adachi, Optical dispersion relations for GaP, GaAs, GaSb, InP, InAs, InSb, $\text{Al}_x\text{Ga}_{1-x}\text{As}$, and $\text{In}_{1-x}\text{Ga}_x\text{As}_y\text{P}_{1-y}$, *J. Appl. Phys.* 66 (1989) 6030-6040
- [5.11] Zebentout, A.; Bensaad, Z.; Zegaoui, M.; Aissat, A.; Decoster, D.; Effect of dimensional parameters on the current of MSM photodetector, *Microelectron. J.* 42 (2011) 1006-1009

Chapter 6 – Focused Ion Beam Etching of Single Pillar Structures

FIB etches were performed on an undoped InAsSb thin film growth on undoped ($> 100 \Omega \cdot \text{cm}$) Si (100) substrates (outlined in chapter 4) for optical characterization on single pillar structures. Etching was performed with a FEI Versa 3D Dual Beam system. As mentioned in section 2.2.4, the optical properties of NW structures allow for not only enhanced absorption at a wavelength-dependent NW diameter, but also for enhanced absorption over an area exceeding that of the NW cross-sectional area. This allows for single NWs to demonstrate enhanced optical absorption seen in NW arrays. The initial pattern for FIB etching consisted of a single pillar, a 2x2 array, and a 3x3 array, all with pillars of $1.7 \mu\text{m}$ diameter (and $4 \mu\text{m}$ pitches for the arrays). The second pattern used for FIB etching consisted of a $1 \mu\text{m}$ diameter single pillar, a $1.7 \mu\text{m}$ diameter single pillar, a 2x2 array consisting of $1.7 \mu\text{m}$ diameter pillars with a $4 \mu\text{m}$ pitch, and a 2x2 array consisting of a $1.1 \mu\text{m}$, $1.5 \mu\text{m}$, $1.9 \mu\text{m}$, and $2.3 \mu\text{m}$ diameter pillar with a $5 \mu\text{m}$ pitch. Low magnification SEM images of the FIB etches depicting the patterns are shown in figure 6.1. It can be seen with the initial etches in figure 6.1a that excessive etching was done creating a well into the Si substrate around each pillar. The second etch was performed in order to reduce this effect, and to introduce a 2x2 array of pillars with varying diameters. Higher magnification images are presented in figure 6.2. Figures 6.2(a)-(c) present the first etch and the over etching is more clearly seen. Figures 6.2(d)-(f) are of the second etch, showing the multi-diameter array.

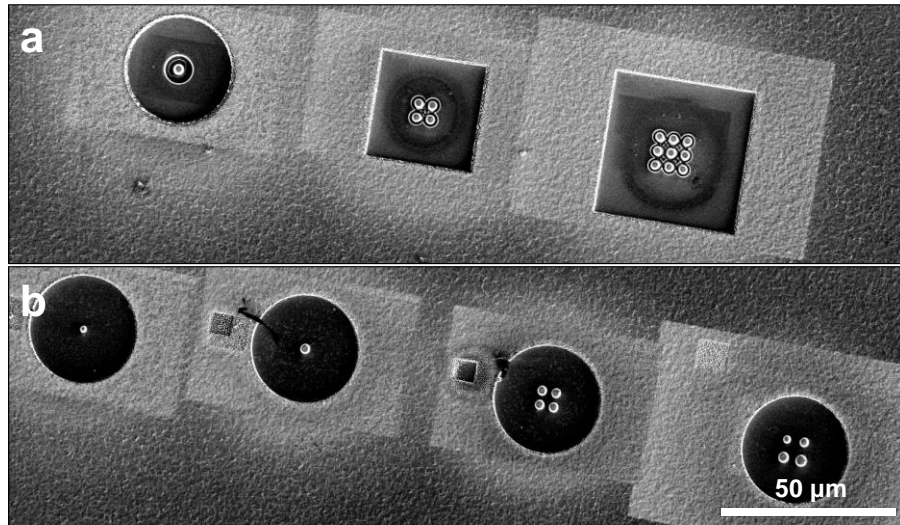


Figure 6.1 Plan view SEM images taken with the FEI Magellan of (a) the initial etch consisting of a single pillar, a 2x2 array, and a 3x3 array, and (b) the second etch consisting of 2 single pillars of different diameters, and two 2x2 arrays with one containing pillars of the same diameter, and the next containing pillars of varying diameters. The scale bar in (b) applies to both images.

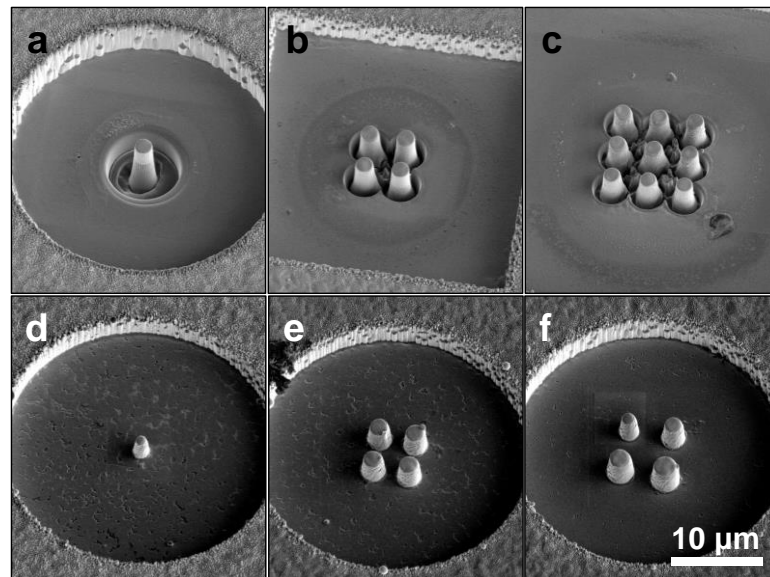


Figure 6.2 30° tilted SEM images taken of the initial FIB etch depicting (a) a single 1.7 μm diameter pillar, (b) a 2x2 array of 1.7 μm diameter pillars, and the second FIB etch depicting (c) a 3x3 array of 1.7 μm diameter pillars, (d) a single 1 μm diameter pillar, (e) a 2x2 array of 1.7 μm pillars, and (f) a 2x2 array of a 1.1 μm , 1.5 μm , 1.9 μm , and 2.3 μm diameter pillar. The scale bar in (f) is applicable for all images.

FTIR measurements were performed with a Bruker Vertex 70 and the Hyperion 3000 microscope on both the first and second etch sets, as presented in figure 6.3. Figure 6.3(a) presents FTIR measurements performed on the first FIB etch in which a single pillar (orange), a 2x2 array (blue), and a 3x3 array (yellow) were created, all pillars having a diameter of 1.7 μm . For comparison, a full 300x300 μm^2 array produced by EBL from chapter 4 with pillar diameter of 1.7 μm and pitch of 4000 nm is also shown (black). Figure 6.3(b) presents the measurements performed on the second FIB etch for a single 1.7 μm diameter pillar (orange), and the 2x2 array of 1.7 μm diameter pillars (blue). In both cases no obvious sharp resonant peak was observed where it would be expected. This may be due to Ga deposition occurring during the FIB etch process that obscures the pillar absorptance.

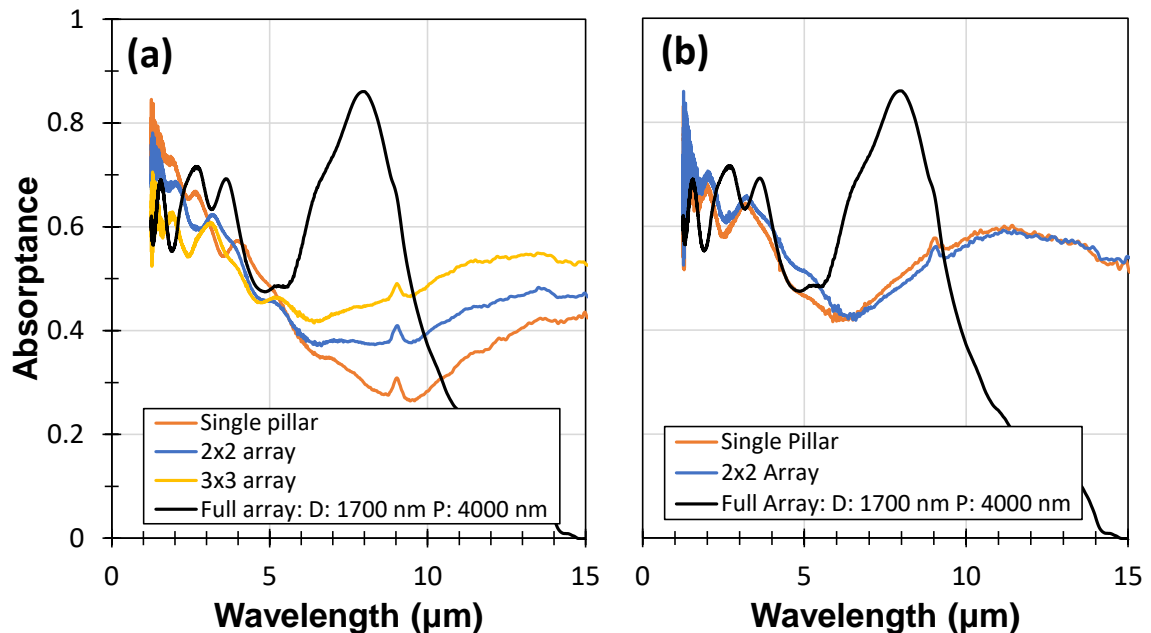


Figure 6.3 FTIR results obtained for (a) the initial etch pattern, and (b) the etch pattern done to reduce undercutting into the substrate.

To confirm the presence of Ga, EDS was performed on the 4x4 multi-diameter array using the FEI Magellan SEM. EDS results are presented in figure 6.4. The EDS mappings revealed a high Si signal from the circular etched region around the pillars corresponding to the Si substrate. A significant Ga presence is also observed in the FIB etched region, confirming that Ga was deposited during the milling process. Attempts to selectively etch the Ga should be attempted in the future.

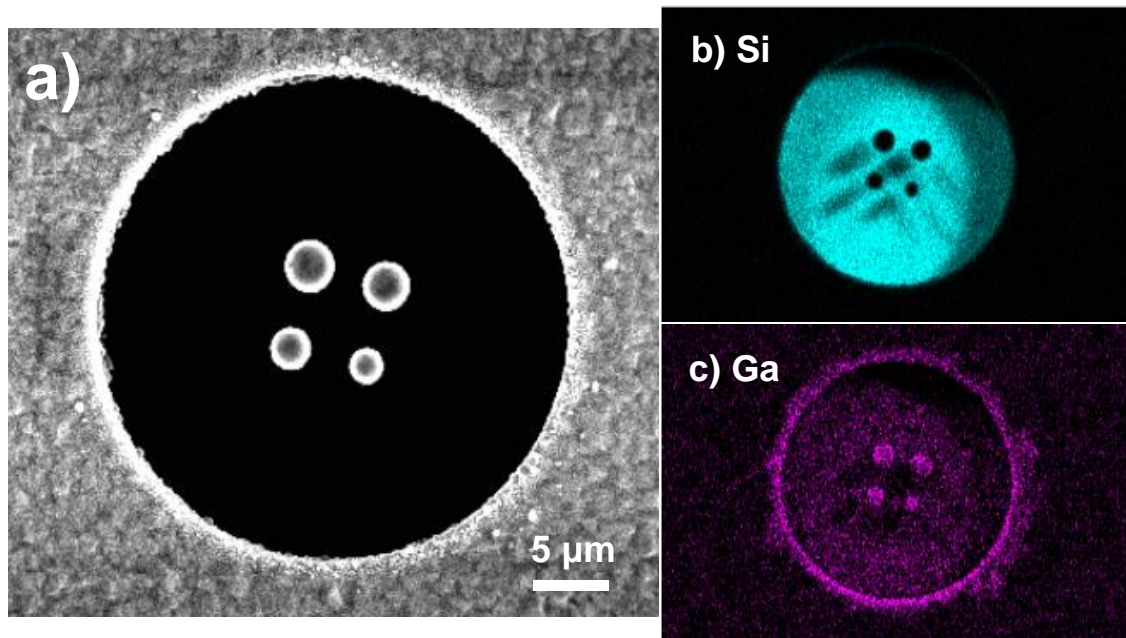


Figure 6.4 (a) SEM image of the 2x2 array consisting of pillars of varying diameters and a 5000 nm pitch. (b) EDS mapping of Si presented in blue. (c) EDS mapping of Ga presented in purple. Signal from In, As, and Sb was present representing the pillar and surrounding thin film and is omitted.

Chapter 7 – Conclusion and Future Prospects

7.1 Thesis Summary

The InSb and InAsSb material system was investigated for MWIR and LWIR multispectral absorption. Absorption wavelength tunability was achieved through the manipulation of pillar diameter and pitch, as opposed to altering the material composition of the system, by utilizing the unique optical properties that NW structures offer. 2.5 μm thick InSb and InAsSb thin films were successfully grown on undoped ($> 100 \Omega\cdot\text{cm}$) Si (100) substrates by MBE with a thin 10 nm thick AlSb buffer layer used to alleviate defects due to the large lattice mismatch between InSb, InAsSb, and Si, and promote epitaxial growth. SEM and XRD were used to demonstrate improvements in thin film growth quality. A top-down fabrication method utilizing EBL and ICP-RIE was used successfully to achieve 300x300 μm pillar arrays with pillars ranging in diameter from 300-1500 nm (InSb) and 1700-4000 nm (InAsSb), and pitches ranging from 1000-3000 nm (InSb) and 4000-6000 nm (InAsSb). Etches were successful and consistently demonstrated large scale pillar arrays. FTIR measurements of the InSb pillars demonstrated wavelength tunability from 1.61 μm to 6.86 μm with a 100 nm increase in pillar diameter corresponding to a 0.53 μm increase in peak absorption wavelength. Measurements of the InAsSb pillar arrays demonstrated wavelength tunability from 8.1 to 16.2 μm with a 100 nm increase in pillar diameter corresponding to a 0.46 μm increase in peak absorption wavelength. Overall FTIR measurement data is presented in figure 7.1 demonstrating the ability for MWIR and LWIR tunability with the InAsSb material system.

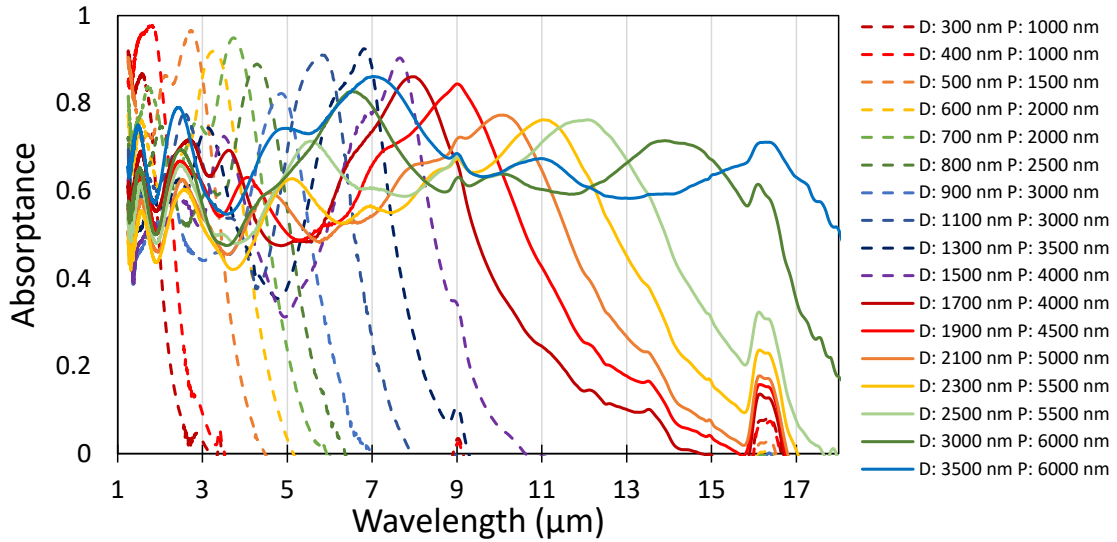


Figure 7.1 Complete FTIR results for InSb (dashed) and InAsSb (solid) pillars.

Single pillar structures were etched from the InAsSb thin film by Ga ion FIB etching to observe enhanced optical absorption from a single pillar. SEM confirmed successful pillar etches. EDS confirmed Ga deposition around the etched structures which may be interfering with local FTIR measurements at the immediate etch site.

Be-doped p-InSb thin films were grown on n-type Si (100) substrates in an attempt to form a p-i-n junction. Interdigitated photoconductor devices with varying finger contact geometry, and photovoltaic devices with varying top-contact collection window areas were processed. Dark current values measured for both devices were high and ohmic, indicating that the p-i-n diode was ineffective at rectification. Hall effect measurements performed on doped and undoped InAsSb thin films indicated a strong n-type behavior even with an intended p-type doping, demonstrating potential issues with the doping process. Photocurrent measurements were obtained from the InSb thin film devices under IR and

solar illumination, indicating the presence of photogenerated EHPs for both devices. The highest measured photocurrent of about 3500 mA/cm^2 was obtained from the W10 S5 interdigitated contact, with all the other combinations showing lower photocurrents of about 500 mA/cm^2 at $\pm 0.2 \text{ V}$. The higher photocurrent of the W10 S5 contact geometry is explained by this contact's finger separation being much closer to the grain size of crystallites in the thin film. Although the p-i-n structure failed to produce rectifying behavior, photogenerated current was consistently discernable from dark current, both under IR and solar illumination. A higher than expected photocurrent indicated a possible gain mechanism.

7.2 Future Prospects

With the successful fabrication of large pillar arrays allowing for absorption in the range of about $1.6\text{-}16 \mu\text{m}$, the next step should consist of processing such an array into a pillar device for IR photodetection. As discussed in section 5.4, a preliminary InSb pillar device was fabricated from undoped InSb on an undoped ($> 100 \Omega\cdot\text{cm}$) Si (100) substrate, as this sample was used for extensive FTIR measurements. BCB was used for this sample to add structural integrity to the pillars, to electrically isolate them, and to form a planar surface for top-contacting of the InSb pillar tips. Further studies are necessary to ensure that the proper doping profile is achieved, due to the doping difficulties observed with InAsSb during MBE growth. An example of such an InSb pillar device with a p-i-n junction implemented is presented in figure 7.2.

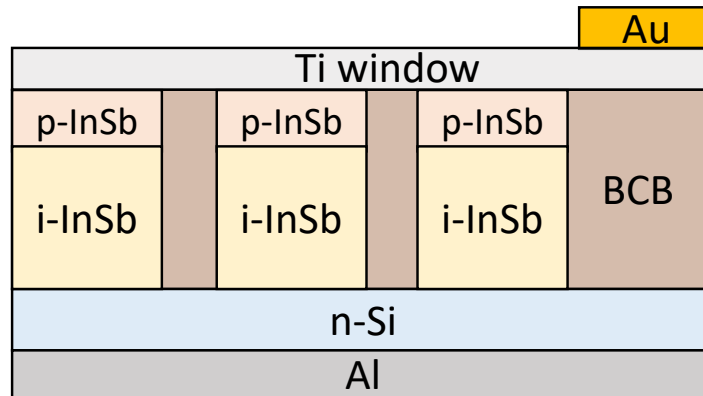


Figure 7.2 Potential device structure for an p-i-n InSb pillar array.

The goal of fabricating such a large diameter pillar device would be to demonstrate multispectral capabilities through the observation of a diameter-dependent photocurrent in the LWIR region, similar to the results demonstrated in [7.1]. Under illumination, a peak in photocurrent generation occurring at the wavelength corresponding to the HE_{11} mode of the pillar is expected to occur. Future work could perform photocurrent measurements at lower temperatures, and use a lock-in amplifier and the FTIR for multispectral device measurements, similar to those performed in [7.2].

7.3 References

- [7.1] J. Svensson, N. Anttu, N. Vainorius, B. Borg, and L.E. Wernersson, Diameter-dependent photocurrent in InAsSb nanowire infrared photodetectors, *Nano Lett.* 13 (2013) 1380-1385
- [7.2] M. Atalla, S. Assali, S. Koelliung, A. Attiaoui, and O. Moutanabbir, High-bandwidth extended-SWIR GeSn photodetectors on Si achieving ultrafast broadband spectroscopic response, *ACS Photonics* 9 (2022) 1425-1433